Development of a time-resolved photoluminescence imaging system using a compressed sensing approach

by
Aidas Baltušis

Submitted in fulfilment of the requirements for the degree of Doctor of Philosophy

James Watt School of Engineering

College of Science & Engineering

University of Glasgow

June 2025

Appendix 2.4

University of Glasgow
College Identity

Statement of Originality to Accompany Thesis Submission

Name: __________Aidas Baltušis____

Registration Number: ______xxxxxxx______________________________________

I certify that the thesis presented here for examination for PhD degree of the University of Glasgow is solely my own work other than where I have clearly indicated that it is the work of others (in which case the extent of any work carried out jointly by me and any other person is clearly identified in it) and that the thesis has not been edited by a third party beyond what is permitted by the University's PGR Code of Practice.

I declare that the thesis does not include work forming part of a thesis presented successfully for another degree.

I declare that this thesis has been produced in accordance with the University of Glasgow's Code of Good Practice in Research.

I acknowledge that if any issues are raised regarding good research practice based on review of the thesis, the examination may be postponed pending the outcome of any investigation of the issues.

Signature: ____

Date: ____

Abstract

In this work, a novel measurement technique for time-resolved photoluminescence (TRPL) imaging of semiconductors is developed using a compressed sensing approach. TRPL provides crucial insights into the charge carrier lifetimes of semiconductor materials, which directly reflect material quality and influence the efficiency of electron-hole recombination processes—key factors in the performance of devices such as solar cells and LEDs. However, conventional TRPL techniques are limited in their ability to efficiently capture high spatial resolution data, often requiring slow, point-by-point measurements that are time-intensive and unsuitable for large or non-uniform samples. The compressed sensing method developed in this work overcomes these limitations by enabling simultaneous measurement of multiple spatial points, reducing the number of measurements required while maintaining high-resolution imaging and accuracy.

The first part of the thesis develops a comprehensive simulation framework for compressed sensing TRPL measurements, beginning with simple 1D models and expanding to complex simulations in both the spectral and temporal domains. The simulation follows a statistical approach, integrating key factors such as photon pile-up and noise to ensure realistic modelling of experimental conditions. A reconstruction algorithm is also developed to handle the high-dimensional data generated from compressed sensing TRPL, forming the foundation for the design and implementation of the experimental system. The simulation results show that in some cases, as few as 2% of measurements can be sufficient compared to conventional methods, demonstrating the effectiveness of compressed sensing.

The second part of this thesis focuses on the design and construction of a TRPL measurement system, specifically developed for imaging semiconductor samples with emission in the near-infrared (NIR) spectral range using a raster scanning approach. The experimental system was setup using 640 nm pulsed laser for excitation and two photomultiplier tube detectors, allowing detection between 700-1600 nm. Point measurements were conducted on cadmium telluride (CdTe) and copper indium gallium selenide (CIGS) samples, while

full raster-scan measurements were performed on CdTe. These experiments demonstrated the system's capability but highlighted challenges such as laser light leakage and divergence of the laser beam.

In the final part of the thesis, the experimental system is modified, to demonstrate a proof-of-concept compressed sensing TCSPC imaging system for acquiring TRPL maps of semiconductor materials and devices. The TRPL imaging results obtained using the compressed sensing approach are compared with those acquired through a conventional point-by-point method over the same excitation area. The feasibility of this methodology is clearly demonstrated, highlighting reductions of 50% or more in measurement acquisition time. Additionally, the benefits and challenges of the experimental prototype system are presented and thoroughly discussed, laying the groundwork for further improvements in system design and application.

Overall, these results provide a pathway toward an improved approach to TRPL imaging, with the first example of a compressed sensing TRPL system. While this thesis primarily focuses on photovoltaic applications, the findings are applicable to other wavelengths and material systems. Future work can build on this foundation to overcome the remaining limitations and further enhance the technique's capabilities.

Acknowledgements

I would like to express my deepest gratitude to my academic supervisor, Professor Stephen Sweeney. My journey into research began under his guidance during my undergraduate research project, and it was his support and encouragement that sparked my interest in pursuing a PhD. Throughout this project, his technical expertise and insightful advice have been invaluable. I am especially grateful for his patience and unwavering encouragement, which provided me with the confidence to navigate the challenges of this research.

I am greatly indebted to my industrial supervisors, Dr George Koutsourakis and Dr Sebastian Wood at the National Physical Laboratory (NPL). I would like to express my gratitude to Dr George Koutsourakis for his invaluable expertise, training, and day-to-day assistance in troubleshooting experimental challenges. His mentorship and guidance were essential to the successful development of the experimental aspects of this project. I would also like to thank Dr Sebastian Wood for his thoughtful feedback, valuable input, and strategic guidance.

I am also grateful to the Engineering and Physical Sciences Research Council (EPSRC) for providing the primary funding for my PhD, without which this journey would have not been possible. I am also appreciative of the NPL for providing the facilities that enabled me to conduct my research. I would also like to extend my gratitude to NPL and IQE plc. for providing financial support in the form of iCASE studentship.

My heartfelt thanks go to my friends, whose words of encouragement kept me motivated to push ahead. Their constant encouragement and belief in me, particularly during the most challenging and uncertain moments of this journey, gave me the strength to persevere.

Research Outputs

Publications

[1] Baltušis, A., Koutsourakis, G., Wood, S., Blakesley J. and Sweeney, S. J., "Compressed sensing approach for temporal and spectral photoluminescence imaging of semiconductors", Conference Proceedings, SPIE Optical Metrology Conference, Modelling Aspects in Optical Metrology (2023).

[2] Baltušis, A., Koutsourakis, G., Wood, S. and Sweeney, S. J., "Development of Time-Resolved Photoluminescence Microscopy of Semiconductor Materials and Devices using a Compressed Sensing Approach" IOP Measurement Science and Technology, 35, 015207 (2024).

Oral Presentations

[1] Baltušis, A., Koutsourakis, G., Wood, S. and Sweeney, S. J., "*Compressed Sensing Time-Resolved Photoluminescence Microscopy of Semiconductor Materials and Devices*" Presentation delivered at UK Semiconductors 2022 conference

[2] Baltušis, A., Koutsourakis, G., Wood, S. and Sweeney, S. J., "*Compressed Sensing Time-Resolved Photoluminescence Microscopy of Semiconductor Materials and Devices*" Presentation delivered at Photon 2022 - Advances in Optical Metrology and Measurements conference

[3] Baltušis, A., Koutsourakis, G., Wood, S. and Sweeney, S. J., "Compressed sensing approach for temporal and spectral photoluminescence imaging of semiconductors" Presentation delivered at SPIE Optical Metrology Conference, Modelling Aspects in Optical Metrology (2023).

[4] Baltušis, A., Koutsourakis, G., Wood, S. and Sweeney, S. J., "*Compressed Sensing Time Resolved Photoluminescence Imaging for Semiconductor Characterisation*" Presentation delivered at SMSI 2023

Poster Presentations

[1] Baltušis, A., Koutsourakis, G., Wood, S. and Sweeney, S. J., "Imaging of Minority Charge Carrier Lifetimes of Semiconductors using Digital Light Processing and Compressed Sensing" Conf. Lasers Electro-Optics, JTu3A.11, Optica Publishing Group (2021).

[2] Baltušis, A., Koutsourakis, G., Wood, S. and Sweeney, S. J., "*Towards wafer scale minority carrier lifetime mapping of compound semiconductors using compressive sensing approach*" Poster presentation given at PGI Conference (2020)

[3] Baltušis, A., Koutsourakis, G., Wood, S. and Sweeney, S. J., "*Contactless defect mapping of semiconductors using compressed sensing and time-resolved photoluminescence*" Poster presentation given at EMRS 2021

[4] Baltušis, A., Koutsourakis, G., Wood, S. and Sweeney, S. J., "*Rapid minority charge carrier lifetime imaging of semiconductor materials and devices using compressed sensing*" Poster presentation given at MIOMD 2021

[5] Baltušis, A., Koutsourakis, G., Wood, S. and Sweeney, S. J., "*Compressed Sensing - Applying Novel Mathematics for Semiconductor Imaging Applications*" Poster presentation given at PGI 2023

[6] Baltušis, A., Koutsourakis, G., Wood, S. and Sweeney, S. J., "*Advancing Semiconductor Material Characterisation with Compressed Sensing Time-Resolved Photoluminescence Imaging*" Poster presentation given at ESLW 2023. **Won best poster presentation award**

Table of Contents

List of Acronyms

ADC	Analog to Digital Converter
APD	Avalanche Photodiode
B&H	Becker & Hickl
CFD	Constant Fraction Discriminator
CIGS	Cadmium Indium Gallium Selenide
CMOS	Complementary Metal-Oxide Semiconductor
cps	Counts per Seconds
CS	Compressed Sensing
CoSaMP	Compressed Sampling Matching Pursuit
DBS	Dichroic Beamsplitter
DCT	Discrete Cosine Transform
DMD	Digital Micromirror Device
EEG	Electroencephalogram
FIB	Focused Ion Beam
FLIM	Fluorescence Lifetime Imaging Microscopy
FWHM	Full Width at Half Maximum
HPMT	Hybrid Photomultiplier Tube
IRF	Instrument Response Function
LBIC	Light Beam Induced Current
LED	Light Emitting Diode
MCP	Multichannel Plate
MNOP	Mean Number of Photons
MOEMS	Microoptoelectromechanical System
MRI	Magnetic Resonance Imaging

MTBF	Mean Time Before Failure
NA	Numerical Aperture
ND	Neutral Density
NIR	Near Infrared
NP	Nondeterministic Polynomial Time
NPL	National Physical Laboratory
OD	Optical Density
OMP	Orthogonal Matching Pursuit
PCI	Peripheral Component Interconnect
PL	Photoluminescence
PMT	Photomultiplier Tube
PV	Photovoltaics
RIP	Restricted Isometry Property
RMSE	Root Mean Squared Error
SP	Subspace Pursuit
SPAD	Single-Photon Avalanche Diode
SRH	Shockley-Read-Hall
SSIM	Structural Similarity Index Measure
TAC	Time-to-Amplitude Converter
TDC	Time-to-Digital Converter
TCSPC	Time-Correlated Single Photon Counting
TRPL	Time-Resolved Photoluminescence
VCSEL	Vertical-Cavity Surface-Emitting Laser
WHT	Walsh-Hadamard Transform
ZC	Zero Cross

Chapter 1 Introduction

Imaging takes many forms and is widely used across multiple disciplines of science and industry, ranging from medical diagnostics (e.g. MRI [1,2] and X-Ray imaging [3]) to materials science (e.g. electron microscopy [4] or atomic force microscopy [5]). Imaging typically refers to optical imaging where the light is reflected or emitted by the material under observation. However, it can also encompass other modalities, such as acoustic [6], or thermal imaging [7]. Many forms of measurement can be used – as long as it is possible to introduce the control of the spatial dimensions. Afterall, imaging is simply measuring a given quality with control over the points in space where the measurements are taken. In a most common example – taking simple photographs, the spatial information is recorded by having a high number of individual detectors, i.e. pixels of the camera sensor.

What is often challenging with certain imaging applications, is finding a reliable way to control the points in space where measurements are taken. This means imaging is not limited to visualising the surface of materials but can extend to detecting internal properties, such as charge carrier dynamics within semiconductors, which are critical for understanding and optimising them. The work presented in this thesis focuses on developing a novel imaging approach to measure charge carrier lifetimes in semiconductor materials.

In the field of semiconductor research, imaging can reveal not just the physical structure but the dynamic behaviour of the charge carriers. The charge carrier lifetime is a critical property in semiconductor materials, providing insights into the efficiency of electron-hole recombination processes, which directly affect the performance of devices such as solar cells and LEDs. Longer carrier lifetimes, typically indicate a lower density of crystallographic defects within the material. When carrier lifetimes are too short, the recombination of charge carriers occurs more rapidly, which can reduce the efficiency of semiconductor devices by increasing energy losses through non-radiative recombination processes [8]. Measuring the charge carrier lifetimes is challenging, even without considering imaging. This lifetime refers to the typical time it takes a mobile carrier to recombine within the material. It is not an absolute value but rather a statistical representation, an average across many carriers.

Conventional methods for measuring carrier lifetimes, such as time-resolved photoluminescence (TRPL), offer high temporal resolution, but they face challenges in terms of spatial resolution and measurement time, especially when dealing with large samples or non-uniform materials. The existing approaches typically rely on scanning approaches, where imaging is acquired by performing a raster scan. This thesis seeks to address these limitations by developing a novel TRPL imaging system based on compressed sensing, enabling faster acquisition without compromising accuracy.

Time-correlated single-photon counting (TCSPC) is a widely used technique for measuring TRPL, providing precise temporal resolution, down to a few picoseconds, at the single-photon level. This method is particularly advantageous when dealing with the charge carrier lifetimes of semiconductor materials, which can range from sub-nanosecond to multiple microseconds. Additionally, the light intensities encountered in TRPL are typically very low, where other detection methods would struggle. TCSPC enables the signal acquisition to be expanded over multiple laser pulses, effectively expanding the signal collection time over longer periods of time. By measuring the arrival times of photons relative to the excitation pulse, TCSPC can accurately determine the decay characteristics of photoluminescence signals, making it particularly useful for studying semiconductor materials. In this thesis, TCSPC was chosen due to its superior time resolution and sensitivity, which are critical for accurately resolving charge carrier lifetimes in both homogeneous and heterogeneous semiconductor materials.

While TCSPC offers excellent temporal resolution, it comes with practical limitations for imaging applications. The acquisition time of a single measurement can take multiple seconds as signal detection relies on accumulating sufficient photon counts. Therefore, acquiring high spatial resolution images, would require significant amount of time. However, once acquired, these images are likely to be highly compressible due to the presence of large homogeneous regions, with features only occurring in specific areas. Compressed sensing can take advantage of this sparsity, enabling the key features of the samples to be captured more quickly while significantly reducing the time needed for full data acquisition.

Compressed sensing is a mathematical framework that enables the reconstruction of signals from a limited number of measurements. Traditionally, the minimum number of measurements required to accurately acquire a signal are dictated by the Shannon-Nyquist theorem [9]. It states that the signal must be sampled with at least twice the measurement frequency, compared to the highest frequency present in the signal. In conventional imaging, this means that every point within the area of interest must be sampled, even if the sample is highly homogenous. This process can be time-consuming and data-intensive, particularly when high-resolution imaging is required.

In recent years, compressed sensing has shown great promise in various imaging applications, such as MRI [10] and radar imaging [11], where it allows for faster data acquisition and reduced storage requirements. In the context of TRPL, where both high temporal and spatial resolution are required, compressed sensing offers the potential to significantly reduce the time needed for data acquisition without compromising the accuracy of the resulting images. By integrating compressed sensing with TCSPC, this thesis aims to develop a more efficient TRPL imaging system, capable of delivering both high temporal and spatial resolution and significantly reduced acquisition times.

This thesis is structured to present the development and integration of compressed sensing with TRPL imaging in three major phases. The first part focuses on developing compressed sensing TRPL simulations, where a step-by-step model is built to simulate the acquisition and reconstruction of photoluminescence data, starting from basic 1D signal models and expanding into the spectral and temporal domains. In the second phase, the work details the design and construction of a TRPL imaging system. This involves the development of a prototype system from the ground up and testing its performance through both single-point and raster scan acquisitions. The final part of this thesis explores the implementation of compressed sensing within the TRPL imaging system and successfully validating the technique. This chapter demonstrates successful development and application of the first compressed sensing TRPL imaging system, providing an important proof of concept for future advancements in this field.

1.1 Thesis Structure

The work presented in this thesis is structured as follows:

Chapter 1 – Introduction: This chapter explains the context, motivations and scope of the research conducted in this PhD project. It provides an overview of imaging and its applications to various scientific fields, with a particular focus on imaging techniques for semiconductor characterisation. The challenges associated with TRPL imaging are discussed, and the concept of compressed sensing is introduced, along with its potential benefits for complex imaging applications.

Chapter 2 – Compressed Sensing Theory and Applications: This chapter delves into the theoretical foundations of compressed sensing, which underpins the investigations in subsequent chapters. The scale of signal space and concept of sparsity are highlighted. A detailed explanation of the mathematical principles of compressed sensing is provided, along with examples of appropriate measurement matrices and an overview of the two main groups of reconstruction algorithms. The reconstruction algorithm employed in this work is discussed, with a justification for its selection. The chapter concludes with a review of compressed sensing applications in various scientific domains, including semiconductor characterisation.

Chapter 3 – Modelling of Compressed Sensing Time-Resolved Photoluminescence Measurements: This chapter outlines the development of a computational model to investigate compressed sensing in TRPL measurements. The model begins with a Monte Carlo [12] based simulation of TCSPC, exploring concepts such as photon pile-up and TCSPC from multiple sources. The model is iteratively refined to simulate compressed sensing spectrometry and, ultimately, compressed sensing TRPL measurements. The final model is used to assess the effects of noise and measurement parameters, providing a foundation for subsequent experimental work.

Chapter 4 – Development of Time-Resolved Photoluminescence Imaging System: This chapter details the design and construction of a TRPL imaging system from ground up. Key design considerations are discussed, along with the options evaluated and the specifications of the chosen components. The chapter also covers the characterisation of the laser source used for excitation and presents the results of testing the system on a variety of samples.

Chapter 5 – Implementing Compressed Sensing for Time-Resolved Photoluminescence Imaging: The final results chapter focuses on incorporating compressed sensing into the developed TRPL imaging system. A digital micromirror device (DMD) is integrated to enable the projection of measurement matrices, allowing for compressed sensing measurements. Initial compressed sensing applications are conducted on laser beam profile measurements and photocurrent imaging of photovoltaic devices. Methods for validating the measurements are discussed, and results from compressed sensing TRPL experiments are presented and compared.

Chapter 6 – Conclusions and Future Work: This chapter summarises the findings of each chapter and presents the overall conclusions of the entire project. Potential future research steps are proposed, highlighting key areas for further investigation and continued development of the methodology.

Chapter 2 Compressed Sensing Theory and Applications

Compressed sensing [13] is a relatively recent development in the field of signal processing that allows the recovery of signals from far fewer measurements than traditionally required. By exploiting the inherent sparsity of most real-world signals in certain transform domains, compressed sensing challenges the classical Nyquist-Shannon [9] sampling theorem and offers a framework that promises both efficiency and accuracy in signal reconstruction. This chapter aims to provide the reader with a comprehensive understanding of compressed sensing as a whole and to offer the necessary theoretical background to understand the work carried out in the rest of the thesis.

The chapter begins with a background on the core concepts of compressed sensing, starting with an overview of the mathematical basis for it [14] and the fundamental differences between the ℓ_1 and ℓ_2 norms in signal recovery. The Restricted Isometry Property (RIP) [15], a critical concept ensuring the stability of sparse signal recovery, is introduced. Additionally, the vastness of signal spaces and the crucial role of sparsity in compressed sensing are discussed, highlighting how most meaningful signals can be represented with far fewer components than the full signal space suggests.

In the next section, the focus shifts to compressed sensing reconstruction algorithms. These algorithms are essential for recovering sparse signals from under-sampled data and form the backbone of any compressed sensing system. This section provides an overview of key algorithms used in practice, including optimisation techniques that ensure robust signal reconstruction.

The final sections of the chapter are dedicated to the wide-ranging applications of compressed sensing. From imaging systems to semiconductor characterisation, compressed sensing has found use in various fields requiring efficient and high-resolution data acquisition. Section 2.4 explores real-world applications, demonstrating the practical benefits of compressed sensing in both imaging and characterisation tasks. This includes its use in medical imaging [10], remote sensing, and semiconductor testing, where compressed sensing enables faster data acquisition and improved resolution.

Overall, this chapter provides a thorough introduction to compressed sensing, covering its theoretical principles, practical implementations, and a broad range of applications. By the end of the chapter, the reader will have gained a solid understanding of how compressed sensing is being utilised in various fields of science and engineering, while also being equipped with the background needed to understand the experimental work presented in the subsequent chapters of this thesis.

2.1 Sparsity of signals

Sparsity is a fundamental property that underlies the effectiveness of compressed sensing. Many natural signals, such as images, exhibit sparsity when transformed into specific bases like the wavelet or Fourier basis [16]. For instance, when a natural image is transformed into the frequency domain, the resulting frequency coefficients often show that a small number of coefficients contain the majority of the signal's energy.

Figure 2-1 illustrates this concept, showing the original uncompressed image (a), its frequency coefficients after applying a Fourier transform (b), and the reconstruction achieved by preserving only the top 10% of coefficients (c) while setting the rest to zero. The reconstructed image (d) demonstrates that even with only 10% of the measurements retained, the quality remains remarkably high, confirming the compressibility of natural images.

2.1.1 Vastness of signal spaces

The vastness of the signal space becomes particularly evident when considering images. For instance, a simple 100×100 pixel black-and-white image can be thought of as a grid where each pixel has two possible states: black or white. The number of possible combinations of pixel states in such a grid is enormous. Specifically, for a 100×100 pixel image, the total number of possible images is $2^{100\times100}$, which equals $2^{10,000}$ or approximately 10^{3010}, a number so vast that it dwarfs the number of atoms in the observable universe.

Within this immense space of possible images, the overwhelming majority would appear as random noise—completely meaningless to a human observer. However, this space also contains every possible meaningful image that could be represented on a 100×100 pixel canvas, from simple geometric shapes to highly detailed representations of objects and scenes. This illustrates the immense diversity and complexity of the signal space that compressed sensing must operate in, making efficient recovery of sparse signals all the more critical.

By leveraging the inherent sparsity of most real-world signals (such as natural images, which are not random noise but often contain structure and patterns), compressed sensing allows for the recovery of meaningful information with far fewer measurements than would be needed to fully sample the entire signal space. This efficiency is made possible through a careful understanding of sparsity patterns, measurement matrices, and the coherence between them. As the field continues to evolve, further exploration and optimisation of these components will enhance the ability to recover meaningful signals from within such a vast, complex space.

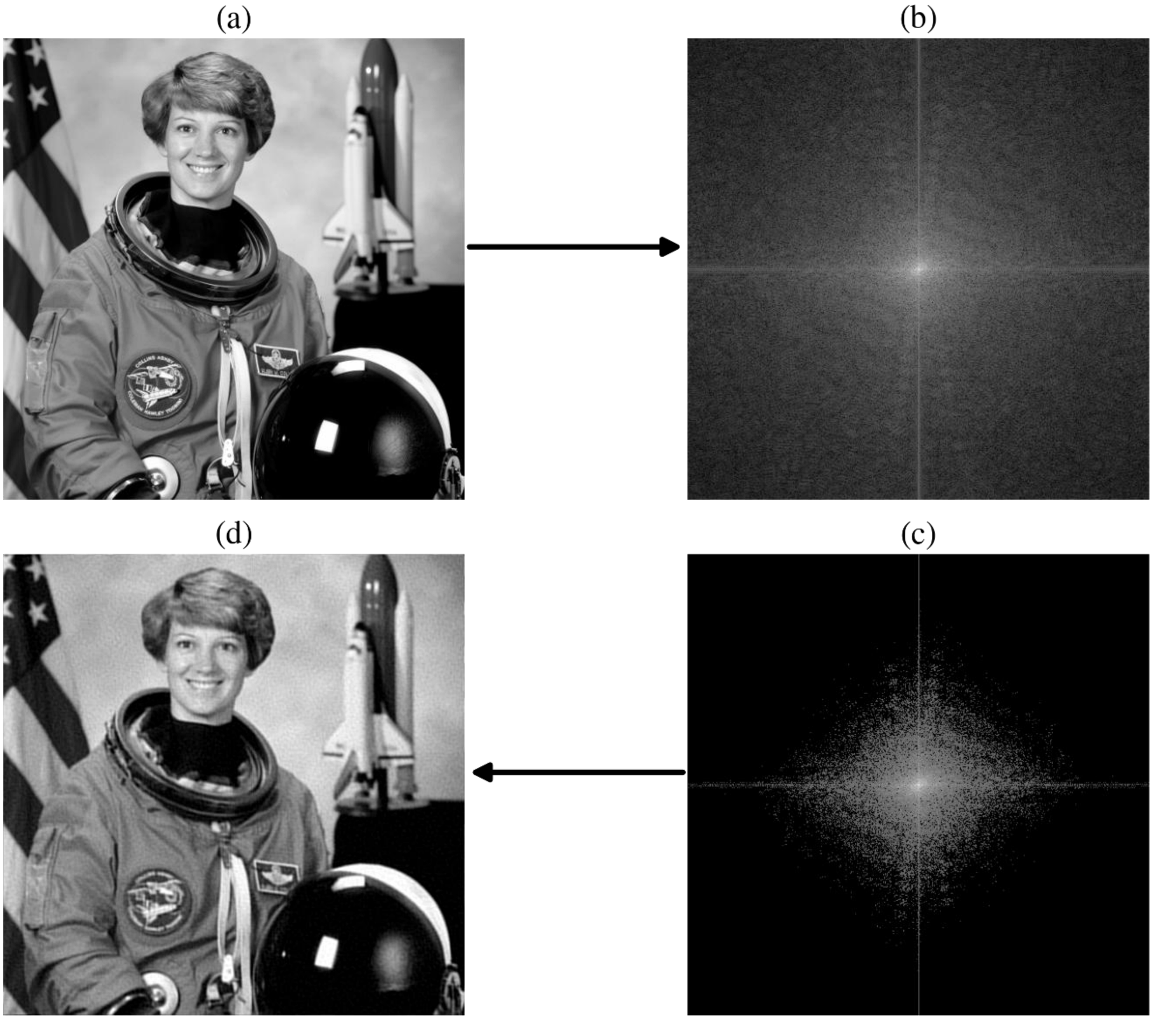

Figure 2-1 Demonstration of the compressibility of natural images. (a) shows the original, uncompressed image. (b) displays the frequency coefficients of the image after applying a Fourier transform, represented on a logarithmic scale. In (c), only the top 10% of the largest coefficients are retained, with the rest set to zero. An inverse Fourier transform is then applied, and the reconstructed image is shown in (d), demonstrating how the image can be effectively reconstructed using just 10% of the frequency components.

2.2 Overview of compressed sensing

Compressed sensing (CS) is a signal processing technique that enables the recovery of sparse signals from a limited number of measurements, often far fewer than required by the classical Nyquist-Shannon sampling theorem. The central idea behind compressed sensing is that many natural signals are sparse or compressible in some domain (such as Fourier or wavelet), meaning that they can be represented by a small number of non-zero coefficients.

This inherent sparsity allows for efficient data acquisition and reconstruction, reducing the need to fully sample the signal at high resolutions.

In compressed sensing, the measurement process is linear and involves projecting the high-dimensional signal onto a lower-dimensional space. Mathematically, this process can be described by the following equation:

$$y = Ax \tag{2.1}$$

where:

- $y \in R^m$ is the measurement vector containing m measurements.
- $A \in R^{m \times n}$ is the measurement matrix, where $m < n$, and n is the length of the signal. This measurement matrix is of critical importance to compressed sensing and is discussed in Section 2.2.4
- $x \in R^n$ is the original signal, which is assumed to be sparse in some transform domain. In the case of image acquisition, n is the number of pixels in the image.

2.2.1 The measurement process

To recover x, compressed sensing exploits the sparsity of signals in some basis or domain. Suppose the signal x is sparse in some transform domain (such as the Fourier or wavelet domain), meaning that it can be represented as:

$$x = \Psi s \tag{2.2}$$

where:

- Ψ is the sparsifying basis or transform matrix (e.g., a Fourier or wavelet basis),

- $s \in R^n$ is the sparse coefficient vector, where most of the entries are zero or close to zero.

Therefore, by substituting Ψs into the measurement equation above, the measurement process can be rewritten as:

$$y = A\Psi s \tag{2.3}$$

The above equation is also illustrated in Figure 2-2. Here, A represents the linear measurement process, which projects the high-dimensional signal s into a lower-dimensional space. Since $m < n$, this system of equations is underdetermined, and therefore, recovering s from y seems impossible at first glance as there are infinite number of solutions. However, if x is known to be sparse, compressed sensing theory shows that it is possible to recover x accurately by solving an optimisation problem that leverages sparsity.

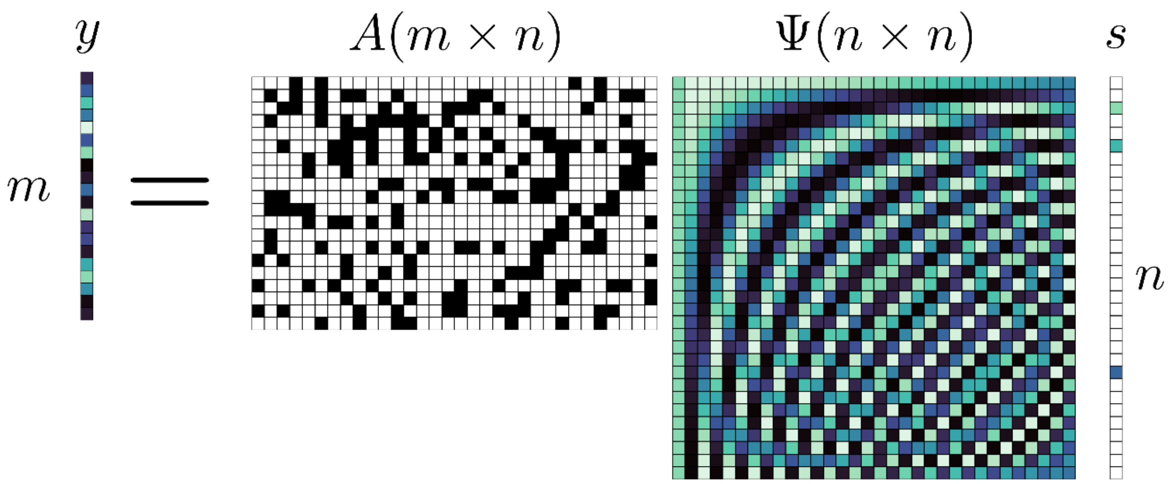

Figure 2-2 Illustration of the compressed sensing measurement process. The visual representation shows how the high-dimensional signal s is compressed into a lower-dimensional measurement through matrix multiplication. By recovering s, the original signal x can be calculated.

2.2.2 Recovering the sparse signal

In compressed sensing, the goal is to recover a signal that is sparse in some basis from a set of under-sampled measurements. Typically, the number of measurements is far fewer than would be required by traditional Nyquist sampling methods. As highlighted in previous sections, most natural signals are sparse and can be represented by only a small number of non-zero coefficients in some transform domain (such as Fourier or wavelet). The ideal way to achieve this sparse recovery would be to minimise the ℓ_0 norm, which directly counts the number of non-zero elements in the signal. This approach, while conceptually simple, is computationally intractable because it requires a combinatorial search through all possible subsets of non-zero coefficients.

To address this, alternative norms like ℓ_1 and ℓ_2 the norms are used, each with different implications for the sparsity and computational complexity of the solution.

$\boldsymbol{\ell_0}$ Norm

The ℓ_0 norm, denoted as $\|s\|_0$, represents the count of the non-zero elements in a signal s. It is defined as:

$$\|s\|_0 = \sum_{k=1}^{n} 1(s_k \neq 0) \tag{2.4}$$

Where $1(s_k \neq 0)$ is an indicator function that equals 1 if s_k is non-zero and 0 otherwise. Minimising the ℓ_0 norm would give the sparsest solution, as it explicitly searches for the solution with the fewest non-zero coefficients. However, solving ℓ_0-minimisation problem is NP-hard because it involves a combinatorial search over all possible subsets of non-zero entries. As the number of variables increases, the number of possible combinations grows exponentially, making the problem computationally intractable for large systems. This combinatorial nature means no known algorithm can solve all instances efficiently (i.e., in polynomial time), placing it in the class of computationally intractable problems. Therefore, in the case of signal recovery, the optimisation problem could be written down as:

$$\hat{\boldsymbol{s}} = argmin \, \|s\|_{\boldsymbol{0}} \; subject \; to \; y = A\Psi s \tag{2.5}$$

$\boldsymbol{\ell_1}$ Norm

The $\boldsymbol{\ell_1}$ norm, denoted as $\|s\|_1$, serves as a more practical alternative to ℓ_0. It is defined as:

$$\|s\|_1 = \sum_{k=1}^{n} |s_k| \tag{2.6}$$

where s is a vector representing the signal. The $\boldsymbol{\ell_1}$ norm encourages sparsity in the solution by minimising the sum of the absolute values of the signal's coefficients. While it does not explicitly count the number of non-zero elements like the ℓ_0 norm, it promotes the selection of fewer large coefficients, leading to a sparse representation of the signal. Importantly, minimisation of the ℓ_1 norm can be solved efficiently using convex optimisation techniques, making it a computationally feasible approach in compressed sensing. The optimisation problem then becomes

$$\hat{\mathbf{s}} = argmin\ \|s\|_1\ subject\ to\ y = A\Psi s \tag{2.7}$$

$\boldsymbol{\ell_2}$ Norm

The ℓ_2 norm, commonly employed in least squares regression, is defined as:

$$\|s\|_2 = \sqrt{\sum_{k=1}^{n} s_k^2} \tag{2.8}$$

The ℓ_2 norm is not inherently sparsity-promoting. Instead, it tends to yield dense solutions where every vector component has some energy. Although effective for approximating solutions in many cases, ℓ_2 norm minimisation is sensitive to outliers, as it squares the errors, giving more weight to large deviations in the data.

Figure 2-3 illustrates this effect by fitting a trendline to linear data from the function $y = kx + b$ with uniformly distributed noise. Six data points were manually altered to simulate large outliers. The red dashed line shows the trendline fitted using the ℓ_2 (least squares) method, which is skewed by the outliers. In contrast, the black line represents the trendline fitted using the ℓ_1 norm. Unlike the ℓ_2 norm, the ℓ_1 norm is less sensitive to outliers because it minimises the absolute errors rather than their squares. As a result, it successfully preserves the overall trend of the data, making it a more robust option for sparse signal recovery in the presence of noisy measurements.

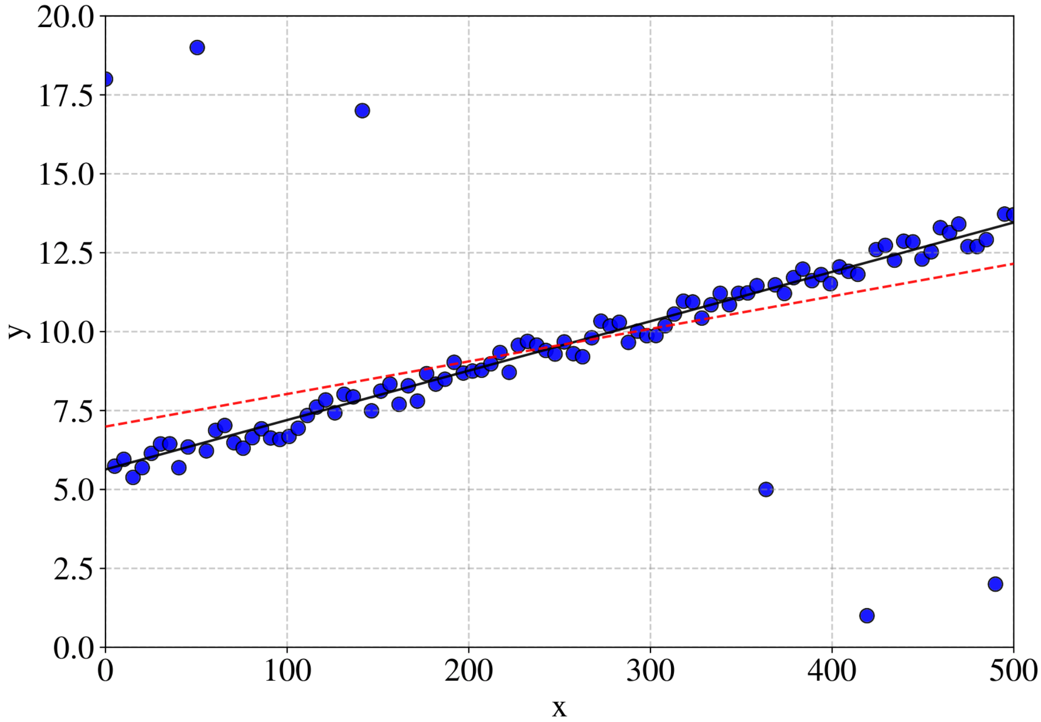

Figure 2-3 Linear data from function $y = kx + b$ with ± 1 uniformally distributed noise. 6 data points were manually edited to imitate large outliers. Red dashed line shows trendline fitted using ℓ_2 i.e. least squares norm and black line shows trendline fitted using ℓ_1.

In many cases, minimising the ℓ_1 norm has been shown to be sufficient for recovering the sparsest solution in compressed sensing. While ℓ_0 minimisation remains the ideal in theory, ℓ_1 norm minimisation provides a computationally practical alternative that can still achieve accurate recovery. The success of ℓ_1 minimisation in sparse recovery has been rigorously proven under certain conditions, such as when the measurement matrix satisfies the Restricted Isometry Property (RIP). This property ensures that the structure of sparse signals is preserved during the measurement process, allowing ℓ_1 norm minimisation to recover the true sparse signal.

The pioneering work of Emmanuel Candès and Terence Tao [14,17] demonstrated that under the presence of RIP (explored in the following section), ℓ_1-norm minimisation is guaranteed to yield the same solution as ℓ_0 minimisation. Thus, ℓ_1 minimisation not only provides a tractable optimisation problem but also promotes the desired sparsity in many practical compressed sensing applications.

Because of this, the signal acquisition process is changed, as illustrated in Figure 2-4. After acquiring the compressed measurements, reconstruction algorithms based on ℓ_1 optimisation can be employed to recover the sparse signal s and in turn get the underlying signal.

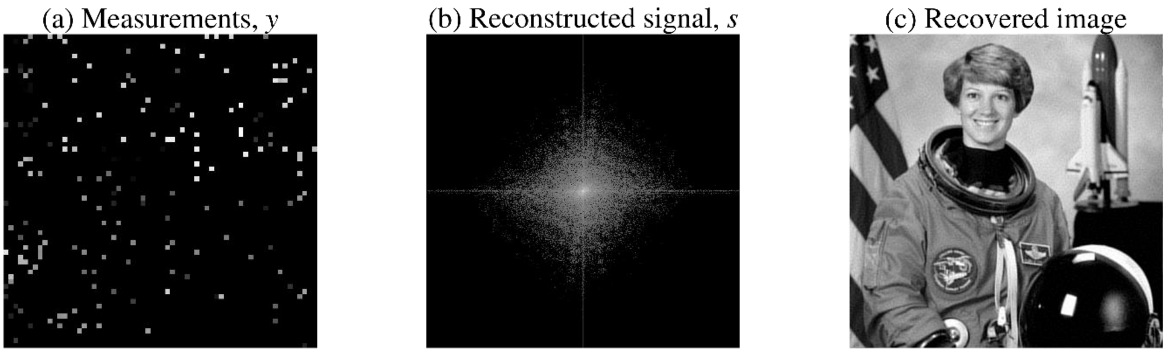

Figure 2-4 Illustration of the compressed sensing recovery process. In (a) the compressed measurements y are illustrated. After acquiring the measurement, ℓ_1 optimisation algorithms are used to reconstruct the sparse signal s, as shown in (b). This signal is the sparsest representation that corresponds with the measurements y. Finally, by applying the inverse of the sparsifying basis (e.g. Fourier or DCT), the original image is recovered, shown in (c).

2.2.3 The restricted isometry property (RIP)

For compressed sensing to be effective, particularly with ℓ_1 minimization techniques, certain conditions must be satisfied, encapsulated by the concept of the Restricted Isometry Property (RIP) [18]. These particularly apply to the measurement matrix A and place conditions on the properties of the measurement matrix. RIP ensures that the measurement matrix maintains the geometry of the sparse signal space, allowing for accurate reconstruction. The key conditions for RIP are:

1. **Incoherence of Measurement Matrix**: The rows of the measurement matrix A must be incoherent with the transform domain used to sparsify the data. An ideal measurement matrix would be completely random [19], ensuring that no particular signal features are favoured during the sampling process.

2. **Sufficient Number of Measurements**: The number of measurements must be sufficiently large, typically on the order of:

$$p \gtrsim k_1 K \log\left(\frac{n}{K}\right) \tag{2.9}$$

where k_1 is a constant related to the coherence between the measurement matrix A and the measured signal, and K is the sparsity level i.e. the number of non-zero entries in the signal. This condition ensures that the sampling adequately captures the essential features of the sparse signal, without distorting its structure.

2.2.4 Choosing measurement matrices

The choice of a measurement matrix is a critical factor in determining the success of compressed sensing-based reconstructions, as highlighted by the RIP.

Figure 2-5 shows several examples of measurement matrices that satisfy the RIP condition, making them suitable for compressed sensing applications. Single-pixel random measurement matrix, shown in subfigure (a) samples a single random point in the signal space at a time. Each row of the matrix corresponds to a single measurement of the signal, and it contains only one "1" (black pixel) while the rest of the entries are "0" (white pixels). In some applications, this can be impractical, as measuring only a single point in a large signal space can lead to poor signal-to-noise ratios. Conceptually this is similar to performing a point-by-point scan, except that instead of moving between pixels in order, the measured points are randomised.

Random patterned measurement matrix, shown in subfigure (b) samples multiple points in the signal space simultaneously. Each row corresponds to a measurement that combines the values of several points in the signal. This is achieved by setting multiple entries per row to "1", with the remaining entries set to "0". By sampling multiple points at once, the amount of signal captured with each measurement is increased. It is important to note that the sparsity of this type of measurement matrix—the proportion of 1s to 0s in each row—is crucial. For each measurement, the ratio of 1s to 0s must remain constant, though the ratio can take on any value, depending on what is most suitable for the measurement.

Walsh-Hadamard Transform (WHT) measurement matrix is shown in subfigure (c). The WHT matrix is an efficient and widely used option for compressed sensing [20]. Its operational principle is similar to that of the random patterned measurement matrix in that it measures the combined response of several points in the signal space. However, the WHT matrix has a significant advantage: it is computationally easier to generate and does not need to be stored explicitly. Instead of storing a large matrix, each row of the WHT matrix can be computed on demand during the reconstruction process. This makes WHT matrices highly scalable and suitable for high-resolution signals, as they avoid the problem of prohibitive storage requirements faced by random sampling matrices.

For any compressed sensing-based reconstruction, the measurement matrix must be known in advance, as it provides the spatial information necessary for reconstructing the signal. As the resolution of the signal increases, the size of the measurement matrix required grows rapidly. Random measurement matrices, while theoretically sound, can become prohibitively large and difficult to manage for high-resolution signals due to the need to store each random pattern used during the measurement process. In contrast, the WHT-based measurement matrix scales efficiently and is particularly useful for large-scale applications. The full measurement matrix for a 100×100 pixel image would be $100^2 \times 100^2$, which quickly exceeds computer memory capacity. More generally, for an image with $j \times k$ pixels, the measurement matrix A has dimensions of $m \times (j \times k)$ entries, where m is the number of measurements. When referring to the sampling rate, $m = j \times k \times sampling\_rate$

It is important to note that, mathematically, the entries of the measurement matrix do not have to be binary (i.e., consisting of just "1"s and "0"s). In fact, the measurement points can take on any values, making non-binary matrices theoretically viable. However, building a physical system based on non-binary measurement matrices introduces significant complexity and is typically not feasible in practical applications. For this reason, binary measurement matrices are preferred in real-world implementations of compressed sensing.

There are also examples in the literature of purpose-generated measurement matrices. When the signal space is well understood, a tailored measurement matrix can be designed to better match the structure of the underlying signal. This allows for more efficient signal recovery, as the matrix can focus on the key features of the signal, reducing the number of measurements needed. Such matrices are particularly useful in applications like medical imaging or radar, where the signal characteristics are predictable, making it possible to optimise the measurement process.

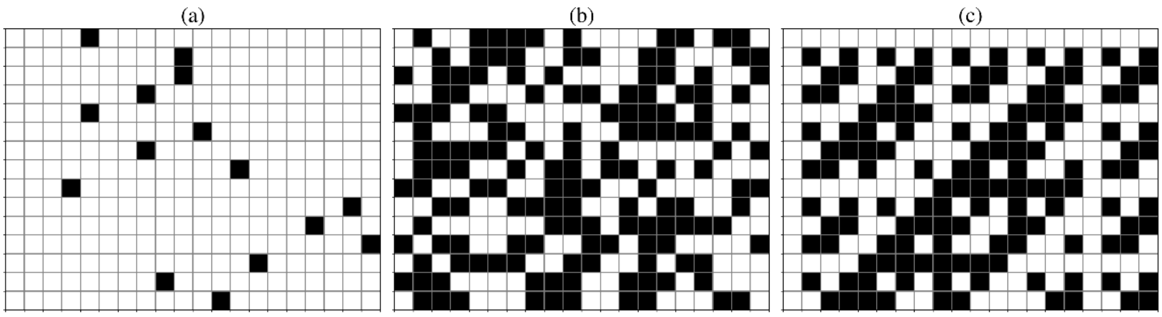

Figure 2-5 Examples of good measurement matrices for compressed sensing (a) single pixel random matrix, (b) random patterned matrix (c) Walsh-Hadamard Transform matrix. Every row of the matrix represents a measurement.

In contrast to the suitable measurement matrices demonstrated above, Figure 2-6 illustrates some examples of measurement matrices unsuitable for compressed sensing. The structured diagonal matrix in Figure 2-6 (a) lacks randomness, resulting in measurements that are highly correlated with the original signal, similar to a raster scan. This high coherence violates the RIP, making accurate signal reconstruction highly improbable. Similarly, the periodic matrix in (b) fails to provide sufficient diversity in the measurements, as the repetitive patterns leave large parts of the signal unmeasured. Both examples highlight how poor measurement design can lead to significant portions of the signal being missed, resulting in artefacts in the reconstructed signal or complete reconstruction failure.

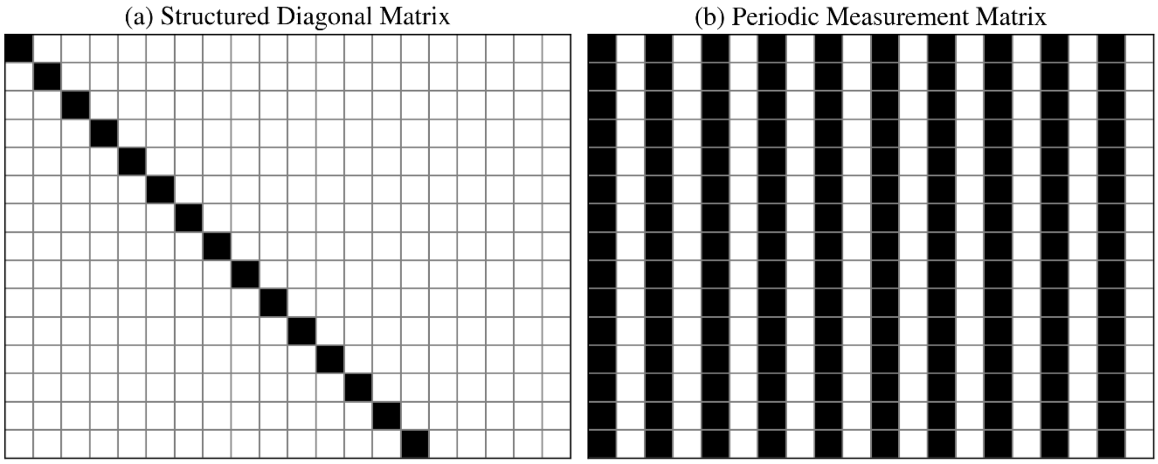

Figure 2-6 Examples of unsuitable measurement matrices for compressed sensing. (a) A structured diagonal matrix, analogous to a raster scan measurement, where measurements lack randomness. (b) A periodic measurement matrix with repetitive patterns. In both examples, the signal is not uniformly sampled, leaving parts of the signal unmeasured and failing to meet the RIP.

2.3 Compressed sensing reconstruction algorithms

Compressed sensing has led to the development of numerous algorithms aimed at recovering sparse signals from undersampled measurements. Interestingly, while ℓ_1 optimisation algorithms predate compressed sensing theory, it is the advancements in computer science over the last two decades that have enabled the practical application of compressed sensing in various fields. These algorithms can be broadly divided into two categories: greedy algorithms and convex relaxation methods. This section provides a general overview of the commonly used algorithms and justifies the specific approach employed in this work. The development of compressed sensing algorithms remains an active area of research, with further details available in references [21,22].

2.3.1 Greedy algorithms

Greedy algorithms have emerged as a significant approach in the field of compressed sensing, particularly for the reconstruction of sparse signals from limited measurements. These algorithms operate under the principle of making locally optimal choices at each step with the hope of achieving a globally optimal solution. Although they often do not guarantee a global optimum, their efficiency and lower computational complexity make them attractive alternatives to traditional convex optimization methods, which can be computationally intensive, especially as the size of the original signal increases [23,24].

One of the most widely used greedy algorithms in compressed sensing is Orthogonal Matching Pursuit (OMP) [25]. OMP iteratively selects the measurement that correlates most with the residual signal, thereby building a sparse representation of the original signal. Despite its popularity, OMP has limitations, including relatively poor reconstruction accuracy and high computational demands, particularly in noisy environments [26,27]. To address these issues, more advanced greedy algorithms have been developed, such as Compressed Sampling Matching Pursuit (CoSaMP) and Subspace Pursuit (SP). These algorithms incorporate backtracking refinement techniques, which enhance robustness against noise and improve theoretical guarantees for signal recovery [26,28].

The performance of greedy algorithms can be further enhanced through various modifications. For instance, reweighted greedy algorithms have been proposed to improve recovery accuracy by adjusting the weights assigned to different components of the signal during the reconstruction process [29]. Additionally, the integration of cross-validation techniques has been explored to optimise the stopping criteria for greedy algorithms, allowing for better adaptation to the specific characteristics of the signal being reconstructed [30]. These advancements highlight the ongoing evolution of greedy algorithms in compressed sensing, as researchers strive to balance computational efficiency with recovery performance.

2.3.2 Convex optimisation algorithms

Convex optimisation algorithms are a cornerstone of compressed sensing, providing a robust framework for reconstructing sparse signals from limited measurements. These algorithms leverage the properties of convex functions to ensure that any local minimum is also a global minimum, which is particularly advantageous in signal recovery tasks. The core principle of compressed sensing is to reconstruct a signal that can be sparsely represented from fewer samples than traditionally required, thereby enabling efficient data acquisition and processing [31].

Among the various convex optimisation techniques, the ℓ_1 minimisation approach is particularly notable. This method seeks to minimise the ℓ_1 norm of the signal, which promotes sparsity in the solution. The ℓ_1 minimisation has been shown to yield high reconstruction accuracy while requiring fewer measurements compared to other methods [32,33]. However, these advantages come at the cost of increased computational complexity, as the optimisation problems can be challenging to solve, especially in real-time applications [34]. Despite this, advancements in algorithms such as the Alternating Direction Method of Multipliers (ADMM) and proximal gradient methods have improved the efficiency of convex optimisation techniques, making them more applicable in practical scenarios [35,36].

Convex optimisation algorithms are also versatile, as they can incorporate various regularisation techniques to enhance performance. For instance, incorporating prior knowledge about the signal structure can lead to better recovery outcomes. This adaptability allows for the development of tailored algorithms that can address specific challenges in signal reconstruction, such as noise and measurement errors [37]. Furthermore, the integration of convex optimisation with machine learning techniques has opened new avenues for improving the robustness and accuracy of compressed sensing reconstruction [38].

Overall, convex optimisation algorithms play a vital role in the field of compressed sensing, offering a mathematically sound approach to signal reconstruction that balances accuracy and computational efficiency. While they may require more resources than greedy algorithms, their ability to guarantee global optimality and adapt to various signal characteristics makes them indispensable in modern signal processing applications.

2.3.3 Algorithm selection

SPGL1 [39,40], or Spectral Projected Gradient for ℓ_1 minimisation, is a widely used algorithm for solving large-scale convex optimisation problems, particularly in the context of compressed sensing. Designed to efficiently recover sparse signals from undersampled measurements, SPGL1 is especially effective for underdetermined linear systems, where the goal is to minimise the ℓ_1 norm of the signal subject to linear constraints. The algorithm leverages a spectral projected gradient method, combining gradient descent with projection techniques to navigate the solution space efficiently while maintaining sparsity in the reconstructed signal. Its adaptability to large-scale problems and efficient handling of high-dimensional data makes it a suitable choice for many compressed sensing applications.

SPGL1 operates iteratively, updating the estimate of the sparse signal by computing the gradient of the objective function and projecting the solution onto the feasible set defined by the linear constraints. This projection step is crucial, as it ensures the solution remains within the bounds of the original problem while promoting sparsity through ℓ_1 norm minimisation [11].

Due to its strong performance in previous work, SPGL1 was predominantly used in this research. Both the original *Matlab* version [39] and a *Python* wrapper [41] were used. Additionally, for exploring higher resolution images, a modified version of the algorithm, developed by Andrew Thompson was used [20]. The decision to use SPGL1 was motivated by its proven reliability in compressed sensing reconstructions in similar applications [42,43], where the algorithm demonstrated excellent performance in terms of both reconstruction quality and computational speed.

The modifications to the algorithm extended the capabilities of the standard SPGL1, enabling it to process higher-resolution data that would typically challenge other algorithms, with examples going up to 1 megapixel reconstructions [42].

2.4 Compressed sensing applications

As mentioned in previous sections, compressed sensing has found applications in a variety of disciplines due to its ability to reconstruct sparse signals from undersampled data. One of the first practical demonstrations of compressed sensing theory was the single-pixel camera, developed by Duarte et al. [44]. This setup utilised a single photodiode, paired with a digital micromirror device (DMD), to capture images. The innovation lay in the simplicity and cost-effectiveness of this camera design, which allowed it to operate efficiently across a broader spectral range than conventional silicon-based cameras. While this design imposed higher computational requirements during the reconstruction phase, it provided significant advantages in applications that required more spectral versatility, especially in non-visible wavelengths. By reflecting the sample's light off a DMD before focusing it onto the photodiode, the system could capture information that was then reconstructed into a high-resolution image using CS algorithms. They also proposed that this principle could be adapted with more sophisticated detectors, such as photomultiplier tubes (PMTs) or avalanche photodiodes (APDs), for low-light imaging, or even spectrometers for hyperspectral imaging. This early work correctly highlighted the potential of compressed sensing to significantly enhance the performance and reduce the cost of existing systems by shifting the complexity from the data acquisition phase to the data reconstruction phase.

One of the most impactful applications of compressed sensing has been in the medical field, particularly in Magnetic Resonance Imaging (MRI). MRI has been a critical diagnostic tool since the 1970s, widely used for diagnosing various medical conditions, including cancer, without the risks associated with ionising radiation. Despite its utility, MRI is inherently a slow imaging modality due to the need to acquire large volumes of data in multiple dimensions. In 2007, Lustig, Donoho, and Pauly [10] applied compressed sensing theory to MRI to accelerate image acquisition, significantly reducing scan times while maintaining image quality. This breakthrough fundamentally changed MRI acquisition protocols and has since become a standard approach in clinical practice, spurring numerous follow-up studies and improvements. The use of compressed sensing in MRI enables the capture of sufficient diagnostic information with fewer measurements, reducing patient discomfort and risks associated with prolonged scanning times, such as claustrophobia and movement artefacts.

Beyond MRI, compressed sensing has found other applications in biomedicine. For example, CS has been applied to Electroencephalogram (EEG) data to improve the resolution and quality of brain activity measurements [45]. Traditional EEGs are limited by low spatial resolution due to the sparse placement of electrodes. By applying compressed sensing, it is possible to reconstruct more detailed signals, offering better insights into neurological activity with fewer sensors. Similarly, compressed sensing has been explored in DNA sequencing to improve the speed of sequencing without compromising accuracy [46]. With the vast amount of data produced in genomic studies, compressed sensing has shown potential to reduce the amount of data that needs to be physically collected, speeding up the sequencing process and reducing costs.

In microbiology, compressed sensing has been applied to the reconstruction of bacterial communities from sparse genetic data [47]. In complex microbial environments, traditional methods struggle to capture the full diversity of species due to incomplete sampling. Compressed sensing enables the reconstruction of these communities from fewer samples by exploiting the natural sparsity in the genetic data, thus providing more comprehensive insights into microbial diversity and dynamics.

2.4.1 Semiconductor characterisation using compressed sensing

Compressed sensing has also been applied in semiconductor characterisation, particularly in improving the efficiency and resolution of various measurement techniques. Traditionally, many characterisation methods in the semiconductor industry, such as photoluminescence (PL) imaging or current mapping, rely on raster scanning, which is slow and inefficient due to the need to measure each point on the sample individually. Compressed sensing offers a promising alternative by significantly reducing the number of measurements required, thus speeding up data acquisition while maintaining or even improving resolution.

One area where compressed sensing has been successfully applied is in photovoltaic (PV) device characterisation, particularly for current mapping. Conventional methods, such as the light beam induced current (LBIC) method, typically involve scanning the sample point by point, where a light beam is focused on a single spot and the resulting current is measured. This is usually done by moving the sample with an XY stage. However, this approach is time-consuming, as it requires scanning the entire sample, even in areas where the response may be redundant, especially for uniform devices. Additionally, measuring current at a single point can be inefficient, as the signal might be weak or even lost, depending on the area of excitation.

Compressed sensing offers a more efficient alternative by exciting the PV device with patterned illumination rather than a single point of light. This patterned excitation increases the overall current response by engaging larger regions of the device simultaneously, ensuring a stronger signal and reducing the likelihood of missing weak responses. Through compressed sensing, it is possible to reconstruct a high-resolution current map from fewer measurements, as the technique leverages the sparsity of the signal. This not only speeds up the measurement process but also improves the overall signal strength, making it particularly beneficial for large-scale PV devices. Several studies [42,48–50] have shown that compressed sensing can drastically reduce the number of measurements needed while maintaining accurate reconstructions of the current map. The ability to avoid redundant data collection and increase signal response makes compressed sensing a highly efficient approach for characterising photovoltaic devices, with the potential to significantly enhance throughput in both research and industrial applications.

2.5 Summary

This chapter presented the foundational principles and applications of compressed sensing theory essential for the research conducted in this thesis. The core idea of compressed sensing revolves around the concept of signal sparsity. While natural signals can often be compressed and described with far less data than typically required, compressed sensing seeks to acquire the compressed data directly without first acquiring the full signal. In conventional measurement techniques, the amount of information provided by each measurement is varied, whereas in compressed sensing, every measurement provides the same amount of information. By exploiting the sparsity inherent in many signals, compressed sensing significantly reduces the number of measurements needed. In imaging, this can be as low as few percent, compared to scanning approaches.

The mathematical framework of compressed sensing is introduced, providing an overview relevant from engineering perspective. As the spatial information is encoded into the measurement itself in the form of measurement matrix, examples of both effective and ineffective measurement matrices are provided. The overall requirements for compressed sensing are encapsulated by the RIP, providing limits on measurement coherence and number.

On the reconstruction side, the chapter explores two main categories of algorithms used to recover signals from compressed sensing data – greedy algorithms and convex optimisation algorithms. SPGL1 algorithm is highlighted as the algorithm predominantly used in this thesis, due to its effectiveness of handling higher resolution reconstructions. Examples from both semiconductor characterisation and broader fields, such as medical imaging, highlight the practical applications and potential of compressed sensing across various disciplines. Whilst applications of compressed sensing for semiconductor characterisation are still relatively few, the existing ones are demonstrated.

Some further theory and concepts are introduced and detailed in other chapters as needed.

Chapter 3 Modelling of Compressed Sensing Time-Resolved Photoluminescence Measurements

Before building the compressed sensing time-resolved photoluminescence (TRPL) prototype system, it was necessary to test the methodology through simulations. No literature was available at the time of writing on compressed sensing TRPL. The closest examples are presented by Karel Žídek [51–53] showing applications of compressed sensing for spectroscopy applications and fluorescence imaging. Therefore, before performing experimental testing and investing into procuring the necessary experimental equipment, it was useful to first explore the feasibility of the methodology through simulations. The chosen approach for this was using numerical simulations in *Python* [54]. The aim of this work was to model a photon counting experiment together with masking of a virtual sample and test if the data can be reconstructed through the techniques described by compressed sensing theory. Additionally, the developed computational model could be utilised to estimate the experimental limitations, such as sensitivity to noise or susceptibility to photon pile-up effects. Because such methodology had not been previously demonstrated, the exact method for reconstructing such data was not immediately clear either but was developed using the computational model.

Before beginning the simulation development, background information on TRPL and time-correlated single-photon counting (TCSPC) is provided. An overview of charge carrier lifetimes is included, along with an explanation of how these are measured using TRPL. Since TRPL signals are typically too weak to be measured directly, the TCSPC technique is employed to accumulate measurements over multiple excitation pulses, enhancing signal detection.

This is then followed by detailed explanation of the simulation work carried out. Each section goes through the various parts and functions involved in both the measurement and reconstruction simulations. The work starts off with building a Monte-Carlo [12] type simulation to test the TCSPC approach, assessing the effects of photon pile-up and TCSPC measurements from multiple sources.

Each subsequent subsection builds on the previous and adds additional functions and layers to move closer towards building a complete model. Some work was also carried out to simulate compressed sensing for spectral measurements. The different approaches to reconstruction and different reconstruction algorithms are also detailed and considered.

The final model is used to assess the effects of compressed sensing measurement parameters and noise, providing a foundation for subsequent experimental work. Results are presented for two different virtual samples with different measurement parameters being varied. The parameters tested were the number of measurements and the number of laser pulses. SSIM [55] metrics were used to compare the reconstructed images to the 'ground truth' reference images to quantify the quality of reconstructions. The final section of the chapter contains details of how measurement noise was simulated and added to the model. The reconstruction was then carried out keeping a constant sampling level but varying the degrees of noise and monitoring how the quality of the reconstruction is affected. The findings then indicate the amount of noise that would be permissible in a physical prototype system to ensure a reconstruction can still be reliably carried out.

Overall, before carrying on with the full system design it was first beneficial to analyse the methodology through numerical simulations. The goal of this was to establish feasibility, determine measurement and reconstruction requirements, and consider effects of various sources of noise.

3.1 Time-resolved photoluminescence

TRPL is a measurement technique used for measuring the charge carrier lifetimes. Charge carrier lifetime is defined by the average time it takes for an electron-hole pair to recombine. The theory for recombination processes has been around since 1950s when it was first proposed in works by Shockley, Read and Hall [56,57]. Measuring carrier lifetime provides information about defect densities within the material. Therefore, it has become almost a standard measurement by industry and academia to define material and device quality [58].

However, to have confidence in the measurement, it is important to understand exactly what property was measured. The measurement results vary between different methods for the same material. The difficulty in accurately defining carrier lifetime is due to it being a property not inherent to the semiconductor but rather a property of a carrier within the semiconductor. Furthermore, whilst the measurement is usually quoted as a single value, it is actually a weighted average of carriers within the sample, influenced by defects, surfaces, temperature and others [59].

The measured lifetimes are always effective lifetimes. They are a combination of bulk recombination, i.e. happening within the semiconductor and surface recombination. These events occur simultaneously and are typically difficult to separate. Therefore, it is important to consider properties, such as wavelength and material thickness to understand the influence of both. The recombination lifetime is defined as:

$$\tau_r = \frac{\Delta n}{R} \tag{3.1}$$

Where Δn is the excess carrier density and R is the bulk recombination rate. The bulk recombination rate is determined by 3 key mechanisms: Defect or Shockley-Read-Hall (SRH) recombination, where a carrier combines non-radiatively by emitting a phonon; Radiative recombination where an electron recombines with a hole by emitting a photon and Auger recombination where the recombination energy is absorbed by a third carrier. These mechanisms are illustrated in Figure 3-1. Therefore, the recombination lifetime τ_r is given by:

$$\tau_r = \frac{1}{\tau_{SRH}^{-1} + \tau_{rad}^{-1} + \tau_{Auger}^{-1}} \tag{3.2}$$

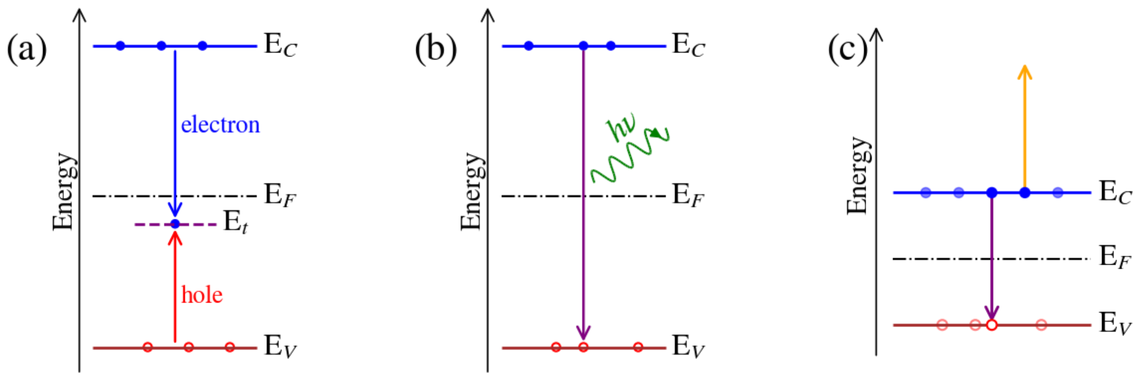

Figure 3-1 The different carrier recombination paths for injected current (electrons shown as filled circles, holes - empty) - (a) showing a defect or Shockley-Read-Hall recombination caused by vacancies in the periodicity of the crystal forming a deep energy level (b) shows radiative recombination, where electron recombines with a hole by emitting a photon, (c) shows an Auger process [60].

At lower carrier densities, the carrier lifetime is primarily dominated by SRH recombination [61]. Therefore, measuring the lifetime gives a good indication of the material quality. The higher lifetime is particularly important in photovoltaic devices, where the excess electron concentration is directly related to the voltage.

3.2 Time-correlated single-photon counting

To accurately capture the rapid and faint signals observed in TRPL, a commonly used technique is TCSPC. The origins of TCSPC can be found in particle physics, back in the 1930s. [62]. In 1961, Bollinger and Thomas extended scintillation counting to encompass various types of radiation [63]. Around the same time, flash lamps with pulse widths of around ~2 ns became available, allowing increased timing precision in photon counting experiments [64]. The method gained traction in the early 1970s for measuring fluorescence decays [65,66]. The measurement speed and accuracy drastically improved in the 1980s with the introduction of picosecond-pulse lasers with megahertz repetition rates [67,68]. These advancements established TCSPC as a key technique in fluorescence lifetime imaging microscopy (FLIM) and subsequently in TRPL measurements in semiconductors.

There are two primary advantages of using TCSPC to acquire TRPL compared to other methods. First, the PL decays in semiconductor materials are very rapid – typically ranging around few ns, although they can go up to μs. Other detector and/or measurement systems lack the speed necessary to capture such fast signals accurately. Secondly, the emitted PL signal is extremely faint and without the use of TCSPC would most likely be indistinguishable from background. This attribute is particularly advantageous for the main objective of this project, aimed at developing a TRPL imaging setup for measuring the entire area of interest simultaneously. By acquiring the information over series of excitation pulses, TCSPC significantly enhances signal-to-noise ratio.

The technique requires a pulsed laser with high-repetition rate, single photon detector and fast digital timing electronics. During TCSPC measurement, each laser pulse serves as a reference, indicated as red pulses in Figure 3-2. Following some of the excitation pulses, a photon gets registered at time τ after the excitation pulse (indicated as yellow circles in Figure 3-2), which gets processed by TCSPC electronics, allocating the arrival time to a specific time bin. The cycle is repeated over many excitation cycles, until enough photons are detected. The resulting histogram of photon arrivals per time bin represents the time decay one would have obtained from a 'single shot' time-resolved analogue recording, provided that the probability of registering more than one photon per cycle is low. This means the scenario shown after the 4th laser pulse in Figure 3-2 must be minimized. Literature commonly quotes that on average, a PL photon should only be detected after at most 5% of excitation pulses to avoid photon pile-up effect [69]. Photon pile-up effect is when multiple photons arrive at the detector within a single excitation pulse. Due to the nature of TCSPC timing electronics, only a single detection event can occur after a given reference pulse. If multiple photons frequently reach the detector, the measured decay will not accurately represent the intrinsic decay curve of the sample, resulting in shortening of the measured intrinsic decay lifetime. This TCSPC measurement methodology, including the pile-up effect is explored through simulations in Section 3.3 . Physical implementation of TCSPC is detailed in Chapter 4.

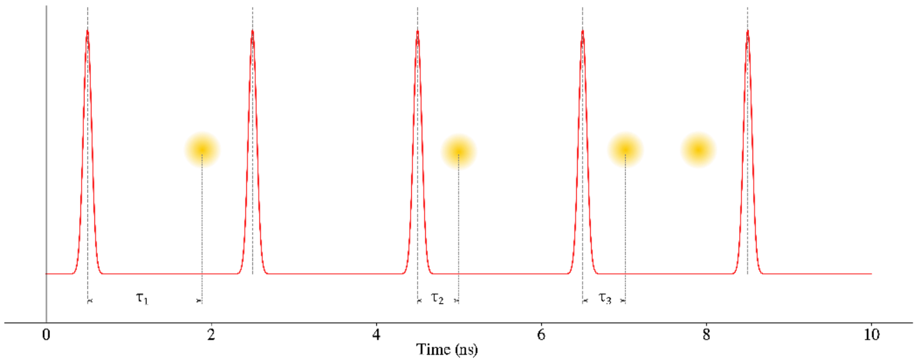

Figure 3-2 Principle of TCSPC method. The red line shows the laser intensity as a function of time. The yellow circles indicate a time at which a photon is registered by the detector. This process is repeated over multiple excitation pulses and the detection time is registered for each pulse. Note that the detector is only able to recognise a single photon per given laser pulse. Therefore, care has to be taken to minimize the probability of multiple photons hitting the detector within the same excitation pulse.

3.3 Developing TCSPC simulation

Flowchart in Figure 3-3 outlines the steps involved in simulating data acquisition of TCSPC. There are 3 key parameters used for this simulation: 1) lifetime (τ_i) of the measured pixel, 2) mean number of photons detected per laser pulse (MNOP), and 3) the number of laser pulses. In the case where the mean number of photons detected per laser pulse is low, i.e., $\ll 1$, the probability of detecting a photon $p \approx MNOP$.

The simulation runs in a loop, starting with the emission of a laser pulse. After each pulse, a condition is checked to determine if the pulse resulted in a photon being detected. If the condition is not met, the algorithm moves on to the next pulse and performs the check again. Once the condition is met, a number is drawn from the exponential distribution, generated using the τ_i parameter – this determines the photon arrival time at the detector. The next stage in the simulation is determining whether multiple photons reached the detector within a given pulse. Due to stochastic nature of PL emission, multiple photons might arrive at the detector between the laser pulses. However, the detectors used in TCSPC setups are only capable of recording a single photon after a laser pulse. Therefore, if multiple photons reach the detector, only the first one would be recorded. To simulate this, after each PL emission event, a random number is drawn to determine if another photon reached the detector during the same pulse. Number of photons arriving at the detector are simulated this way and the arrival time of each of them is determined. The check is performed until no more photons are recorded. At this point, only the photon with the shortest arrival time is recorded and the rest are discarded. The photon arrival time gets placed into a histogram, where the width of each bin of the histogram represents the temporal resolution of the measurement. The loop then goes to the next laser pulse, starting the process again. The whole cycle repeats for a fixed number of laser pulses, populating the histogram, as indicated in Figure 3-4. After a large number of pulses, typically $10^7 - 10^8$, the histogram becomes equivalent to the TRPL response of the measured area. These assumptions work in the limit that the pixel size is large compared to the diffusion length.

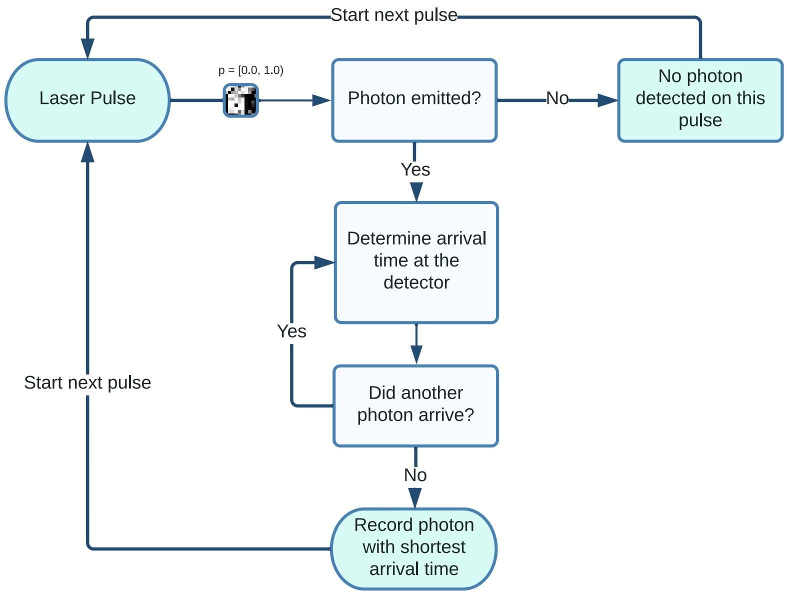

Figure 3-3 Flowchart indicating the TCSPC measurement process. Typically, laser pulses are repeated for a predetermined number of pulses.

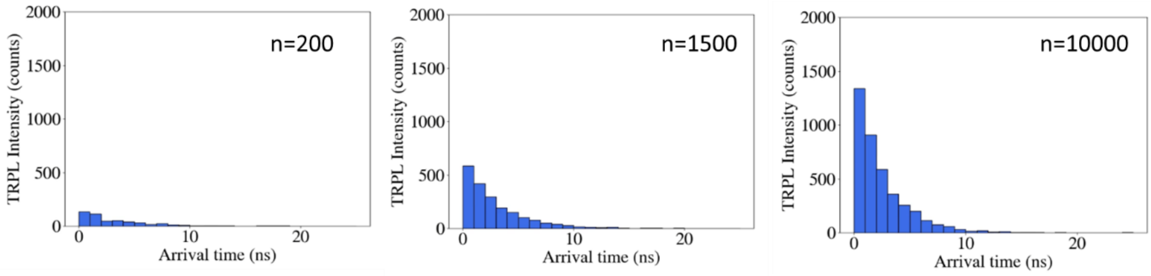

Figure 3-4 Example of TCSPC process building up a TRPL response by repeating the measurement process. The n corresponds to the number of laser pulses used. By plotting the arrival times of the photons as a histogram, the overall TRPL of the sample arises.

3.3.1 Determining decay constant

To fit the resulting TRPL curves, a non-linear least squares fitting algorithm is well suited. An implementation of this provided by `scipy.optimize.curve_fit` [70] was used in this work, which is based on Levenberg-Marquardt algorithm [71,72]. The algorithm takes data to be fitted, initial guess parameters and the model function as inputs and returns the optimal parameters to describe the function. By performing the fit, the TRPL measurements can be defined by a single number τ.

The fitting algorithm additionally returns the covariance matrix which is useful to determine the accuracy of the fit. In simulated measurements, the fitting is relatively straightforward as all the results are drawn from the exponential distribution to begin with. In real measurements, the fitting becomes more complex as multiple recombination methods are present as well as dark counts and other sources of measurement uncertainty, making the fitting more complicated. The fitting process for real measurements is explained in more detail in Chapter 4.

3.3.2 Simulating photon pile-up

As mentioned in the previous section, TCSPC systems are prone to photon pile-up effect where the system becomes biased towards detecting earlier recombination events. This effect appears due to PL emission following Poisson statistics at low excitation levels [73]. The implication of this is that a probability always exist that a pulse will result in multiple photons reaching detector within a single cycle. However, due to the nature of PMT and counting experiments in general, only the first photon will be recorded as the dead time of the detector is larger than the time between laser pulses. Additionally, the timing of TCSPC measures the reference time between the laser pulse and the arrival event. Therefore, by increasing the probability of multiple photons reaching the detector, the system bias towards detecting faster photons is increased.

```
def meanphotons(p, pulses):
    mnop = []
    for i in range(0, pulses):
        emitted = 0
        pl_prob = np.random.random()
        while pl_prob < p:
            emitted +=1
            pl_prob = np.random.random()  # checks if another photon is
emitted. Can result in almost infinite loop as prob approaches 1
        mnop.append(emitted)
    return np.mean(mnop)
```

Figure 3-5 Code snippet used for numerically determining the mean number of photons per pulse from probability of photon detection. A number is repeatedly drawn from uniform distribution and compared against the probability parameter to determine the number of photons in a single pulse.

Literature commonly refers to keeping the $MNOP$ below 0.05 to prevent introducing this systematic error [64,74]. Above this value, the probability of multiple photons reaching the detector increases, leading to the system becoming biased towards detecting shorter lifetimes and resulting in shorter measured lifetimes. This process can be investigated by varying the probability parameter p mentioned in the previous section and measuring the change in measured decay constant. The outcomes of this are shown in Figure 3-6. The blue circles indicate the lifetime measured after simulating the TCSPC measurement, showing a clear reduction in measured lifetimes as the probability is increased. To explain this, it was useful to look at the average number of undetected photons for each laser pulse. This was calculated by determining the MNOP at each probability using the function shown in Figure 3-5. After determining MNOP, the probability was subtracted leaving the average number of undetected or excess photons per pulse at each probability. We can see that as the probability increases, there are more and more photons which would be completely missed by the detector. From the code snippet, we can see that as $p \to 1, MNOP \to \infty$.

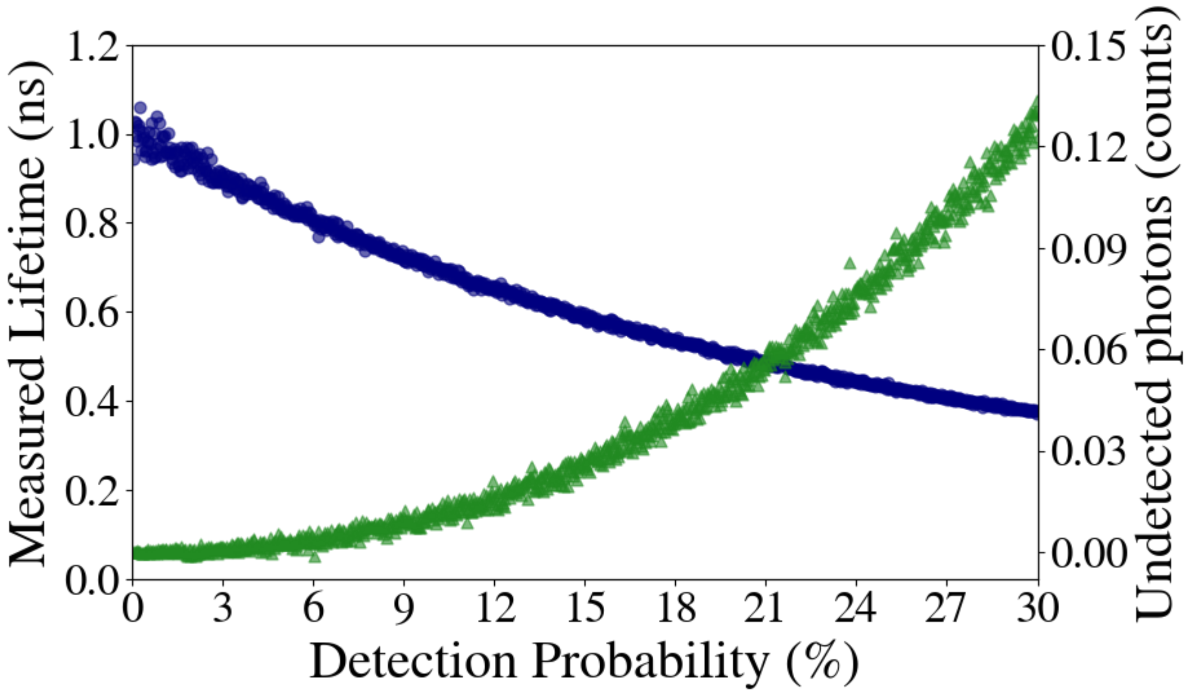

Figure 3-6 Investigation of photon pile-up effects in TCSPC simulation. Blue circles show what lifetime was measured as the probability of detecting a photon on each laser pulse was increased. As the probability of detecting a photon increases, the MNOP rises as well, leading to multiple photons arriving at the detector in the same laser pulse. Green triangles show the average number of photons undetected on each excitation pulse. This is calculated by subtracting the detection probability from the MNOP detected emitted.

3.3.3 TCSPC from multiple sources

For the purpose of simulating compressed sensing TCSPC measurements, it was also beneficial to understand how the measured lifetimes are affected when broader areas of samples are excited. What happens in the case when within the excited area, there are two areas with specific average lifetimes? When applying compressed sensing TCSPC, a whole area of interest will be excited and a combined response from the whole area will be seen. Understanding how the measurements interact helps in building an appropriate reconstruction model.

To simulate this, a virtual sample was defined consisting of 100 cells. The lifetime of each of those cells was set to 1 ns and the response for the whole sample measured, resulting in a measurement of 1 ns, as expected. The model was set up so that only a single, random cell could emit a photon on every laser pulse. Then, one of those cells was replaced with a 10 ns cell, and the measurement repeated, recording the measured lifetime of the whole sample. The number of longer lifetime cells was increased gradually until the whole sample only had longer lifetime cells. Figure 3-7 shows the lifetimes measured as a function of shorter and longer lifetime cell ratios. A non-linear behaviour was observed – the measured lifetime appears to be more heavily weighted by shorter lifetimes. This implies that when measuring a sample point with features smaller than the excitation spot, the overall measured lifetime is likely dominated by the shortest recombination time within the illuminated area.

The ability to measure single or multiple time constants using the single-pixel imaging concept is rooted in the fundamental principle that each pattern projected onto the sample excites different spatial regions with potentially different charge carrier lifetimes. When considering a simplified case of a sample with two subcomponents having distinct lifetimes (e.g., 1 ns and 10 ns as in this simulation), the resulting decay curve represents a weighted sum of exponential functions. This can be expressed as:

$$I(t) = A_1 e^{-\frac{t}{\tau_1}} + A_2 e^{-\frac{t}{\tau_2}} \tag{3.3}$$

In a real sample, with a range of decay constants, the above would become a weighted average of all the different decay constants. The non-linear relationship between measured lifetimes and the ratio of components with different lifetimes (as demonstrated in Figure 3-7) has important implications for the single-pixel imaging approach. This non-linearity means that as sample complexity increases—for instance, when moving from two distinct lifetime regions to multiple regions with a continuous distribution of lifetimes—the measured signal becomes increasingly dominated by shorter lifetime components. Therefore, reconstructing the spatial distribution of these lifetimes across the sample via compressed sensing algorithms would no longer be possible as the measurements are no longer a linear combination of contributions from each spatial position.

Instead, by considering the PL intensities at each time slice individually, the contribution to the particular time slice follows the additive basis required by compressed sensing. At each time point t after excitation, the measured intensity is a linear combination of contributions from each spatial position within the area excited by the pattern. This linearity at each time point enables the use of compressed sensing reconstruction techniques, even though the overall lifetime behaviour exhibits non-linearity.

However, this does introduce some limitations on the applicability of compressed sensing to TRPL imaging techniques. The inherent bias towards shorter lifetimes may obscure longer lifetime components, especially when they represent a smaller fraction of the excited area, potentially limiting the dynamic range of detectable lifetime differences. The technique also assumes photostability throughout the measurement period, which may not always be the case, depending on the material being tested.

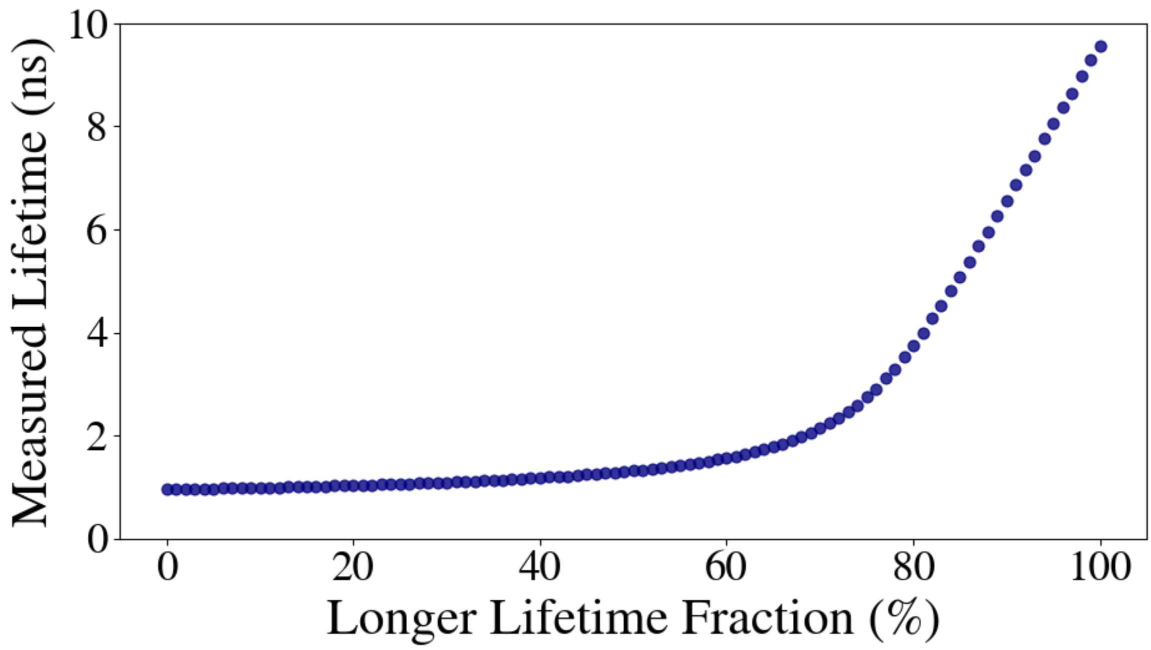

Figure 3-7 This figure assumes a broad area of the sample is excited and the lifetime measured for the whole area. The whole area of the sample consists of short (1 ns) and long (10 ns) lifetime cells. The fraction of long lifetime cells was increased gradually until the whole area consisted only of long lifetime cells. The resulting measured lifetimes show a non-linear behaviour of a TCSPC measurement – the measured lifetimes are more heavily weighted by shorter lifetimes.

3.4 Compressed sensing simulation

3.4.1 1D compressed sensing simulations.

One of the most straightforward implementations of compressed sensing is in the case of one-dimensional signals. Traditionally in order to effectively sample all of the frequencies of interest within the signal Shannon-speckle limit must be satisfied [9]. The limit specifies that the minimum sampling rate must be at least twice the signal's bandwidth in order to reliably acquire the underlying signal. However, by applying compressed sensing theory, this requirement can be relaxed when the signal is sparse in some domain, enabling accurate recovery from sub-Nyquist measurements.

A simulation can be developed by sampling a signal at random points in time with precisely known timing. A reconstruction can then be performed based on the values measured at these points of time to extract the full overall one-dimensional signal. Only a fraction of the measurements is needed, compared to the traditional sampling approach.

This approach can be simulated computationally. Figure 3-8 shows an example of a 1D signal which consists of a combination of 2 sine waves with different frequencies (111 Hz and 250 Hz). The dots in the figure show locations where the signal intensity was sampled, which is equivalent to only 10% of the points that would have to be sampled by following the Shannon-Nyquist theory. Using the intensity values at these points in time and the timings when the signal was sampled, a compressed sensing reconstruction can accurately acquire the underlying signal. This effectively gives the ability to acquire the compressed measurement directly without having to acquire a dense amount of data first and then compressing it.

When applying this measurement regime experimentally, the big caveats are that the timing must be known very precisely. Any uncertainty in the timing of the measurements will lead to a poorer reconstruction of the overall signal. Additionally, the reconstruction of the signal takes some computing time which might make this approach impractical for some applications. This principle has been utilised to boost the sampling rate of oscilloscopes [75].

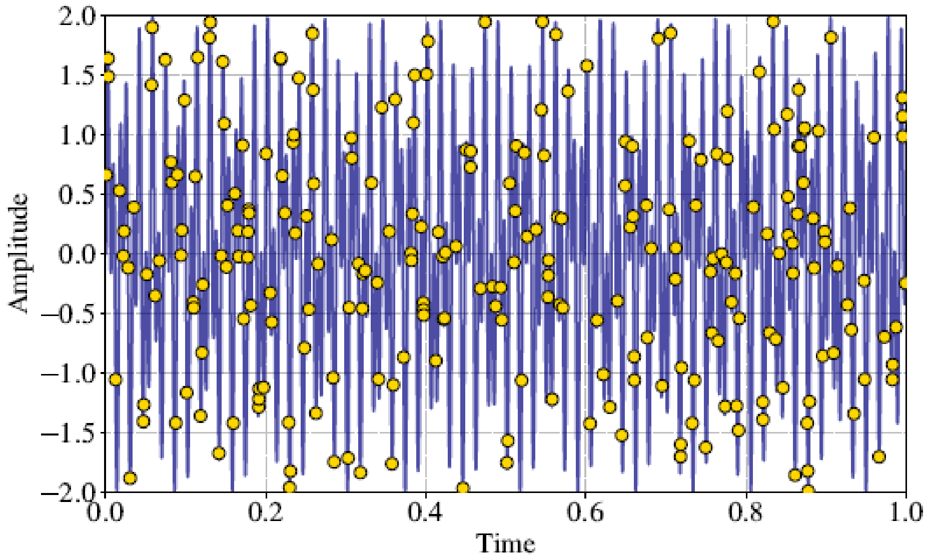

Figure 3-8 An example of arbitrary 1D signal consisting of 2 frequencies (111 Hz and 250 Hz) with yellow dots indicating random sampling points. Using compressed sensing theory, the original signal can be accurately reconstructed with the number of points sampled. In a traditional sampling regime, the sampling rate would have to be at least twice the highest frequency.

3.4.2 Testing the model - simulating single pixel camera

To further extend the simulation model, the principles of compressed sensing were applied to demonstrate a single-pixel camera measurement. To achieve this, the sample was masked with a measurement pattern, and the sum of all pixel values within the masked areas was calculated, resulting in the total intensity of the masked area. This process was then repeated for several different masking patterns, allowing the calculation of total pixel intensity for each measurement. This approach simulated the scenario of using a simple photodiode, where a sample was masked with various patterns, and the light reflected off it was measured. In this case, the measurement consisted of a single current reading of the reflected light from the sample. By repeating the measurements with different patterns and subsequently subjecting the entire dataset to a reconstruction algorithm, the overall image could be obtained without the need for measurements of each individual point. This approach was the first experimental implementation of compressed sensing published in literature [44].

To simulate a single pixel camera, the method is split between two parts – the measurement simulation and the reconstruction simulation. The first part of effectively simulating a measurement is to mask the virtual sample with a pattern. To effectively do this, a simple `for` loop was used, repeating for the number of pixels in the image. For every iteration of the loop, a pattern generation function called `wht_pattern_new` gets called, as shown in Figure 3-9. This function takes the measurement index (`i`), Hadamard order number (`m`) and a alternative Hadamard basis array (`v`) as inputs and generates a Hadamard pattern of dimensions $2^m \times 2^m$, which consists of `True/False` values. NumPy's advanced indexing syntax allows masking the virtual sample in a straight-forward way by using the Hadamard pattern as an index of the virtual sample to return a masked image only containing image values where the pattern had `True` values. In this case, the measurement simulation is straightforward – for every masked array, all the pixel values are simply summed up. The `for` loop is then repeated, storing the pixel sums.

```
measurements = np.empty(pixels, dtype=int)
for i in range(pixels):
    #get hadamard pattern
    had_pattern = wht_pattern_new(i, m, v)
    measurement = np.sum(image[had_pattern])
    measurements[i] = measurement
    if i % 10 == 0: print(i)
```

Figure 3-9 The for loop used to simulate a single-pixel camera type of measurement. A function is used to generate a pattern based on the iteration of the loop. The pattern then masks the virtual sample and returns a sum of all the pixel values covered by the pattern.

Therefore, the measurement part of the methodology results in a 1D array of pixel sums of different masks. The index of the array corresponds to the index of the masking pattern used. This structure is displayed in Table 3-1.

Table 3-1 An example of structure and value seen during compressed sensing measurements. A few Hadamard patterns are shown here with their respective indices. The white parts of the patterns are where the sample is measured. The masked image is added to better indicate the parts of the image that are being measured with each sample. The final row is the measured values from the given pattern. The number of patterns used goes up to the number of pixels in the sample image.

Pattern index	3	10	12	36	92
Masking Pattern	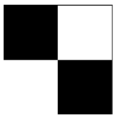		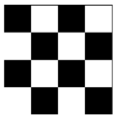	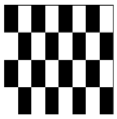	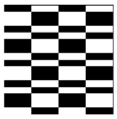
Masked Image			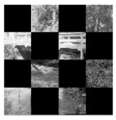	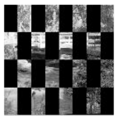	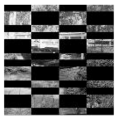
Measured value	15255036	14993527	14281186	14838557	151974630

The 2nd part of the simulation process was to reconstruct the compressed measurements acquired in the first part. Before performing the reconstruction, the patterns and measurement data need to be pre-processed. For the reconstruction to work, we must ensure minimum coherence between the measurement patterns used and the sampled images. However, as described in the compressed sensing review chapter, we can decrease the coherence by applying a transform. In this work, we used Haar wavelet transform to achieve this, by applying it to the measurement patterns. Finally, the transformed patterns and the measurements, as well as sampling level can be input into the reconstruction algorithm to run the optimisation and find the sparsest solution, which is implied to be the sampled image. Note that the answer provided by the algorithm is in the transform domain that was applied to the measurement patterns. An inverse transform should be applied to display the answer in a natural domain.

This reconstruction is displayed in Figure 3-10, where the sampling level was set to 25% and a good image reconstruction was still observed. A good quality reconstruction is observed, with $SSIM = 0.89$. Therefore, it can be concluded that all parts and functions of this simulation model is behaving as expected and applying the compressed sensing technique correctly. We can then build onto this algorithm to develop a more complex simulation, which is covered in the next section.

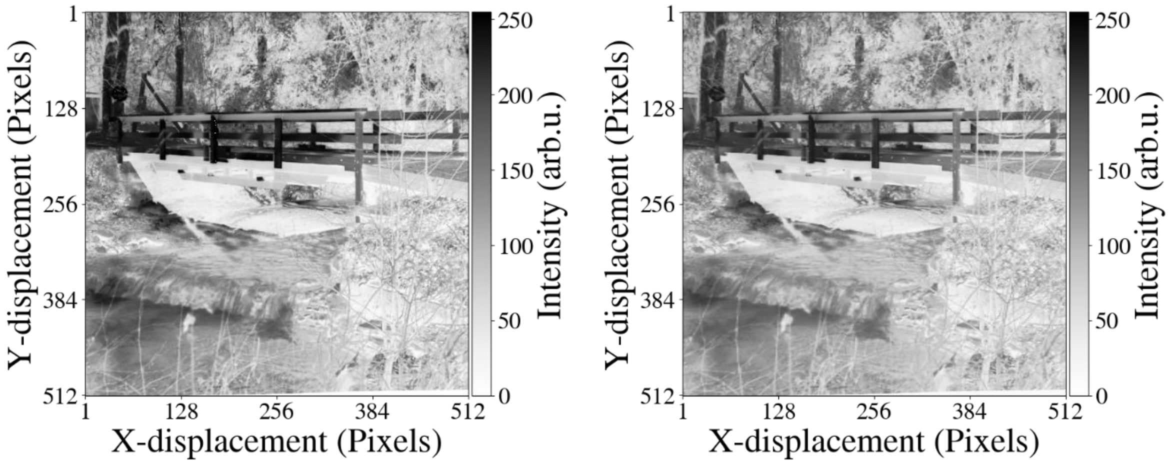

Figure 3-10 The image on the left is the ‘ground truth’ image that used as the source for the single-pixel camera sampling methodology described above. The image on the right is reconstructed from the sums of the measured patterns. A total of 65,536 patterns were measured, equivalent to a sampling level of 25%, for an image of $512 \times 512\ px$.

3.4.3 Spectral measurements from masked sample

Another use case for compressed sensing that was considered in this work is towards spectral imaging with compressed sensing. From a numerical simulation perspective, the key difference between these measurements is that every pixel of the image can no longer be described by a single value. Instead, every pixel consists of a spectrum, adding an additional dimension which has to be considered.

The masking function used in the previous case can be reused here. However, the spectral data cube must be sliced along its spectral axis first, to reduce the cube to a series of 2D images. Every image then has the masking function applied to it, returning a PL intensity masked image at each wavelength bin. This is illustrated in Figure 3-11.

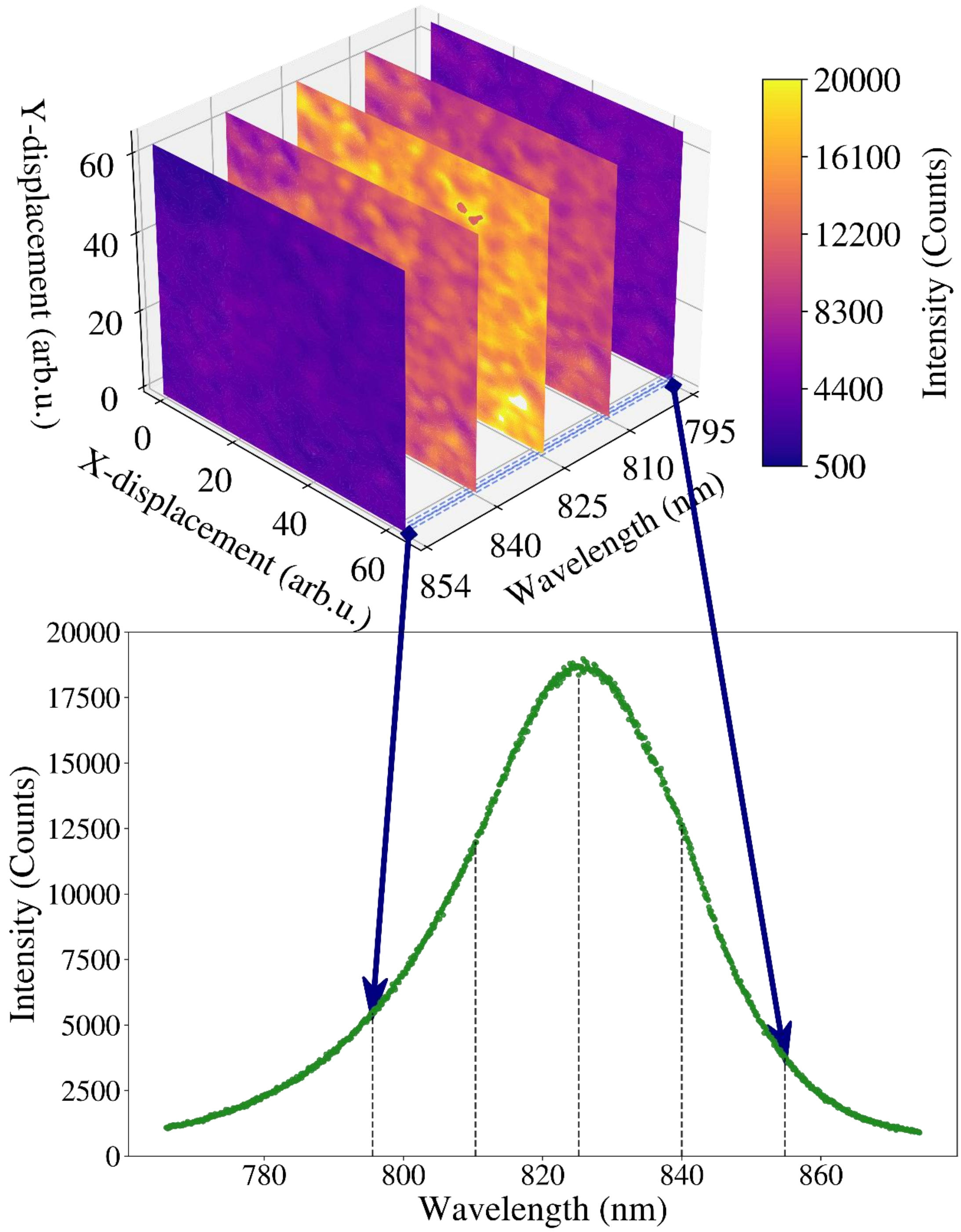

Figure 3-11 An illustration of the structure of hyperspectral imaging. In this case, every spatial pixel of the image consists of its own spectral response, resulting in a 3D data cube structure. To make this type of structure compatible with compressed sensing algorithms, the cube can be split into a series of images for each different wavelength.

To simulate the measurement part, a key assumption was made. We assume that the contributions from different parts of the masked sample combine in a linear way. In other words, if 2 points of the sample were to be excited at the same time, the measured spectrum would be a combination of the 2 points. Based on this assumption, the measurement simulation becomes similar as in the previous case. All the values from the masked area can be added up. This is then repeated at every wavelength bin, resulting in a 2D measurement matrix. Row index of the matrix corresponds to measurement pattern used and the column index is the wavelength bin measured.

To carry out the simulations, hyperspectral imaging of CdTe sample was performed using Horiba Labram HR microscope. The acquired measurements were then used as the virtual samples for the compressed sensing simulations.

At the time of performing these measurements, the reconstruction algorithms were incapable of handling a 2D measurement. Instead, the reconstruction was performed on each wavelength bin at a time, treating it independently of all other bins. An inverse transform was applied to each of the slices, to construct final data cube.

For displaying the data, it was useful to perform some fitting to reduce the data cube into a 2D image. In this case, peak wavelength was determined at each pixel to construct a peak wavelength map from the data cube. The original and reconstructed ones are shown in Figure 3-12, with a few points on the right showing the spectra that they consisted of. Note that this assumes an 'ideal' sampling condition, where the true spectra can be losslessly captured by the simulated detection, with no addition of noise. Some noise considerations were investigated further on in the chapter.

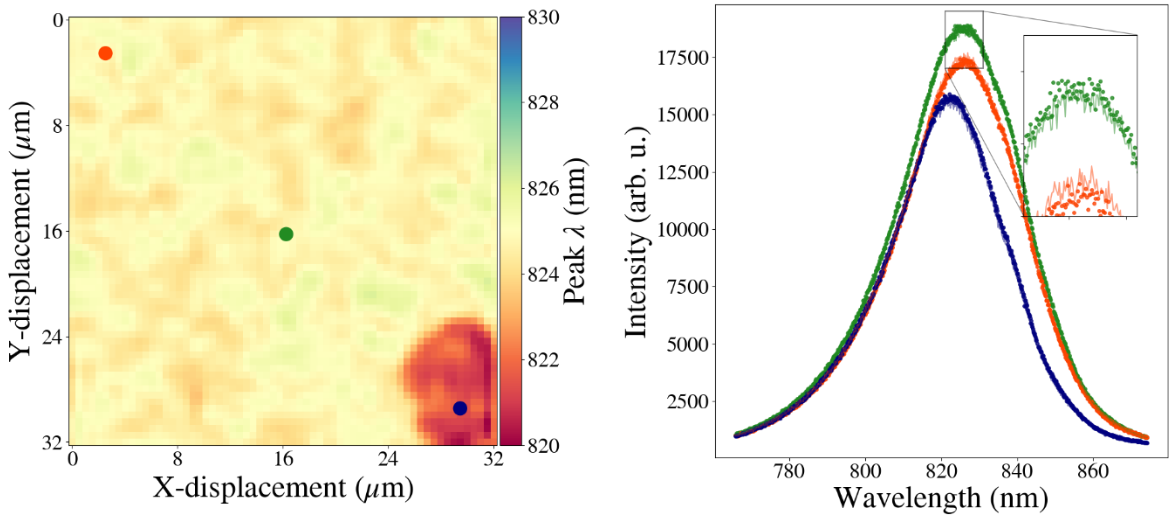

Figure 3-12 A reconstruction of the peak wavelength map for CdTe from sampling the hyperspectral data cube using the described methodology. A few points on the map are highlighted and their respective spectra are shown on the right. The solid spectrum lines are the original spectra of those points, and the scatter plots are the spectra of those same points after reconstruction.

3.4.4 TCSPC measurements from masked sample

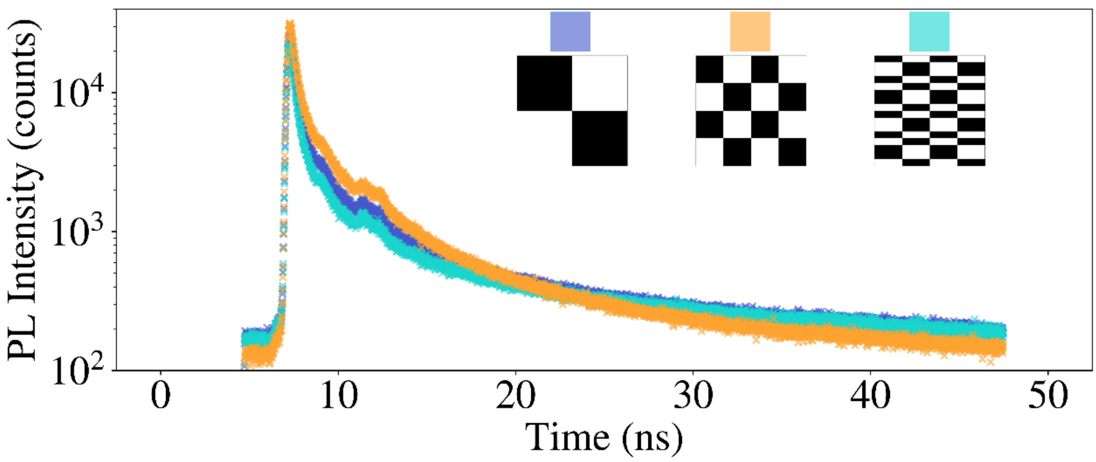

Figure 3-13 Example of a typical CS measurement. The inset patterns demonstrate some of the patterns used in the measurements to mask the sample area. Only the white parts of the pattern were allowed to excite the sample. The coloured decays show the TRPL measured for each of these patterns.

One of the main goals of this research project was to apply a similar principle towards TCSPC measurements. This presented an extra layer of complexity onto the simulation technique, as not only the compressed sensing part had to be simulated, but also the TCSPC measurement. The developments of numerical TCSPC simulation were described in previous sections. Therefore, the techniques developed for single pixel camera and spectral measurement simulations must be incorporated with the TCSPC measurement simulation.

Another function called `give_pattern` detailed in Figure 3-14, was used to mask the virtual sample, parallelise the `for` loop and process the measurements into a histogram. The matrix `A` contains all the patterns to be used in the measurements and the `for` loop is set to iterate and perform TCSPC measurement after masking the lifetime map with each of the patterns. Because every pattern is measured independently of each other, the `for` loop could be parallelised, improving the simulation running time.

```
def give_pattern(A, bins_total, cells, pulses, prob, tau, delta,
longtime, bin_range):
    """
    Function for performing measurements on multiple patterns in
parallel.
    """
    start, stop = bin_range
    result = np.empty((int(cells*delta), bins_total))
    for i in prange(int(cells*delta)):
        print("Pattern ", i)
        pattern = np.where(A[i])[0]  #returns a list of indices where A
== True
        times = TCSPC(pulses, pattern, prob, tau, longtime)
        bin_heights, _ = np.histogram(times, bins=bins_total,
range=(start, stop)) #converts times from each pattern to hist
        bindata = np.asarray(bin_heights)
        result[i, :] = bindata
    return result
```

Figure 3-14 Function used to virtually mask a sample with a given pattern. Variable A contains all the patterns to be measured. The function TCSPC carries out the TCSPC simulation, considering only the areas where masking pattern contained True values. The innerworkings of TCSPC function are described in a figure further on. The TCSPC function output is then processed as a histogram and results are saved.

However, due to TCSPC, we know that only a single detection event can occur in a measurement cycle. Therefore, we need an additional step to determine which pixel causes the emission photon. To effectively simulate this, another key assumption had to be made. We assumed that all of the pixels illuminating the virtual sample have an equal probability of emitting a photon. Therefore, after the masking, a random pixel is chosen to test for emission and TCSPC considerations. The virtual sample map consists of lifetime values, which are used to determine the photon arrival time. To determine the arrival time, a random number is drawn from an exponential distribution with the decay constant set to the lifetime of value of the chosen pixel. This process is similar to the one described in Figure 3-3. However, only the fastest arrival time gets recorded. The function used to do this is shown below in Figure 3-15.

```
def TCSPC(pulses, cell, prob, tau, longtime):
    """
    Records the fastest arriving photon from each pulse. Allows the possibility
of multiple PL photons being emitted
    on each pulse, however, only fastest one gets recorded. Assumes uniform
illumination density and uniform probability
    of PL emission. Assumes exponential decay of lifetime.
    """
    arrivals = []

    for idx in prange(0, pulses):
        shortest = longtime
        pl_prob = np.random.random() #draws a number between 0 and 1 from
continuous uniform distribution
        i=0
        if len(cell) == 0:
            shortest=0
        else:
            while pl_prob<prob:
                #this part executes whenever a pulse produces a photon
                idx = np.random.choice(cell, size=1)[0] #chooses which cell of
the sample emitted photon based on discreet uniform distribution
                pltime = np.random.exponential(tau[idx]) #Assigns the arrival
time of photon to detector. Drawn from exponential distribution
                pl_prob=np.random.random() #checks if another photon is
emitted. Can result in almost infinite loop as prob approaches 1
                if pltime<longtime and pltime<shortest:
                    #for handling a case were >1 PL photons emerge from given
laser pulse. Only the time of fastest one is saved
                    shortest = pltime
                i=i+1
        if shortest != longtime:
            #to only save values from pulses which result in emission
            arrivals.append(shortest)
    return np.asarray(arrivals)
```

Figure 3-15 The function written to simulate TCSPC with compressed sensing. At the start of each laser pulse cycle, a random pixel gets selected for emission. That pixel's value is then used to emit a photon and record its time. The cycle repeats for the number specified by pulses variable. The function outputs the arrival times for every laser pulse that caused an emission.

The cycle gets repeated for a predetermined number of simulated laser pulses, before moving onto the next projection pattern. Once all the laser pulses of a given pattern have been measured, all the arrival times are processed as a histogram. The counts for each bin are saved and the algorithm moves onto the next pattern and the same cycle of laser pulses is repeated. The measurement is finished once all the patterns have been measured. The final result file is a matrix, where each row index is the index of the mask that was used, and each column is the temporal bin used. All the values within the matrix are the number of counts of photon detections. Note that no spatial information gets saved – the measurement file does not contain information about which pixels resulted in the photons being emitted.

The challenge here arises from the fact that we cannot consider every point of the sample to be defined by a single value. Instead, every pixel has its own distinct temporal signal. If a sample is excited using one of the masking patterns the measurement consists of a decay which is a contribution of all the recombination events across the whole masked area. Every measurement pattern will excite different combinations of the sample areas and, therefore, will create a slightly different overall temporal response. This is illustrated in Figure 3-13 where the inset patterns show examples of some of the measurement patterns used in this work and the TRPL signal for each of these patterns. This highlights the novelty of this work since previous implementations of compressed sensing considered measurements that could be defined by a single value, whereas in the case of TRPL every measurement is a decay. Therefore, a suitable reconstruction routine had to be determined through simulations before performing the physical experimental work.

3.4.5 Compressed sensing TRPL reconstructions

One of the initial ideas for reconstructing compressed sensing data was to fit each of the decays and determine their decay constants. Then every pattern results in a single value which can be used as inputs into the reconstruction algorithm. However, after initially attempting this the reconstructed images in simulations lost all their structure and a uniform image was acquired. The reconstruction seemed to resemble the overall average TRPL response of the entire sample area. This was partly expected based on the linearity measurements shown in Figure 3-7, where it was shown that shorter lifetimes have higher contribution to the decay constant measured.

Instead, it was decided to perform the reconstruction by slicing the TRPL data into bins, similarly to how it was described for spectral simulation in section 3.4.3 . This way, each reconstruction consisted of the PL intensity map at each time slice. A reconstruction could then be repeated for every measurement bin to acquire the measured data cube. This data cube consists of two spatial dimensions and one temporal, i.e., each pixel has a corresponding TRPL reconstructed for it. The resulting data cube is demonstrated in Figure 3-16.

The data cube can be further analysed by fitting a function through the temporal axis to determine its decay constant and display the charge carrier lifetime maps. This was the final step in building an effective simulation model which was then suitable for further testing and tuning of the simulation parameters. The results are presented and discussed in the sections below.

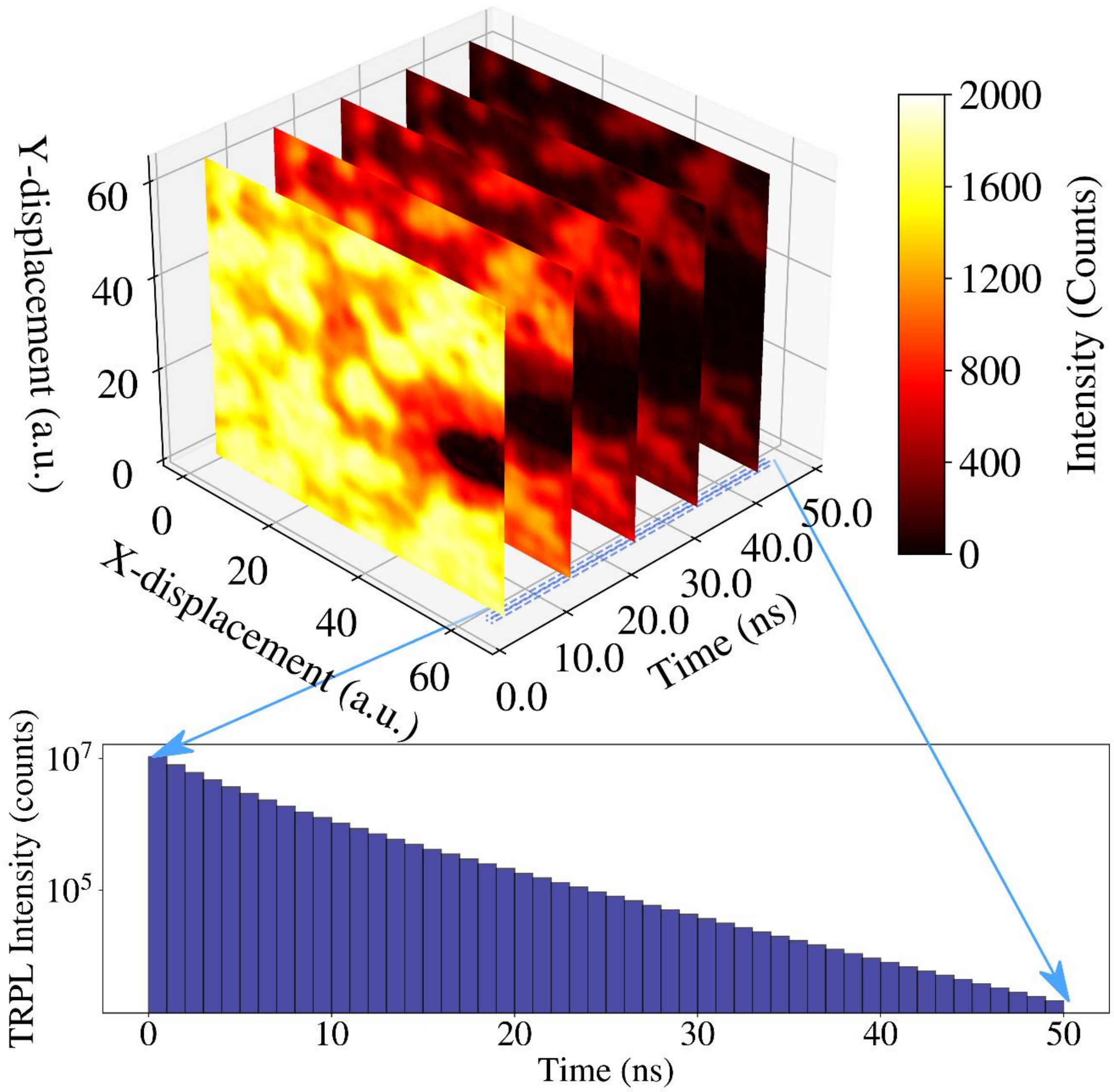

Figure 3-16 Data cube example of PL intensity images at varying time bins as reconstructed using the SPGL1 algorithm. Every spatial pixel of the data cube contains an estimated TRPL response of the pixel.

3.5 Simulation results

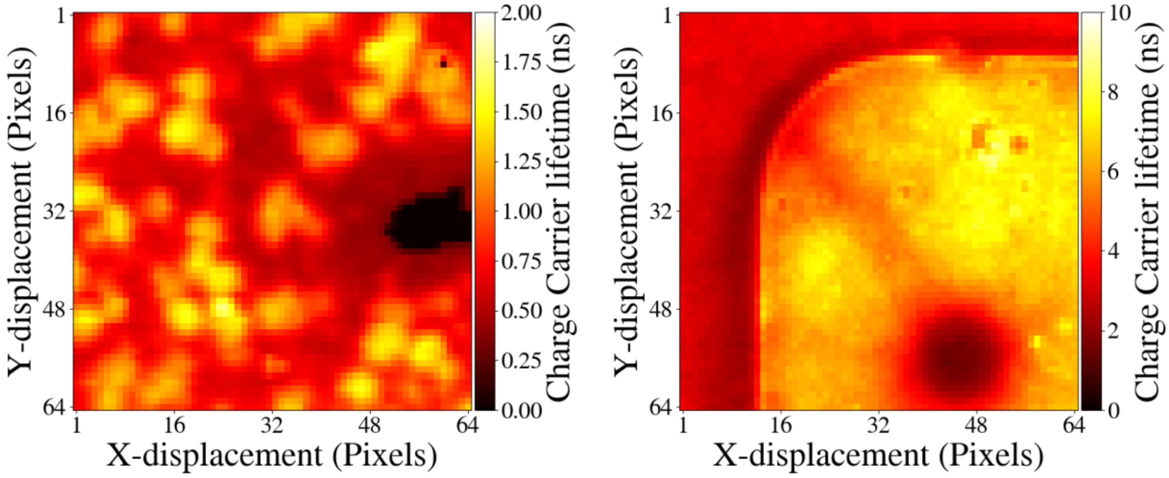

Figure 3-17 The reference images that were used as the source or 'ground truth' images for carrying out the simulation work. The left image was taken from a CIGS PV device measurement and the right image is of a perovskite PV device.

The images shown in Figure 3-17 were used as the 'ground truth' images for the purposes of simulation. The image on the left was experimentally acquired by raster mapping a CIGS PV device with TRPL measurements and then fitting the decays. The right image was acquired using photocurrent mapping of a perovskite PV device. It is useful to note here that the exact images do not have a major influence on the overall process of the simulation. The same principles could have been applied by using any 'natural' image.

The image values were considered to be the charge carrier lifetimes for the measurement simulation. When a given image pixel gets sampled, a number is randomly drawn from exponential distribution with the decay constant set to the value of the pixel. After carrying out the measurement and reconstruction processes, the acquired data-cube gets fitted with an exponential decay constant to acquire the reconstructed lifetime values. This allows for comparison between the true and reconstructed images.

3.5.1 Scanning the parameter space

The first consideration was investigating the reconstruction sampling level. As detailed in the compressed sensing theory section, the use of compressed sensing allows a reduction in the number of measurements required to reconstruct signals, overcoming the sampling typically needed as according to Shannon-Nyquist theorems. In this work, a sampling level denoted using Δ means the percentage of patterns measured as a function of total pixels in an image. For example, a $64 \times 64\ px$ has a total of 4096 pixels. $\Delta = 10\%$ means a total of 409 patterns were measured and used to reconstruct the image.

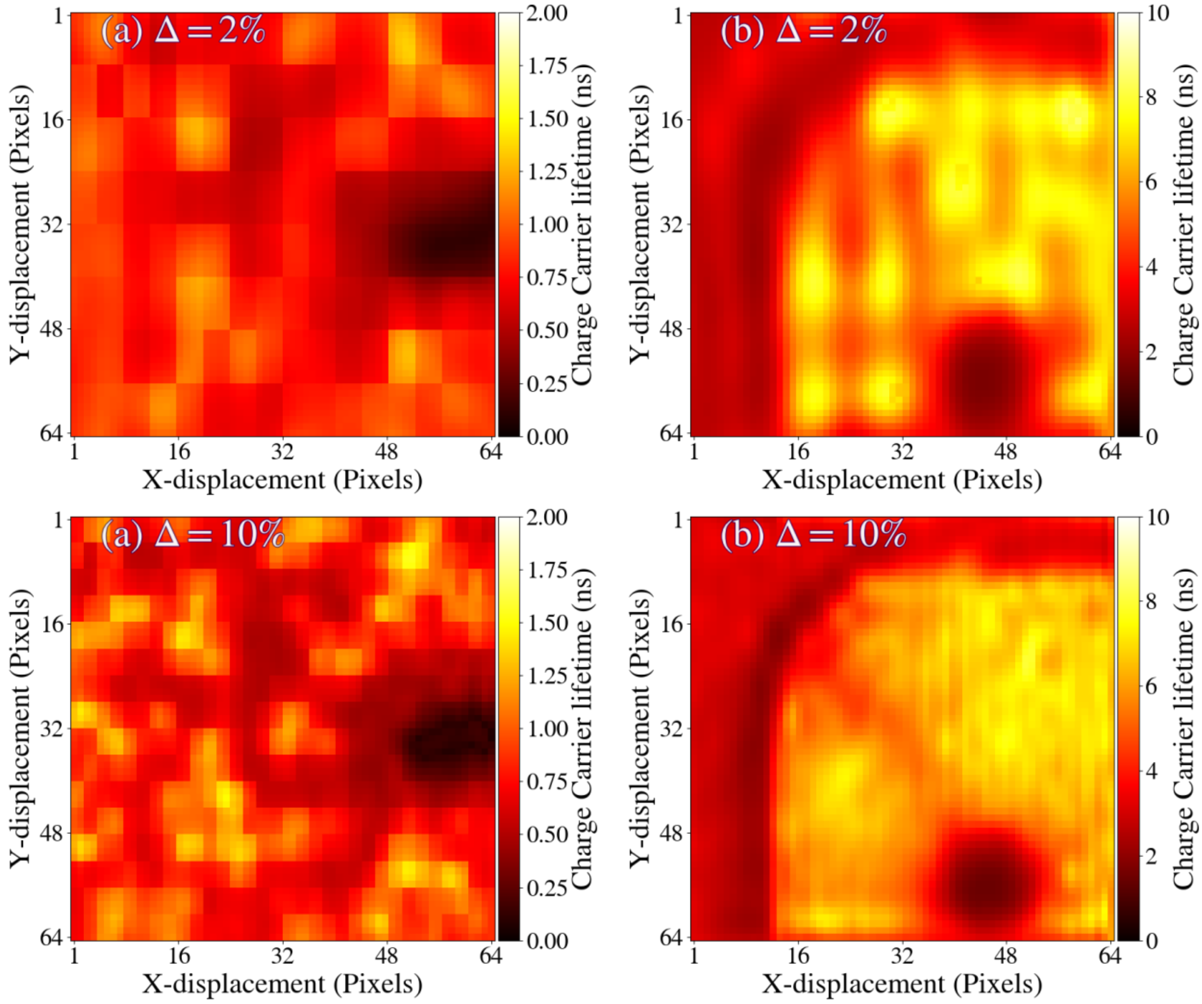

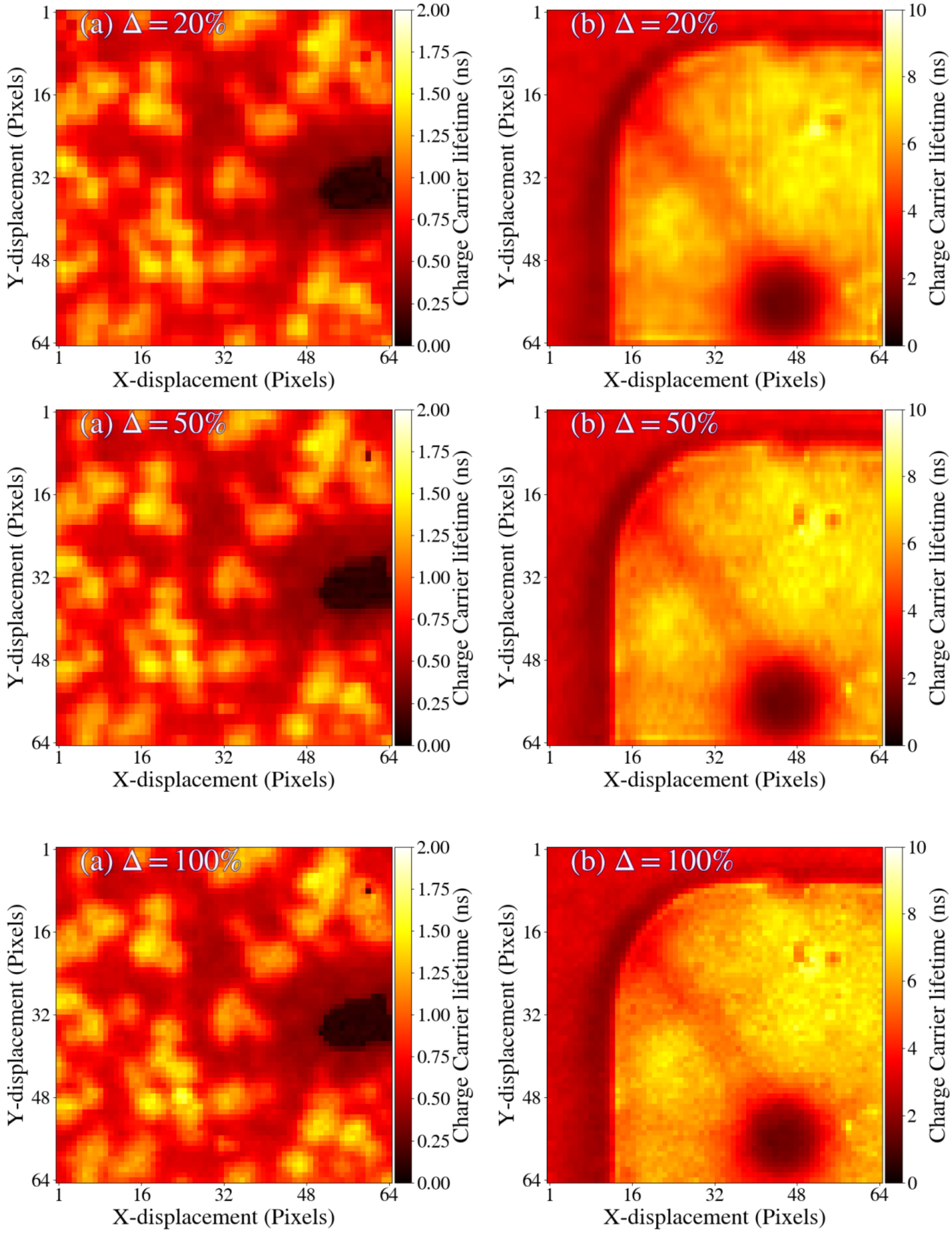

Figure 3-18 Reconstructed carrier lifetime maps from measuring virtual samples in the described computational model. The images in the left column contain reconstruction for CIGS sample and the images in the right column contain reconstructions for perovskite device. The sampling levels used in the reconstruction are denoted on the images. As the sampling level is increased, finer details get revealed.

The reconstructed images are shown in Figure 3-18 at sampling levels varying from $2\% - 100\%$. As expected, increasing the sampling level results in better reconstruction quality. However, the benefits of increased rate get smaller, at higher rates. The major structure of the samples gets accurately identified even at very low sampling levels of 2% and 10%. One possible application for very low sampling level measurements could be accurately identifying areas with higher defect areas within a broader area, such as a wafer. A low sampling level could be used to image the whole wafer in very short amount of time. If any areas show a significant difference in quality, these could then be focused on and measured in more detail.

To better understand the effect of the different sampling level, structural similarity index measure (SSIM) [76] was used to quantify the comparison between the ground truth image and the reconstructed ones. The SSIM ranged from 0.4 at the low sampling level of 2 %, to 0.98 at the high end, where SSIM = 1 would mean an identical image. The results are shown in Figure 3-19 for both samples. It is evident that increasing the sampling level past 25% for both samples offers very minimal improvements in reconstruction quality according to the metric.

It is also important to note that the maximum quality of reconstruction achieved differs between the two samples, with the perovskite sample reaching a higher maximum SSIM value compared to the CIGS sample. This difference may arise from the distinct ranges of charge carrier lifetimes across the two samples. CIGS sample exhibited lifetimes spanning $0 - 10\ ns$ whereas for the perovskite sample, lifetimes varied from $0 - 2\ ns$. The broader distribution of carrier lifetimes might be more challenging for the compressive sensing algorithm to resolve accurately. This is supported by the simulation work shown in section 3.3.3, where the presence of two distinct lifetime regions resulted in an overall measured lifetime being biased towards the shorter lifetime.

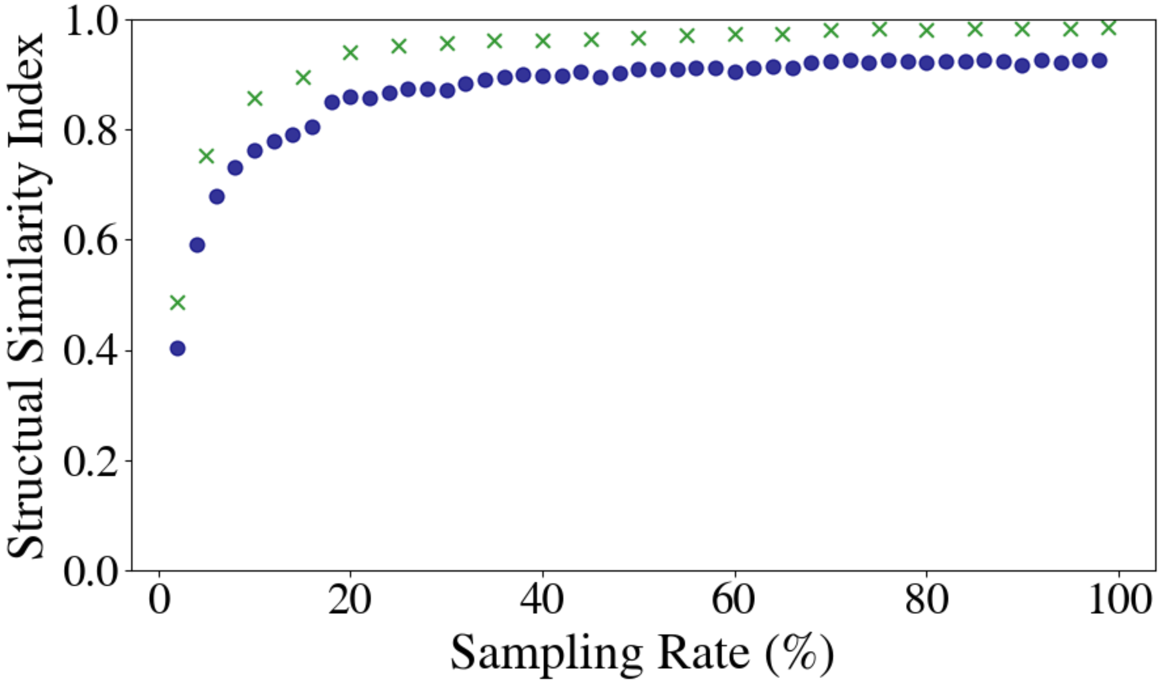

Figure 3-19 SSIM figure used to compare the similarity between the reconstructed images and the virtual samples. The green crosses refer to the CIGS sample and the blue circles refer to perovskite sample. The results indicate a rapid improvement in quality until about 20% sampling level, after which the improvement becomes minimal.

3.5.2 Noise

The results shown in previous sections assumed idealised measurements. They do not contain any sort of measurement noise or background contributions, which would be present in a real experimental system. In a physical measurement, there would be variations introduced by random measurement noise, the dark counts of the detector, resolution and dynamic range of the instruments, laser instabilities and other sources. Adding the sources of noise to the simulations helps to further evaluate the methodology as well as quantify some of the limitations that might be expected when developing the physical system.

To simulate the noise, the measurements that were already acquired were perturbed using small random values drawn from Gaussian distribution. A Gaussian distribution for noise was adopted, assuming that even though each of the different sources of noise that might be present in a measurement might have different distributions, the combined effect of all the noise sources would result in a normal distribution. The normal distribution is described by the following probability density function:

$$p(x) = \frac{1}{\sqrt{2\pi\sigma^2}} e^{-\frac{(x-\mu)^2}{2\sigma^2}} \tag{3.4}$$

Where μ is the mean and σ is the standard deviation. A parameter called `noise_level` was introduced to allow a varying degree of perturbations. A single number was randomly drawn from this distribution for each bin of the measured TRPL signals, using $\mu = 0$ and $\sigma =$ `noise_level` $\times$ `bin_counts`. For example, if a noise level of 1% was specified and the bin had 1000 counts, $\sigma = 0.01 \times 1000 = 10$ will be used to draw a single number, which will then be added onto the bin counts. The noise levels considered ranged between $0.1\% - 5\%$. After perturbing the measurements, they were all reconstructed using the same reconstruction process and algorithm described earlier with the sampling level set to 50%.

Figure 3-20 shows the noisy maps reconstructed. The quality of the images appears to rapidly deteriorate with increasing noise levels. At 5%, the images have little resemblance left to the original ones. The fitting of the TRPL becomes difficult as well, with many pixels failing the fit. These simulations are important when applying the technique experimentally. These results indicate that in order for the compressed sensing TRPL system to produce reliable results, the sources of random noise must be minimised as much as possible. Additionally, the compressed sensing part of the methodology is highly susceptible to any signal changes over time, such as drift. The nature of the reconstruction algorithm considers all the differences between each measurement to be entirely related to the spatial variations of the measurement patterns used.

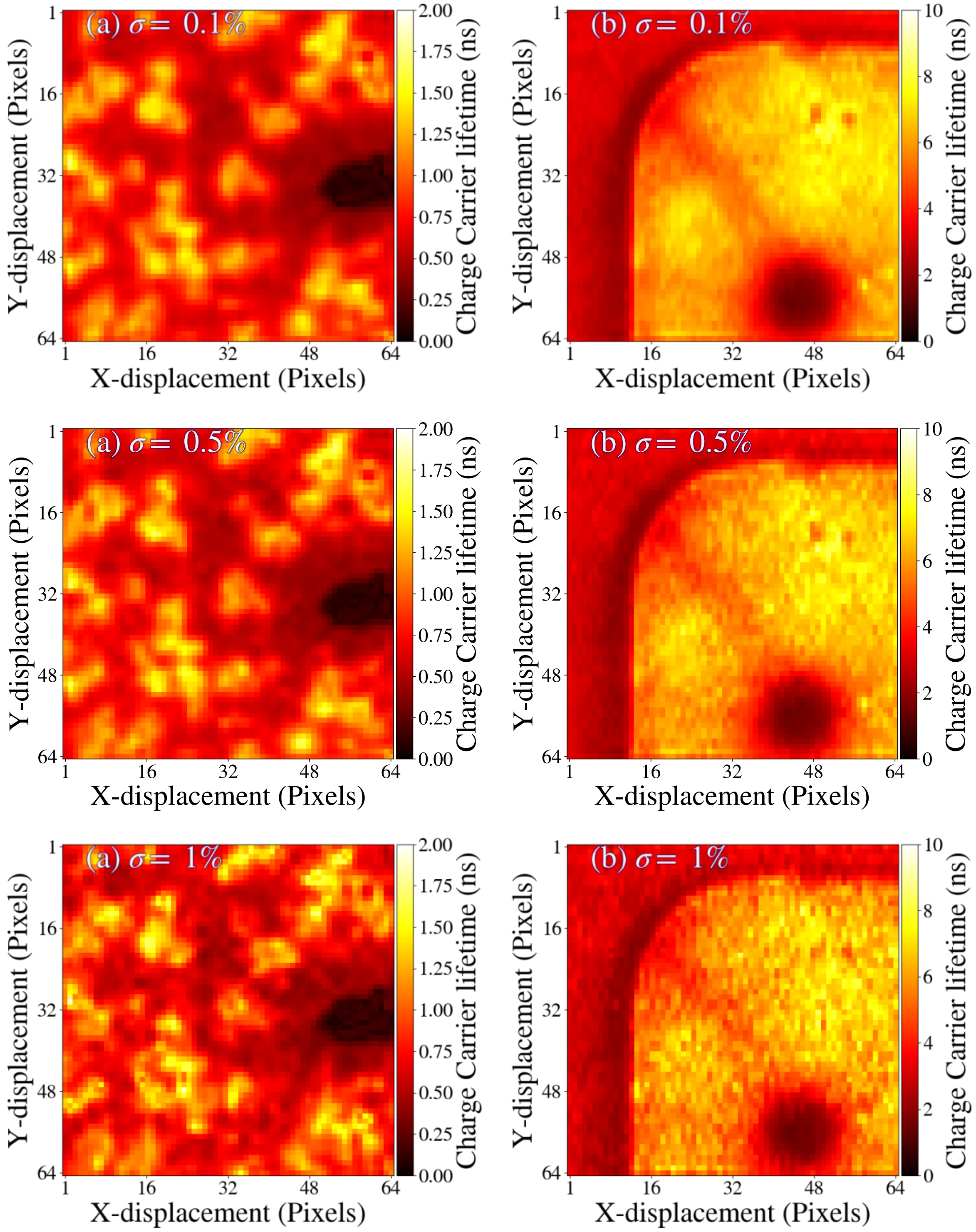
(a) $\sigma =$ 0.1%
(b) $\sigma =$ 0.1%
(a) $\sigma =$ 0.5%
(b) $\sigma =$ 0.5%
(a) $\sigma =$ 1%
(b) $\sigma =$ 1%
Y-displacement (Pixels)
X-displacement (Pixels)
Charge Carrier lifetime (ns)
1
16
32
48
64
0.00
0.25
0.50
0.75
1.00
1.25
1.50
1.75
2.00
0
2
4
6
8
10

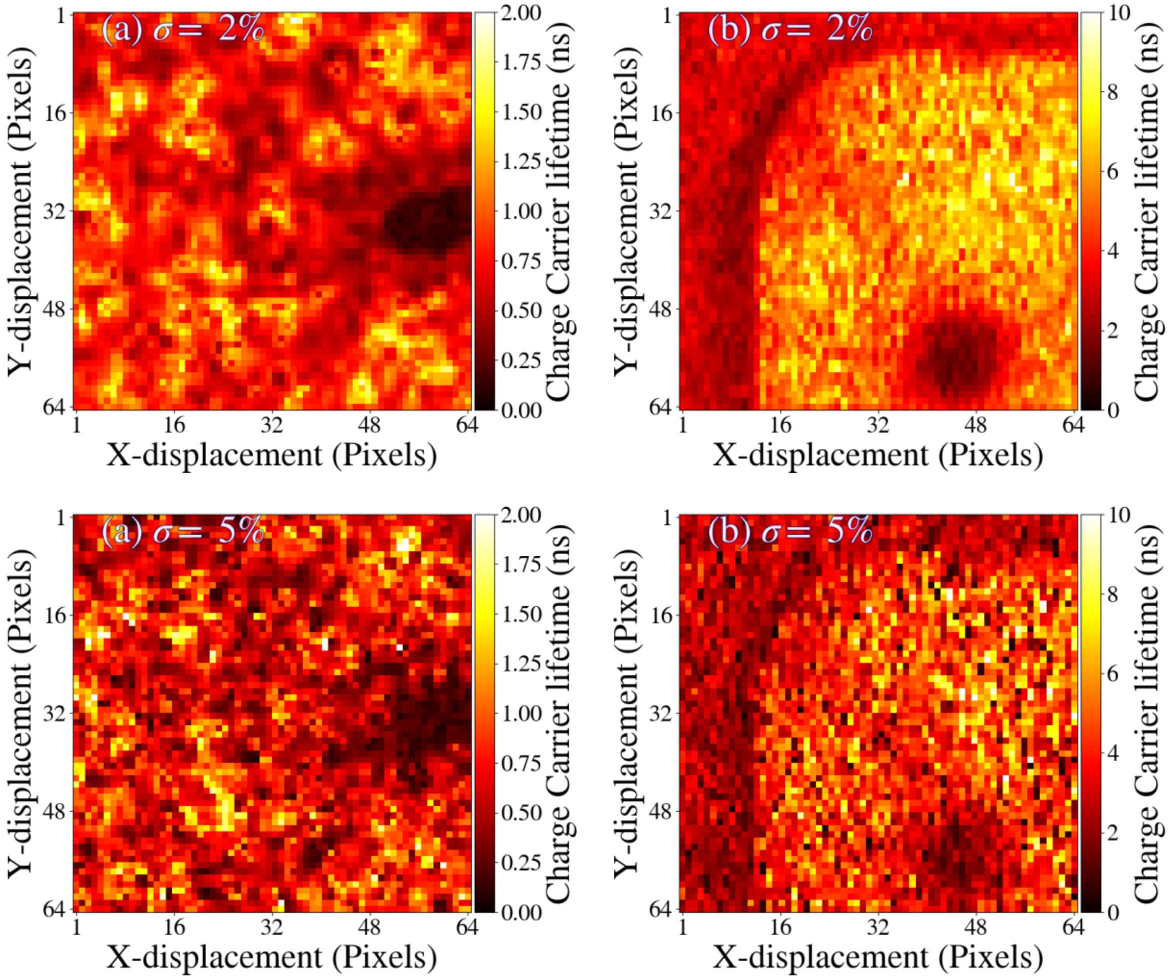

Figure 3-20 Carrier lifetime maps reconstructed using the described CS TRPL measurement acquisition and reconstruction with Gaussian noise added to each measured bin. The sampling level was kept constant at 50% for all the noisy reconstructions.

3.6 Chapter conclusions

In this chapter, a comprehensive simulation framework for compressed sensing TRPL imaging was developed and validated, forming the foundations for the experimental work presented in Chapter 5. A statistical model capable of simulating TRPL data acquisition using TCSPC was implemented. A reconstruction approach for reconstructing compressed sensing TRPL data has been developed, utilising the SPGL1 algorithm. The developed simulation, combined with the reconstruction technique, show effective reconstruction of charge carrier lifetime images, even at significantly reduced sampling rates. Testing the sampling rates demonstrated that accurate charge carrier lifetimes could be reliable reconstructed using only 20% of the measurements required compared to conventional raster scanning. This highlights the potential efficiency gains achievable with compressed sensing in TRPL imaging.

Before starting with simulation work, background information about TRPL and TCSPC was detailed. TCSPC measurements were simulated in section 3.3 using random probabilities of a number being drawn from exponential distribution. As TCSPC is susceptible to photon-pile up effects, a detailed description is given of considerations made to allow for multiple photons being emitted in a single laser pulse. Testing results are shown for the effects of photon pile-up as well as varying the composition of the measured area. The photon pile-up study demonstrated the shortening of measured carrier lifetimes at higher photon detection rates.

In section 3.4, the development of the compressed sensing simulation progressed from a simple 1D model to more complex multi-dimensional simulations. This iterative approach began by examining a 1D signal for basic compressed sensing feasibility and then expanded to simulate a 2D single-pixel camera setup, followed by a 3D model representing spectral compressed sensing which would be equivalent of hyperspectral camera measurements. The final version of the simulation included simulating compressed sensing TRPL acquisition using TCSPC measurement.

In section 3.5 the developed simulation model was utilised for investigating the effects of sampling rate. Maps of CIGS and perovskite PV devices were used as ‘ground truth’ images for carrying out the simulations. These were then investigated by performing the reconstructions at varying sampling levels, ranging from 2% to 100%. The quality of reconstructions is quantified using SSIM, showing minimal additional gain in image quality past sampling level of around 25%. It was also observed that some of the larger details could become apparent even at sampling rates of a few percent. This could be utilised for very fast, initial measurements for identifying regions of interest for further investigations.

To further improve the model, different degrees of normal noise was added to the measurements to test the robustness of the methodology. From the noise investigations, it is apparent that the methodology is highly susceptible to the effects of random measurement noise. By adding random noise with amplitude equivalent to up to 5% of the signal, the reconstructed carrier lifetime maps were greatly disturbed.

Overall, the simulation framework developed here served as a feasibility study, validating the potential of compressed sensing TRPL and establishing the reconstruction methodology required for experimental application. These findings lay the groundwork for the experimental work discussed in later chapters and underscore the value of compressed sensing for efficient TRPL imaging. The simulation approach could also be extended to test the methodology further, by considering the effects of different materials or further effects of measurement noise.

Chapter 4 Development of Time-Resolved Photoluminescence Imaging System

This chapter describes the system design, implementation and testing process of the time-resolved photoluminescence (TRPL) imaging system developed in this work, covering each of the system elements in detail. The devices investigated in the project are described. Finally, initial results acquired from various samples are presented and the issues encountered along the way and optimisation steps are detailed.

The aim of this work was to design a TRPL imaging system capable of comparing spatial lifetime profiles across different materials and devices. An additional objective was to thoroughly understand the intricacies and requirements for performing time-correlated single-photon counting (TCSPC) experiments. This meant that the system needed to function not only as a standard TRPL measurement tool but also as a TRPL mapping system. The electronics required to perform these measurements deal with accurate timing of hundreds of thousands of events each second, requiring picosecond precision. By building this measurement system from the ground up, experience and understanding of such systems was gained, both regarding the optical system and hardware implementation, but also regarding the control software, which plays a significant role in such systems. Furthermore, another aim of this chapter was to use the work described here as a starting point for the final results chapter. The final chapter seeks to expand the system discussed here to include the full utilisation of the digital micromirror device, validate that the system works as expected and explore the capabilities and limitations of TRPL imaging.

4.1 System design considerations

The first step in developing a measurement system was defining the requirements for the desired functionality. Key to this, when planning the system design, were the types of materials that would be investigated. Afterall, the chosen materials would dictate the hardware considerations, such as ensuring that the laser and the detectors are of appropriate wavelengths. Additionally, different material systems will have varying charge carrier lifetimes which can range from ns to μs.

The primary focus were material systems which are suitable for photovoltaic device fabrication. This aligned well with the research focus of the group at NPL and devices that were already available within the group. Additionally, an external partner on the project was a semiconductor manufacturer IQE PLC, who were also interested in providing materials to be tested in with the proposed methodology, showing interest in wafer and vertical cavity surface emitting laser (VCSEL) characterisation.

The materials and devices investigated throughout this work are the following:

- Cadmium Telluride (CdTe) PV devices, manufactured by the research team at the Centre of Renewable Energy Systems Technologies (CREST) at Loughborough University. The devices were made by depositing CdS on a 50x50 mm substrate resulting in ~200 nm thick films and then depositing CdTe in a close-space sublimation system resulting in 4-6 μm thick films. More detailed explanation of the fabrication is published in [77]. CdTe has a direct bandgap of ~1.51 eV (~821 nm) at room temperature [78]. These devices have been extensively studied and reported on by the CREST group, allowing for comparison between measurements done using different systems. The TRPL measurements done by the group show lifetime values of $\tau_1 = 1.39\ ns$ and $\tau_2 = 3.91\ ns$ [79].
- Copper Indium Gallium Selenide (CIGS) solar cells fabricated at Loughborough University. The absorber layer thickness was ~3 μm, composing of $Cu_{0.9}In_{0.7}Ga_{0.3}Se_2$. The detailed description of the fabrication process is given in in [80,81]. This material system is useful for production of PV devices due to its advantageous temperature dependency and low-cost manufacturing techniques [82]. CIGS has a widely tuneable bandgap, ranging from 1.01 eV up to 1.68 eV [83] by varying the Ga fraction. Some TRPL results of these devices have also been published, showing lifetime value of $\tau = 2.45\ ns$ at 1055 nm emission wavelength [58].
- Selection of GaAs wafers and devices. Pieces of undoped and Si p-doped GaAs wafers were used for investigation described in this work. Additionally, a GaAs reference cell (commercial reference cell by ReRa Solutions) was also used. There is little literature on measuring charge carrier lifetimes within wafer substrates as it

is typically only considered when measuring devices. However, it was expected that these materials would exhibit high emissivity as well as high uniformity which could prove useful when testing the methodology. The bandgap of GaAs is 1.435 eV (~864 nm) at room temperature [84].

- A variety of perovskite solar cells, fabricated by groups at University of Surrey and Swansea University [85]. Perovskite materials have been receiving huge amounts of interest over the recent years and have seen their power conversion efficiency rapidly rise [86]. They are a useful material for the development of this methodology due to their high emissivity and relevant lifetime values.
- Other materials were also considered throughout the project, such as InP PV devices, which have a bandgap energy of 1.34 eV (~923 nm) [87].

4.2 Hardware considerations

This setup employs a single objective lens for both illumination and light collection, using a dichroic beam splitter to direct the PL signal toward the detector. A schematic diagram of the targeted layout is shown in Figure 4-1. The schematic shows how each of the components fit together to form the measurement system. The components required for building the measurement system are:

- Excitation source
- Photodetector
- TCSPC Electronics
- Optical Components
- Safety Measures
- (Optional) Sample Positioning system

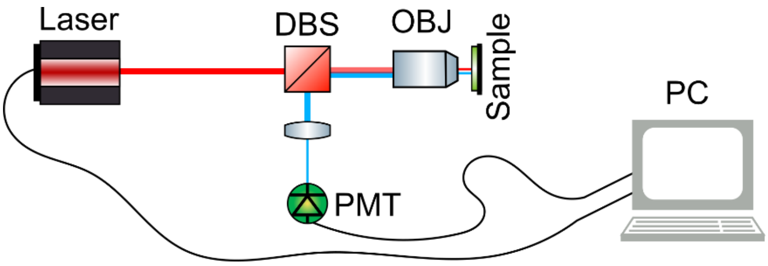

Figure 4-1 Schematic diagram of the TRPL imaging system described in this chapter

In the following sections, each component is discussed in greater depth, with an analysis of available options. The options are compared, and the rationale behind final selections is provided.

4.2.1 Laser choice

First piece of equipment considered when designing the TRPL system was the laser source. The key considerations can be listed as follows:

- The pulse duration of the laser should be at least an order of magnitude shorter than the shortest charge carrier lifetime that is expected to be measured. Therefore, pulses that are <100 ps would be best in this application. TCSPC measurements could still be resolved with longer pulses, but additional complications would be introduced due to the rise and fall times of the pulses
- The laser must be able to be pulsed with a suitable repetition rate as well as able to output the reference signal. The inverse of repetition rate dictates the maximum time window that can be measured with a TCSPC setup. However, having a low repetition rate would lead to a prohibitively long measurement duration. A repetition rate that could be varied from ~10-100 MHz would be most suited.
- The laser wavelength in a TRPL measurement system must exceed the bandgap energy of the material to excite electron-hole pairs while also achieving sufficient penetration depth. This allows photoluminescence from both the bulk and surface, enhancing insight into recombination dynamics throughout the material. The penetration depth is determined by the material's absorption coefficient, α, at the laser wavelength, with the light intensity decaying exponentially with depth *z*

according to $I(z) = I_0 e^{-\alpha z}$. High α values limit penetration, restricting excitation to the surface region.

- Finally, the laser power must be sufficiently high to create a sufficient power density at the sample plane to excite enough carriers within the material.

2 main companies with suitable laser systems were considered – Picoquant and Becker & Hickl (B&H), both having multiple suitable options. Both specialise in complete systems for TCSPC microscopy, meaning that all the key components could be sourced from a single manufacturer, simplifying the integration and ensuring compatibility.

Three lasers were considered, summarised in Table 4-1. B&H BDS-MM 635 nm and Picoquant LDH-IB 640 nm had nearly identical specifications in terms of wavelength, power, pulse width, and repetition rate, making both viable options for this application. The key difference between these models was the cost: the BDS-MM laser was offered at a significantly lower price (€6,410 versus €17,170 for the LDH-IB).

Picoquant LDH-P 530 nm provided a distinct advantage in terms of beam quality, with a superior beam shape (circular, $M^2 < 1.1$) and higher average power (>200 mW). However, its shorter wavelength (530 nm) raised concerns about reduced penetration depth. This would result in most of the excitation being confined to the sample's surface, making it challenging to measure bulk recombination dynamics effectively. The higher cost (€37,490) further reduced the feasibility of this option.

Although LDH-P offered better beam quality and a higher power level, the elliptical beams of BDS-MM and LDH-IB lasers were deemed adequate for the experimental work planned in this chapter. The laser light would be focused into a single spot making the beam shape not as important. Additionally, while parameters like beam divergence would be useful to compare, this information was unavailable for the BDS-MM upon inquiry; however, it was concluded that this absence would not significantly impact performance in this context.

Ultimately, the B&H BDS-MM 635 nm laser was selected due to its competitive pricing and specifications closely matching those of the Picoquant LDH-IB 640 nm. However, as discussed in Chapter 5, the choice of this laser introduced some limitations. The work described in that chapter involved exciting larger sample areas simultaneously, which meant that higher laser power as well as a uniform beam profile would have significantly benefited those experiments and enhanced the systems performance.

Table 4-1 Some of the key specifications of the lasers considered for this system. Costs acquired in July 2020.

	BDS-MM-640-FBE [88]	LDH-IB-640-B [89]	LDH-P-FA-530XL [90]
Supplier	B&H	Picoquant	Picoquant
Wavelength	640 nm	640 nm	530 nm
Beam shape	1 x 3 mm	1.5 x 3.5 mm	2.1 ± 0.2 mm, M^2 <1.1
Power (average)	20 mW at 80 MHz	30 mW at 100 MHz	>200 mW at 80 MHz
Repetition rate	20, 50, 80 MHz	Variable, up to 100 MHz	Variable, up to 80 MHz
Pulse width	~100 ps	<90 ps	<100 ps
Cost	€6,410	€17,170	€37,490

4.2.2 Detector choice

A highly sensitive detector is required to perform TCSPC measurements, capable of sensing a single photon. Additionally, due to the samples that were expected to be investigated, a broad wavelength range was desirable, covering at least 700-1500 nm. A single detector covering this entire range does not exist on the market so 2 detectors would be required. There are 3 main types of detectors that would be suitable for TCSPC setup:

- Photomultiplier Tube (PMT)

- Single-photon Avalanche Diode (SPAD)
- Hybrid photomultiplier tube (HPMT)

Some other types of detectors are available; however, they were not suitable for consideration due to various reasons, detailed further below.

Photomultiplier Tube (PMT)

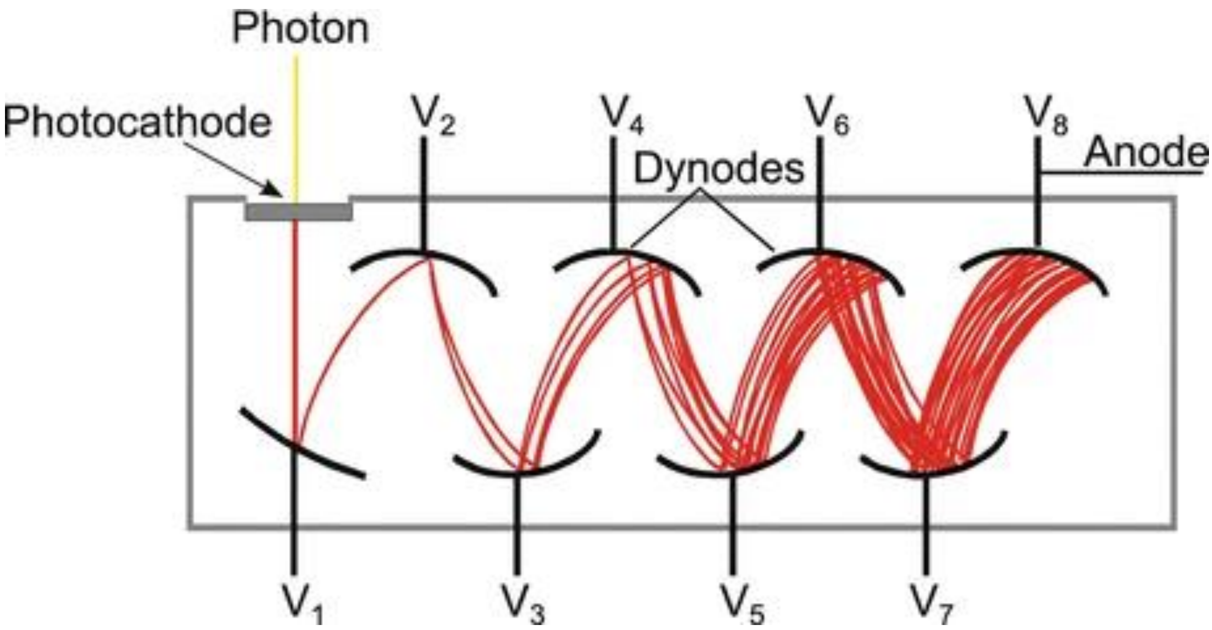

Figure 4-2 Schematic of internal components within a PMT. A photon incident on the photocathode causes an emission of an electron, accelerated towards the first Dynode, which causes additional electrons to be emitted and cascade, resulting in amplification. The final dynode is connected to an anode where a current is measured. (Source: Bülter, A. © 2014 Springer International Publishing Switzerland [91]. Reproduced with permission from Springer Nature)

Some of the earliest PMTs were first developed in the 1930s for television applications, but were later shown to be sensitive to single photons [92]. A standard PMT is a vacuum tube that converts light photons into an electrical signal. A schematic of its internal components is displayed in Figure 4-2. It consists of several key components:

- Photocathode: The photocathode is a photosensitive material located at the entrance window of the PMT. When a photon strikes the photocathode, it liberates an electron through the photoelectric effect.

- Electron Multiplier: The electron liberated from the photocathode is accelerated towards a series of dynodes, which are metal electrodes arranged in a cascade. Each dynode is held at a higher positive voltage than the previous one, resulting in electron multiplication through secondary electron emission. As the electron strikes each dynode, more electrons are emitted and accelerated towards the next dynode, resulting in an exponential amplification of the electron signal.
- Anode: The final dynode in the cascade is called the anode. It collects the multiplied electrons, resulting in a measurable electrical current. The anode is connected to external circuitry for signal processing and amplification.

The PMT operates under high voltage, typically a few hundred to a few thousand volts, to achieve electron multiplication and ensure efficient electron collection at the anode. The multiplication is caused by the secondary-electron-emission process [93], which inherently varies in the amount of electrons produced, leading to fluctuations in final signal intensity. In other words, for the same light intensity incident on the photocathode, the electrical signal collected at the anode will vary in amplitude. As a result of this fluctuation in amplitude, accurately timing the arrival of these pulses is challenging and can introduce timing jitter, as noted in Figure 4-7.

The detector efficiency is determined by the photocathode material. Commonly the photocathodes are GaAs or GaAsP for visible wavelengths and InP/InGaAsP or InP/InGaAs for infrared wavelengths. An advantage of PMTs useful for this application is their relatively large photocathode area, typically ranging 5-8 mm, allowing for easier coupling of the PL signal into the detector.

Standard PMTs exhibit an effect called afterpulsing, which can introduce artefacts in the photon-counting electronics. This refers to additional peaks that are present in the signal several ns after the main pulse. There are 2 mechanisms that are responsible for this effect. First, the electrons produced by the electrodes can elastically scatter within the tube, leading to a spread of arrival times. The second cause is due to residual gasses within the tube being ionised, which then interact with the photocathode to cause additional pulses.

Some current will always flow through a PMT, even when there is no light incident onto the photocathode, which is called dark current or dark counts. Different photocathode materials will exhibit different levels of dark counts, ranging from tens to thousands of counts-per-second. These are caused by thermionic emission from the electrode surfaces, leakage current and scintillation due to effect from cosmic rays. However, in a TCSPC setup the typical count rates are on the order of $10^6 - 10^8$ cps, meaning the dark current influence is negligible.

Single-photon Avalanche Diode (SPAD)

In contrast to PMTs, SPADs are semiconductor solid-state devices, typically made of silicon for visible wavelengths, or InGaAs/InP based. Avalanche photodiodes operate by applying a high reverse bias across the diode, so that any electrons produced by incident photons produce additional electron-hole pairs as they move through the material. This effectively provides gain on the order of $10^2 - 10^3$. To further improve the gain and reach single-photon sensitivity, the bias is pushed even higher, to a point just above the avalanche breakdown voltage, as shown in Figure 4-3 (a). This operation mode of SPAD is called 'Geiger Mode' [94]. At this level of bias, a single photon incident on the diode can cause a self-sustaining avalanche effect. This leads to a rapid rise in current to a level detectable by suitable electronics. After the detection event, the diode gets reset via quenching of the avalanche which brings the reverse bias back below the breakdown voltage and prepares the device for further detections.

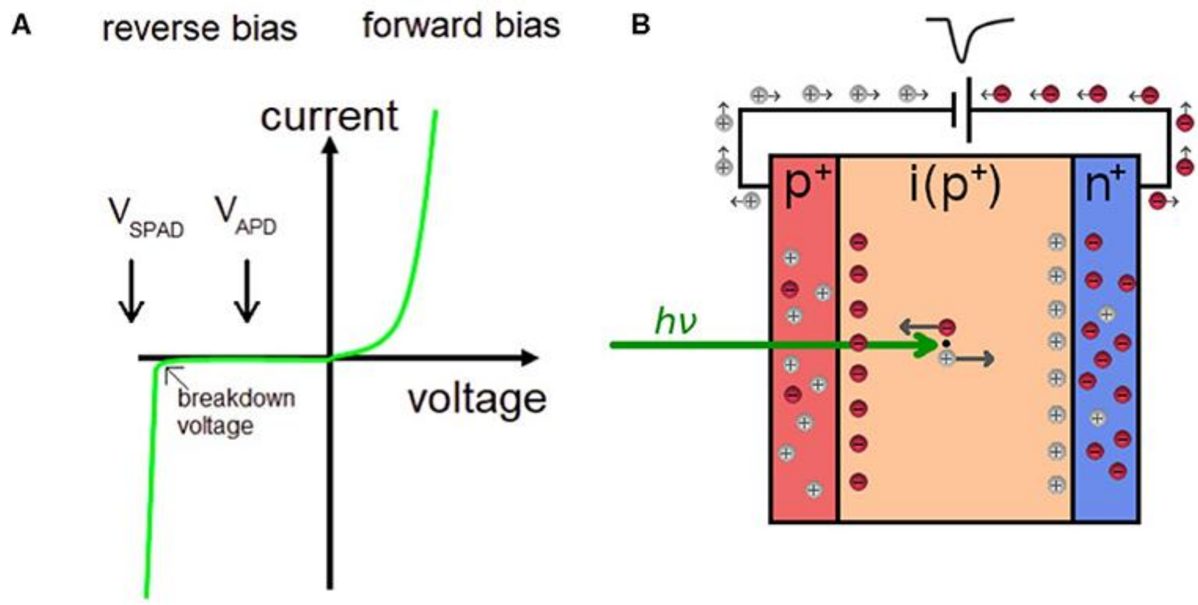

Figure 4-3 (a) I-V curve of an avalanche photodiode. When operated at a reverse bias voltage that is just above the breakdown voltage, single photon sensitivity can be achieved. (b) schematic of a p-n junction that SPAD's are based on. A photon has to directly hit the depletion region to produce an additional current carrier and cause an avalanche effect. (Source: © 2020 Hirvonen and Suhling[95] used under CC BY 4.0)

SPAD's dark count rates are proportional to the active area and inversely proportional to operational temperature. As the active areas are usually smaller than those of PMTs, the absolute dark count rates are significantly reduced, down to the order of $\sim 10^0 - 10^2$ [96]. SPADs also exhibit afterpulsing, which is caused by various impurities and defects within the semiconductor material, creating traps. After a detection event, the trapped carriers can trigger the avalanche again, generating afterpulses [97]. This is reduced by the quenching process and the probability is inversely proportional to the detector deadtime. Finally, SPADs also feature an effect called afterglow [98], caused by some carriers recombining radiatively, resulting in some luminescence during the avalanche process. In some instances, the afterglow can trigger any other detectors present in the setup and appropriate filtering must be used.

The main drawback of SPADs for this application is the added complexity when aligning the system due to their small active areas. SPADs range between $10 - 100\ \mu m$ making focusing of PL emission very challenging.

Hybrid multiplier tube (HPMT)

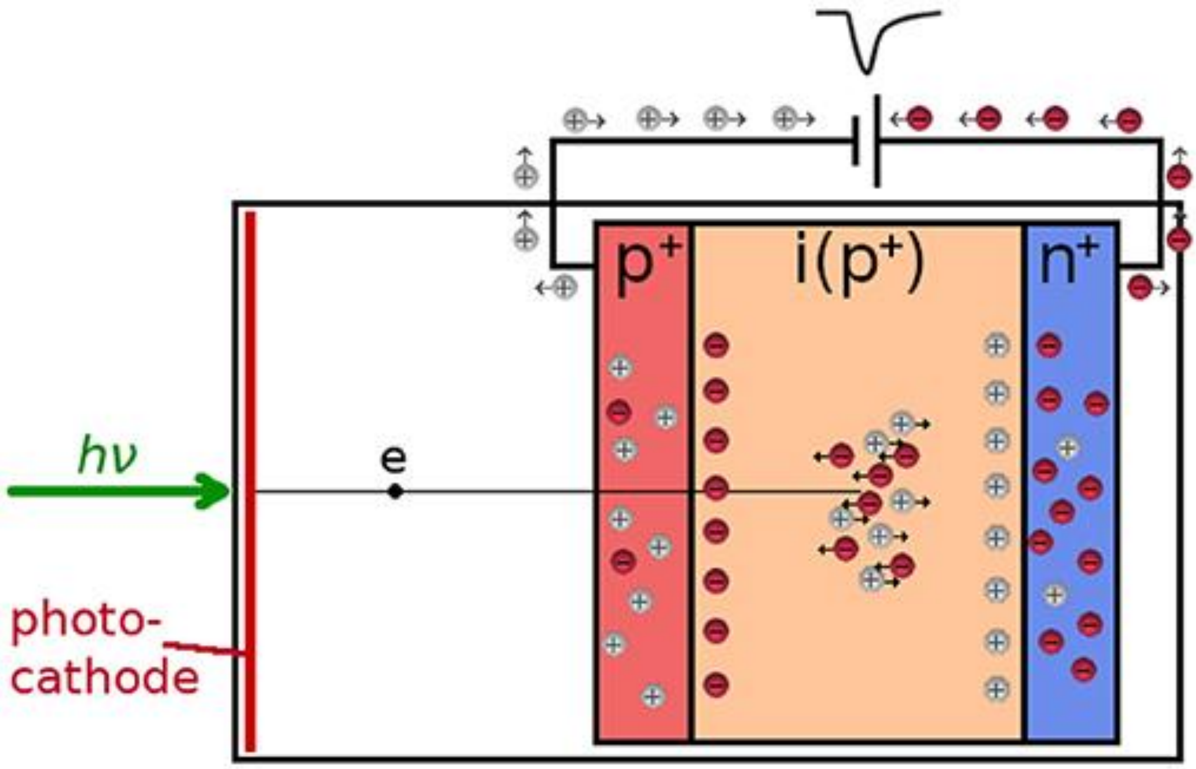

Figure 4-4 Schematic of a HPMT. A photon incident on the photocathode causes an emission of an electron which is accelerated towards the p-n junction. (Source: © 2020 Hirvonen and Suhling[95] used under CC BY 4.0)

A hybrid PMT is a modified version of the standard PMT that incorporates silicon avalanche photodiode inside the evacuated vacuum tube, schematic of which is shown in Figure 4-4. The hybrid PMT combines the advantages of both traditional PMTs and solid-state amplification, resulting in improved performance.

In a hybrid PMT, the APD is placed at the location where the dynodes are traditionally present in a standard PMT. An electron emitted from the photocathode gets accelerated through a high voltage onto the APD. The APD adds additional gain, making the overall electrical pulse sufficient to be detectable when combined with suitable preamplifier.

The combination hybrid PMTs offer significant advantages when compared to SPAD or PMT, overcoming some of the limitations present in both. They do not exhibit afterpulsing and the acceleration caused by high gain voltage leads to narrower transient time spread of the detector improving the timing resolution compared to standard PMT. As a result, these have now become the most common detector type for TCSPC applications.

Other detectors

Two more detectors suitable for photon counting experiments, superconducting nanowire single photon detector (SNSPD) and multichannel plate (MCP), are described in this section. However, these were deemed unsuitable for this project due to practical limitations.

SNSPD have newly emerged over the last couple of decades and are an active field of research [99]. These boast significantly higher detection efficiencies, lower dark count rates and lower timing jitters, significantly surpassing every other type of detector available [100,101]. Commercial products are also available on the market and there is literature of using these detectors for TCSPC applications [102]. However, these detectors must be operated at liquid helium temperatures, with typical operation temperatures reported between 1-4 K. As a result, these would be unsuitable for this type of project due to the associated infrastructure, complexity, and the cost.

A more common type of detector is MCP first produced in the 1960s [103]. The operational principle of these is similar to PMT, however instead of using discrete dynodes, the detector contains small glass tubes lined with photosensitive coating, leading to continuous amplification as the electrons travel through them. The main limitation of these are the low maximum count rates that can be obtained, on the order of 10^4 which would severely limit the experiment speeds. Additionally, these are reported to have a relatively low device lifetime.

Chosen detectors

After considering the available options it was decided that a larger detector area is beneficial in this setup. Aligning PL emission into <100 µm active area of SPAD would be too challenging, making signal collection challenging. Therefore, best choices are either a PMT or a HPMT.

For visible range, B&H HPM-100-50 HPMT was chosen with a GaAs photocathode. The larger detector area as well as narrow and clean instrument response function (IRF) were desirable for the application to make the fitting of the TRPL decays more reliable. The quantum efficiency throughout its spectral range is displayed in Figure 4-5.

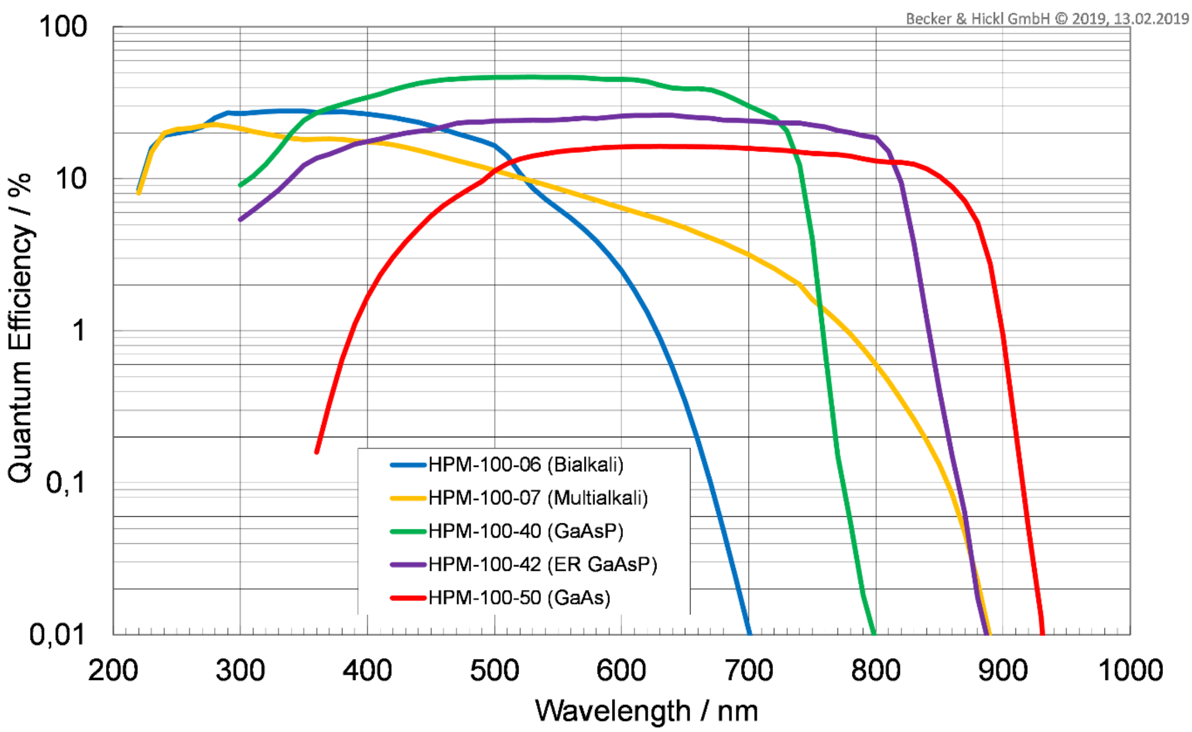

Figure 4-5 The quantum efficiencies of hybrid PMTs offered by B&H. The GaAs based PMT, shown in red was the most appropriate for this project.

The range of options available in the NIR were more limited. No HPMTs were found on the market at the time of designing the system. Therefore, it was chosen to go for H10330C-75-C5 PMT from Hamamatsu with InP/InGaAs photocathode. The quantum efficiency is displayed in Figure 4-6.

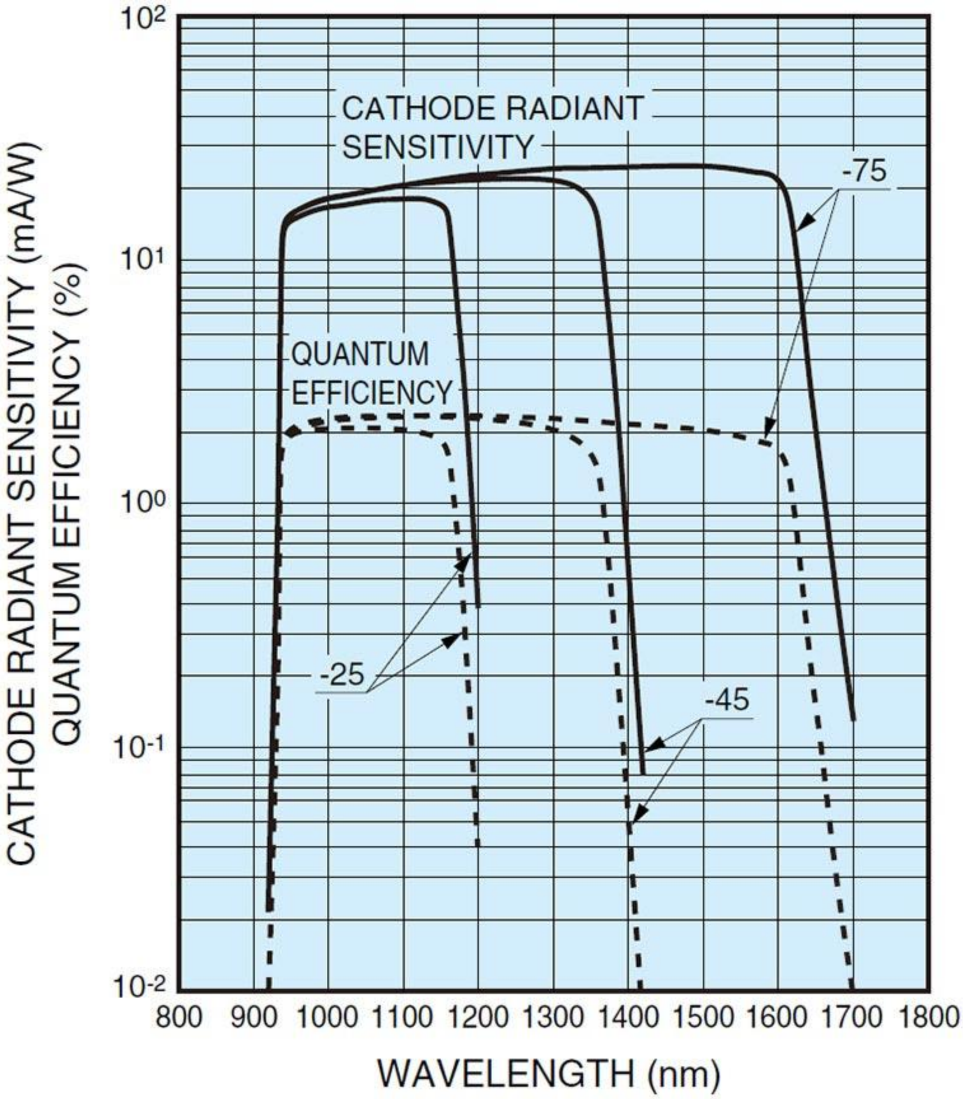

Figure 4-6 Quantum efficiency graphs of NIR PMTs offered by Hamamatsu. The detector chosen for this project is marked with -75 lines.

4.2.3 TCSPC electronics

Accurate timing electronics are necessary to perform TCSPC measurements. The electronics must reliably and accurately determine the timing between the laser excitation pulse and a corresponding pulse from the detector. A TCSPC module (SPC-130-EMN) was acquired from B&H as a part of the whole TCSPC system.

The module automatically divides all the photon arrival times within the specified collection time into a histogram. Typically, the timing window is the inverse of the repetition rate of the laser. The number of histogram bins within this time window is controllable, up to a maximum of 4096 bins, which equates to temporal resolution of 12 ps when using 20 MHz repetition rate laser pulses. The module can store up to $2^{16} - 1$ counts per channel and quotes a maximum useful count rate of 6 MHz.

The module operates using constant fraction discriminator (CFD) principle to accurately time the reference pulses from the detector and laser. Some form of discriminator is necessary to set a threshold when a pulse should be detected. A simple and commonly used type of discriminator is leading edge discrimination, where a fixed threshold voltage is set. If the signal crosses the threshold, this constitutes a pulse, and a timing reference is provided. As highlighted in Figure 4-7, the pulse amplitudes of PMTs greatly vary in amplitude, due to the random amplification processes. Leading edge discrimination would introduce significant timing jitter due to the rise times of the pulses.

Instead, CFD splits the input signal into two and delays and inverts one of them before adding the 2 together, as shown in Figure 4-7. By measuring the zero-cross time of this new signal, the effect of pulse height gets minimised. Additionally, a zero-cross (ZC) level parameter is used to optimise the timing performance. The electronic implementation of this technique is presented and detailed in TCSPC Handbook by W. Becker [104]

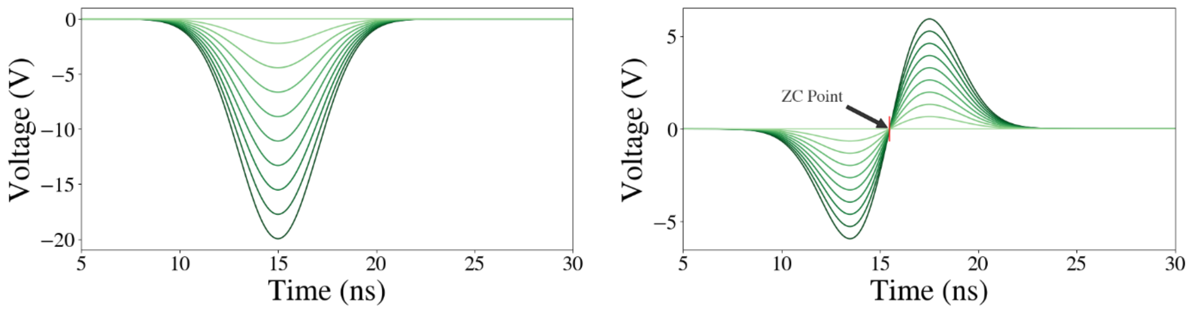

Figure 4-7 Left figure – illustration of some electrical pulses that might be produced by a PMT. We can see that the amplitude varies greatly, making a leading-edge discriminator inaccurate. Right figure – illustration of CFD process. The signal coming from the PMT gets sent down two lines. The second signal gets slightly delayed and inverted before adding the 2 signals together. The zero-cross point in this combined signal is then independent of pulse amplitude.

The module also contains a time-to-amplitude converter (TAC) which converts the timing difference between the laser pulse and the detector pulse into a measurable voltage. This is typically done in a reversed start-stop method. When a photon pulse is detected, a capacitor starts charging, until a subsequent laser pulse arrives and the charging stops. The generated voltage scales linearly with time, therefore measuring the voltage gives accurate timing of the photon arrival. Note that TACs produce some non-linearities near the edges. Therefore, any events that would fall within the non-linear range are discarded.

TAC is accompanied by an analog-to-digital converter (ADC) which processes the TAC voltage into a digital equivalent so that the value can be stored at an appropriate memory location as a 'count' event. The ADC must be able to accurately divide the TAC voltage range into equal bins, which are the width of each timing channel. The electronics necessary for this is complex and must provide extremely reliable and precise results for TCSPC to be feasible. Historically, this used to be the bottleneck component in TCSPC applications. The combined circuitry of TAC/ADC system is quoted to produce an IRF of 3 to 6 ps [104]. However, advances have been made in the processes, significantly improving the speeds.

The electronics have a quoted dead time of 80 ns. Once a detector pulse is detected, all the electronics reset during this dead time before a subsequent pulse can be detected. Therefore, if a detector were to send two detection pulses withing 80 ns of each other, the second pulse would be ignored by the module.

One drawback that was noticed after receiving this module was the interface used to connect it to the PC. The module used an old PCI standard to connect to PCs. However, this is a largely obsolete connector, and newer standard has been used since 2003. Since then, motherboard manufacturers have shifted towards using the newer standard and almost no motherboards made within the last 10 years include a PCI slot. A suitable expansion box was used, allowing to connect the card to a modern PC. Some PC stability issues were experienced as a result of this, leading to many measurements being lost or only completing partway.

For TCSPC electronics to function effectively, the path lengths that the laser reference signal and the detector signal have to travel had to be considered. Every 30 cm difference in the total path length results in an additional 1 ns timing difference. Therefore, on initial design and after making more significant changes to the measurement system, the cable lengths had to be modified to ensure the 2 signals are in-sync. Otherwise, the peak of TRPL might occur in the middle of the timing window, cutting off the tail end of the decays as shown in Figure 4-8.

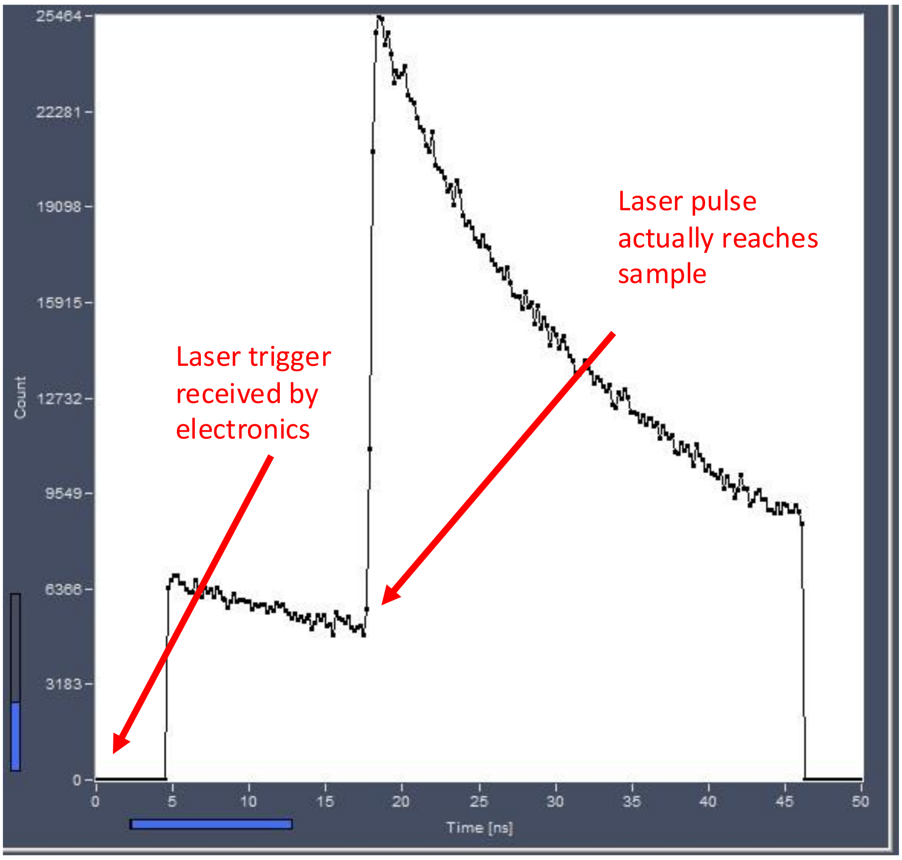

Figure 4-8 Example of a measured TRPL with incorrect path lengths of the SYNC and REF lines. The SYNC and REF lines are approximately 18 ns out of sync in this scenario, resulting in TRPL not fully decaying within the measurement window.

The TCSPC module was provided with its standalone software, which was used for setting up the system and optimising the signal. LabVIEW drivers were also acquired which allowed the development of more complex custom control software including all the system components for acquiring and saving measurements.

4.2.4 Translation stage

A translation stage was a necessary addition to the system. It allowed the raster-scanning measurements as well as accurately positioning the sample within the focal plane of the objective. Stages based on 2 types of technologies were considered – piezoelectric actuator driven stages or stepper motor mechanical stages. Piezo stages offer exceptionally high resolution, often in the nanometre range, but are limited in movement range, which would restrict the ability to scan larger sample areas.

In contrast, stepper motor stages, offer coarser resolution—typically on the order of micrometres. However, they have a much greater movement range, on the order of tens or hundreds of millimetres, allowing spatial mapping of broader sample areas. In this experiment, the movement precision on the order of micrometres was sufficient, allowing enough movement resolution to position the sample within the focal plane.

Linear stages can only move along a single axis. However, multiple can be combined to give multiple degrees of freedom. Stepper motors in these stages drive a lead screw mechanism, enabling the platform’s movement with the desired precision.

The stage chosen for this system was OptoSigma’s OSMS26-100(XYZ)-M6 3 axis motorised stage with HSC-103 stage controller. Photograph of the stage is shown in Figure 4-9. Each axis has a travel range of 100 mm, with resolution of approximately 2 µm. This model was chosen due to meeting the requirements needed for the system as well as competitive price. Additionally, the controller had a straightforward control software and implementation for serial communication, allowing development of control software via Python, LabVIEW or other programs.

Figure 4-9 Optosigma's 3 axis motorised stage that was used in this work.

4.2.5 Optical components

Dichroic mirror

A dichroic mirror reflects certain wavelengths of light whilst letting other wavelengths pass. It was an important part of the system, separating the excitation and emission light. There are 2 types of dichroic mirrors – longpass and shortpass. Longpass allow wavelengths longer than their design wavelength to pass and reflects shorter wavelengths, whereas the shortpass filter works the opposite way around.

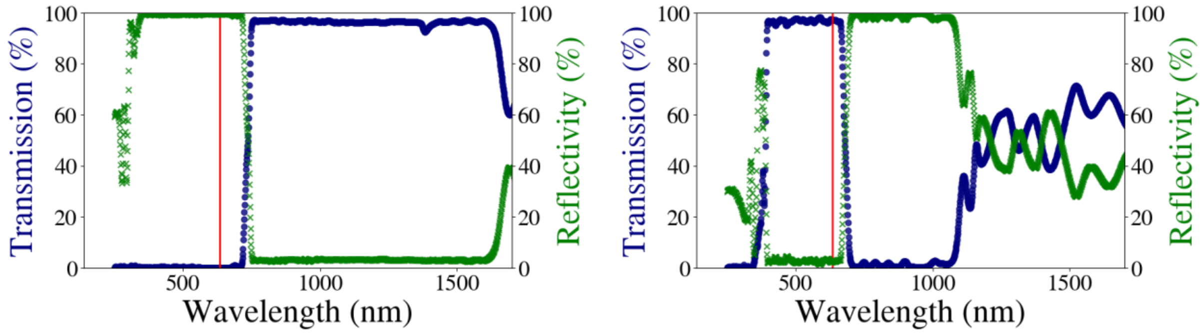

Figure 4-10 The transmission/reflectivity plots of DMLP735B Longpass mirror (left) and DMSP680B Shortpass mirror (right). The red vertical line indicates the excitation laser wavelength. Data provided by the manufacturer (Thorlabs).

Figure 4-10 shows the reflection and transmission data of the 2 filters considered for this system. A useful thing to consider is the amount of laser light that can leak through. In other words, what is the transmission at the laser wavelength of the longpass filter and the reflectivity of the shortpass filter at the same wavelength. These values are important to consider because some of the light incident on the sample will be reflected back through the objective and towards the dichroic mirror. The longpass filter has transmission of 0.01% at 635 nm and shortpass filter has reflectivity of 2.44% at 635 nm.

During initial design, it was decided that the higher amount of leakage light from the shortpass filter was acceptable, and it was chosen instead of the longpass as it allows a more favourable geometry of the optical setup. Figure 4-11 illustrates the difference between the configurations. Using longpass filter would have required mounting the detector aperture facing downwards, towards the optical table or mounting the sample perpendicular to the optical table.

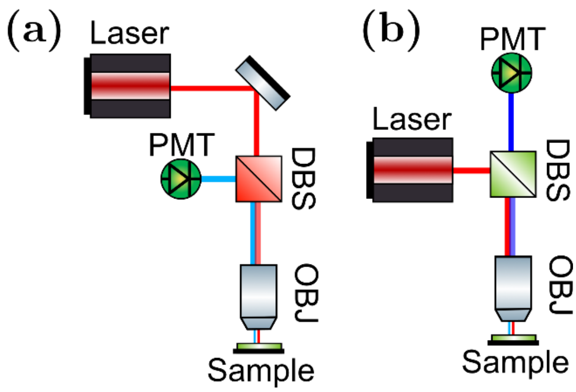

Figure 4-11 (a) Schematic of the configuration when using shortpass dichroic mirror (DBS); (b) schematic when using longpass dichroic mirror. Placing PMT above the DBS filter would require careful planning of appropriate mounting.

Microscope objective

A broad range of various microscope objectives were available, each with specifications tailored to different microscopy applications. In general, for microscopy applications a higher numerical aperture (NA) value is advantageous as it increases light-gathering capacity and resolution [105]. Because of the range of samples that were considered in this work, the objective had to have a broad operating spectral range, spanning into mid-IR. Working distance of >3 mm was required to allow measurement of samples which were encapsulated in glass.

Whilst not critical for the work in this chapter, later developments in Chapter 5 necessitate further considerations. Chapter 5 involves introducing a digital micromirror device (DMD) to project spatial patterns into the laser beam, positioning the DMD in the objective's back focal plane. For this configuration, a large entrance pupil of the objective was desirable to maximise the imaging of the DMD plane, which has an area of $\sim 20 \times 10\ mm$. Additionally, a magnification of at least $10\times$ was beneficial for achieving high spatial resolution. Focusing the laser beam, effectively increased excitation density and, consequently, the TRPL yield from the sample.

After all the considerations, the chosen objective was Thorlabs TL10X-2P, shown in Figure 4-12. Key specifications are detailed in Table 4-2. The objective has good performance in the 400-1300 nm wavelength range, making it useful to measure all samples considered in this work.

Figure 4-12 Thorlabs TL10X-2P microscope used in this work. [106]

Table 4-2 Key specifications of the Thorlabs TL10X-2P microscope objective used in this system.

	Magnification	NA	Working Distance	Wavelength Range	Entrance Pupil
TL10X-2P	10X	0.5	7.77 mm	400-1300 nm	20 mm

4.2.6 Safety measures

An enclosure box was designed to cover the entire optical table, which would contain the entire optical setup. The parts used were standard enclosure components offered by Thorlabs. The enclosure was designed in Fusion 360 software and the model is shown in Figure 4-13. It was chosen to build a large enclosure which would contain plenty of additional room to allow other experiments to be built within the same enclosure as needed. The enclosure allowed safe work without risking laser exposure to the users. Additionally, enclosure made the measurements more stable as the detector was shielded from the outside lights and any fluctuations, reducing dark count rates.

Safety interlocks were placed on the doors of the enclosure which cut off power to the laser when the doors were opened. Additionally, the laser was also connected to the room interlock, which cut off the laser power when untrained users entered the lab. An override box with a key switch was designed and connected, allowing the enclosure interlock to be overridden when alignment work was necessary.

Figure 4-13 3D model of the enclosure designed to contain the TRPL systems developed in this work.

4.3 Laser characterisation

During the system design stage, it was noticed that the laser beam produced was highly elliptical. While a typical beam profile had been provided by the manufacturer, initial discussions concluded that this ellipticity would not pose a major issue. Plans were made to adjust the beam profile using cylindrical lenses to correct the shape, reduce divergence, and improve collimation.

Upon acquiring and testing the laser, however, the beam's characteristics proved more challenging than anticipated. Specifically, the beam's divergence was significant due to its multimode nature, which affected collimation beyond initial expectations. To quantify the divergence, the beam size was assessed at various distances away from the aperture, yielding divergence values of approximately 9.4 mrad along the x-axis and 1.2 mrad along the y-axis.

Even after introducing cylindrical lenses the divergence remained substantial. To help mitigate the beam spread and reduce the final beam spot size, the laser was positioned as close as possible to the microscope objective.

During system assembly, beam profile of the laser beam was measured and shown in Figure 4-14. To measure the beam profile, a camera was positioned 30 cm away from the laser, with an ND filter in front of it. The beam profile is highly non-uniform. In the setup described here, the laser beam was focused into a single spot, therefore measuring the averaged response of the excited area. Therefore, the non-uniformities would not have a significant effect on measured lifetime. Whilst this is not a significant issue in the work described in this chapter, it was problematic for further work, which is covered in the next chapter, as these non-uniformities get convolved with the final images produced.

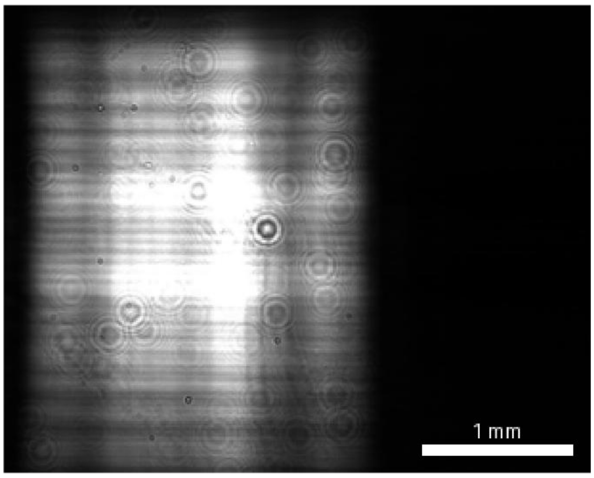

TRPL

Figure 4-14 Laser beam profile measured using camera positioned 30 cm away from the laser with only ND filter in between.

Another important consideration was the laser pulse shape in the time domain, which can introduce non-linearities in the sample response. The exact pulse profile varied depending on the repetition rate and the power level of the laser. The full-width half-maximums (FWHM) of the laser pulses according to the manufacturer ranged between 65 to 300 ps across the parameter range. The laser pulses for 50 MHz repetition rate at a range of powers are illustrated in Figure 4-15. At higher power levels, an additional peak in the pulse profile emerged, which could introduce artefacts in subsequent measurements by convolving the laser pulse shape with the sample's response. This effect is generally minimal when the pulse width is considerably shorter than the measured charge carrier lifetimes. However, the presence of secondary peaks could alter the measured decay characteristics.

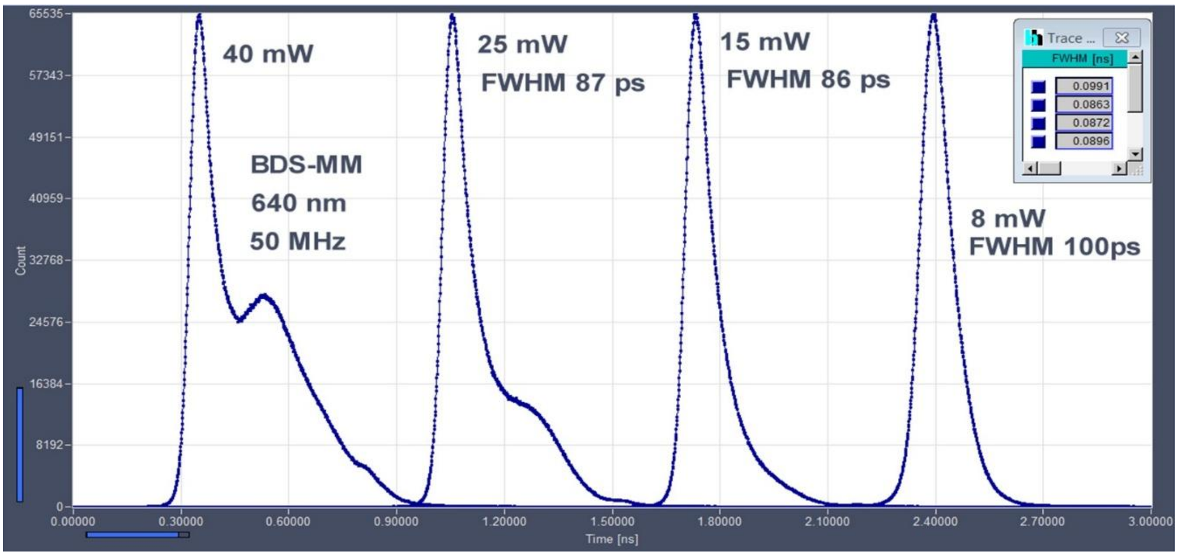

Figure 4-15 Laser pulse shapes at varying power levels of the excitation laser used in this system.

4.4 System assembly

The system follows a commonly used TRPL configuration, in which a pulsed laser is used to excite the sample, and the resulting PL emission is collected through the same microscope objective. The system layout is illustrated in Figure 4-16. The excitation laser source was steered through the shortpass filter and the microscope objective, exciting the sample stage underneath. PL from the sample was collected by the same microscope objective and guided towards the detector by the dichroic mirror. A focusing lens was placed to help collect more of the PL. Some additional optics were placed, such as a 98%/2% beam splitter to allow positioning of a Class 2 alignment laser and some spare filters for adding additional optics further down the line if needed. Furthermore, filters were introduced into the optical path to suppress the residual laser light from reaching the detector. A combination of a longpass filter and a bandpass filter were initially used. The longpass filter had OD=3, and the bandpass filter had OD=5 at the laser wavelength, which should provide an overall OD=8 at the laser wavelength, assuming the reflections between the filters are minimised [107].

Laser leakage presented a significant challenge due to the extremely high sensitivity of PMT detector. This required to minimise any stray reflections within the optical system. To achieve this, the optical beam path was fully enclosed, preventing scattered light from reaching the detector and ensuring light only along the optical beam path could reach the detector. This issue was further complicated as the reflectivity of the various sample surfaces varied. Some materials had high reflectance, which increased the likelihood of laser light reaching the detector, even after passing through the various filters. In an attempt to further suppress the leakage, a notch filter was introduced, to specifically block the laser wavelength. However, even after implementing this, some laser light would still be detected.

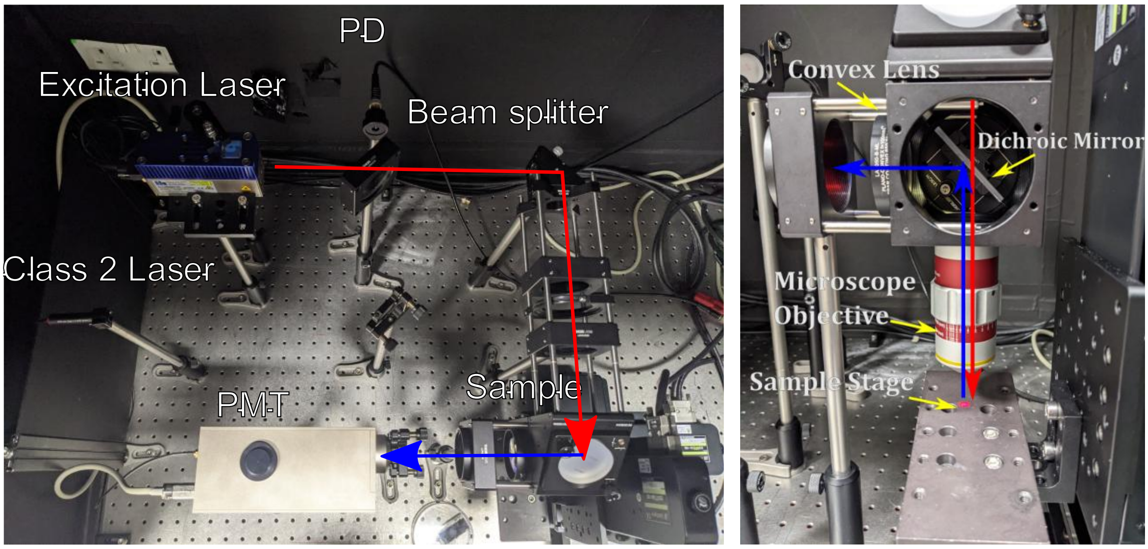

Figure 4-16 Photograph of the initial build of a TRPL measurement system for single point excitation. The left image shows the top side view of the setup. The picture on the right shows a close up image of the cage mount configuration. The laser light path is illustrated using a red line and PL emission path using blue line.

4.5 Data fitting

An essential part of TRPL measurements is accurately fitting the decay data to extract meaningful charge carrier lifetimes. Ideally, the TRPL decay could be modelled with a simple exponential decay function, where the decay constant reflects the lifetime of the charge carriers within the sample. This is often the case in fluorescence microscopy applications, where the decay from the various fluorophores has a well-defined, single exponential decay. However, in applications of semiconductor characterisation, this is typically not the case. As highlighted in Chapter 3.1 the carriers within semiconductors have multiple recombination pathways, each with varying recombination constants. Additionally, the recombination mechanisms will also depend on the device structure. Therefore, the use of multi-exponential decay function is often necessary to provide an accurate fit. In this case, multiple decay constants would be extracted, corresponding to the various recombination pathways, such as non-radiative, radiative, and surface recombination. The overall TRPL intensity can be described by the equation:

$$I(t) = \sum_{i}^{k} A_i \exp\left(-\frac{t}{\tau_i}\right) \tag{4.1}$$

Where $I(t)$ is the TRPL signal of the sample at time t, k is number of recombination paths present, A_i is the amplitude and τ_i is the charge carrier lifetime, for recombination route i. In the simplest case, $k = 1$ where there is only one type of recombination present.

Additionally, the measured TRPL response is inherently convolved with the IRF, which has a broadening effect on the recorded decay. This convolution can obscure shorter-lived decay components, particularly when the lifetimes are close to or below the IRF duration. For this system, the IRF is approximately 150 ps, suggesting that broadening effects can become significant when measuring lifetimes below the nanosecond range [108].

Fitting TRPL data with convolved IRF is known as reconvolution fitting and is described using the equation

$$I(t) = \sum_{i}^{n} A_i \exp\left(-\frac{t}{\tau_i}\right) \otimes IRF(t) \tag{4.2}$$

This requires accurately measuring the IRF of the system, which is a combined effect from the electronics, the detector and the laser. However, measuring the IRF proved challenging as it requires samples with decay constants shorter than the IRF. This was further complicated for NIR detector which could not detect the laser light. Whilst some attempts were made to perform reconvolution fitting, it proved to be unreliable. Additionally, the typical lifetimes for materials investigated in this thesis were significantly longer than the expected IRF of the system. Therefore, it was chosen to not use the reconvolution fitting in any of the results presented here.

Further challenges were introduced due to the laser leakage, especially for highly reflective samples, which could reflect the laser light towards the detector, despite the various optical filters. This leakage, presented as a fast, initial drop in the TRPL decay, linked to the pulse width of the laser. For highly reflective samples, such as polished GaAs wafers, this effect obscured the TRPL response of the sample entirely. Therefore, the use of the Hamamatsu NIR PMT was typically preferred where possible, as the laser wavelength was outside the spectral range of this detector.

Before performing the data fitting, some pre-processing steps were employed. Every TRPL measurement contained some bins at the start and at the end of decay with 0 counts, due to TCSPC electronics. The peak of the decay was identified, and the data fitting restricted to the region from the peak until the decay reached zero. In some cases, it was also attempted to subtract the background dark count rate of the system, however, it was determined that this is not necessary as the dark count rate does not change the decay time of the signal.

Additionally, as a further attempt at reducing the effects of laser leakage, some attempts were made to offset the starting point of the fit to some bins after the peak. As the laser intensity drops off much quicker than TRPL, this approach should reduce the laser effect on the fitted decay constant. However, this made the fitting somewhat arbitrary in terms of defining how big this offset should be. It was found that the decay constants would change depending on the size of this offset, making the overall fitting unreliable.

The fitting process itself was carried out in Python, using non-linear least squares methods implemented via the `scipy.optimize.curve_fit` [70] library, allowing to attempt fitting of any arbitrary functions. The measured decays were always first fitted with a single exponential decay, before shifting to a double exponential model. Whilst in principal, triple and higher exponential decay models could be employed, the literature around the samples considered in this work typically only described single or double exponential decays.

4.6 Results

This results section is included to demonstrate the successful development and functionality of the TRPL measurement system, which was the primary objective of this chapter. Measurements were conducted on a variety of samples, however results for CdTe and CIGS samples are provided here. These particular samples were used due to available literature, allowing comparison of the obtained results with published data. Therefore, these sample measurements serve as proof of concept, demonstrating the system's capabilities of capturing key photoluminescence characteristics.

4.6.1 CdTe

As discussed above, the first TRPL measurements were carried out on CdTe PV device. This sample was chosen due to the availability of characterisation data, including prior TRPL measurements published on the same device, allowing for a direct comparison of results and validation of the system's performance.

Figure 4-17 shows the TRPL decay of a single point of the CdTe device, measured using the system developed in this chapter and fitted with a double-exponential decay model. A bandpass filter with 820-830 nm band was fitted to only allow the PL from the sample. Conveniently, laser leakage was not a concern with this sample. The amount of laser light reflected off the sample was minimal, reducing the back reflections of the laser into the detector. The unabsorbed light appeared to be scattered off the sample, rather than reflected. This allowed for a high-quality fit without significant interference from the excitation pulse.

The TRPL decay resulted in charge carrier lifetimes of 2.2 ns and 14.1 ns. These lifetimes corresponds to charge separation in the p-n junction and recombination in the bulk material respectively, according to [109]. TRPL measurements of the same sample have also been described in work carried out by V. Tsai et al. [110], where the faster lifetime was shown to range between 1.5 to 3 ns, depending on the sample region. This close agreement supports the accuracy of the system's initial configuration and provides confidence in its ability to capture meaningful TRPL data. Furthermore, the successful fit and alignment with established data indicate that the system is well-suited for further TRPL measurements across similar materials, particularly for mapping lifetime variations within a sample. However, the fitted model shows noticeably poorer agreement near the end of the decay, indicating that further refinement of the model may be necessary to improve the accuracy of the lifetime extraction from the TRPL curves.

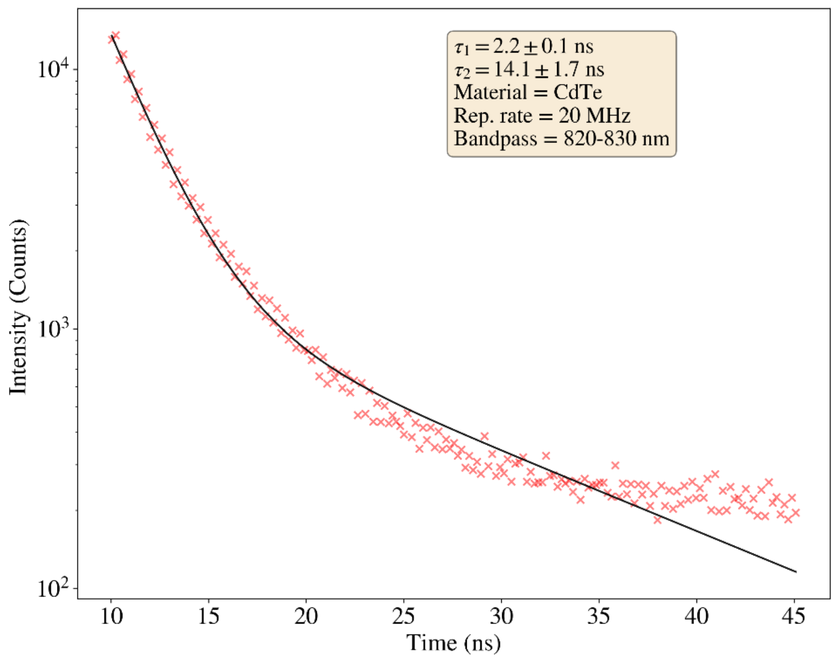

Figure 4-17 Time-resolved photoluminescence measured of CdTe PV sample with a double exponential decay fitting.

To further investigate the sample and evaluate the system's capabilities, the next step involved imaging the sample by measuring the TRPL at each point. The total area imaged was 23 × 35 mm, measured using a raster scanning approach on the x-y translation stage, achieving spatial resolution of 0.1 mm and temporal resolution of 200 ps. The resulting images are shown in Figure 4-18. Given the double-exponential decay characteristics of the sample, two lifetime maps were generated, corresponding to the decay constants τ_1 and τ_2. The spatial resolution in this case was limited by the focused beam spot size, which was approximately 0.1 mm on the sample surface. Dark regions surrounding the sample indicate areas outside the sample boundary where no TRPL signal was measured.

Due to the raster scanning method, this measurement was time-intensive, as each measurement point required a few seconds to acquire, resulting in the overall data acquisition of approximately 48 hours. Nonetheless, this experiment represented a significant milestone, demonstrating that the developed system could successfully produce spatially resolved TRPL maps. This capability provides a foundation for further system enhancements, specifically through integration with the compressed sensing approach discussed in the following chapter, aimed at achieving faster and more efficient TRPL imaging.

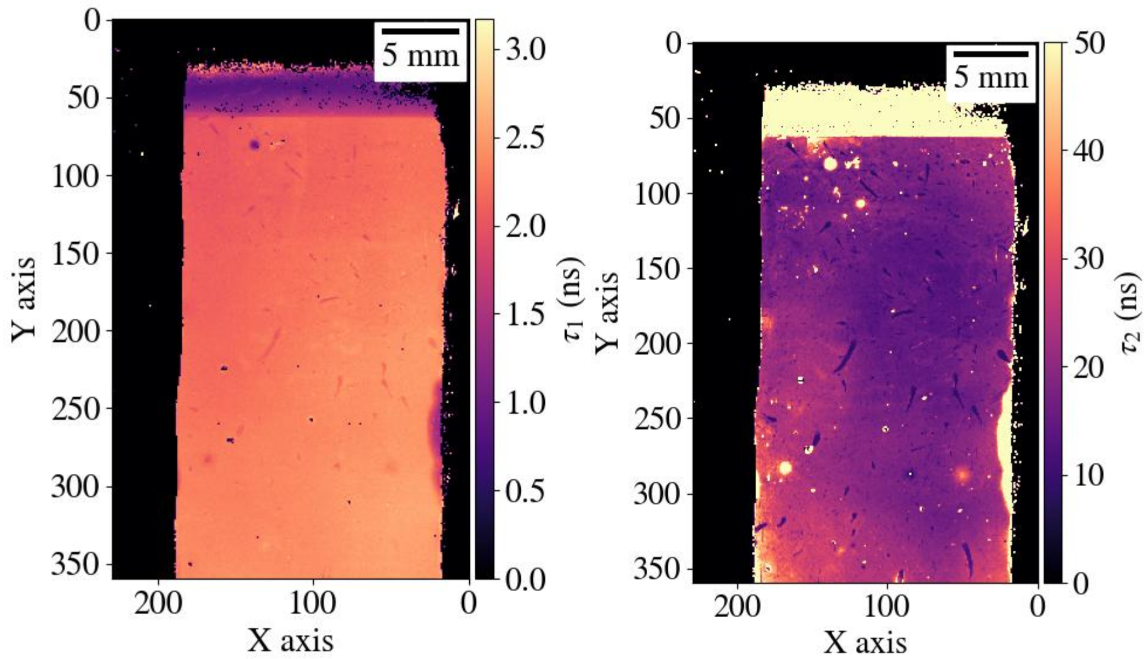

Figure 4-18 Lifetime maps of a CdTe sample acquired using a raster scanning TRPL imaging approach. For every point of the sample, TRPL spectrum was acquired, which was fitted with a double exponential function, to extract the charge carrier lifetimes, τ_1 and τ_2. These maps correspond to the two primary recombination methods present in the material, providing insights into spatial variations in recombination dynamics across the sample.

4.6.2 CIGS

CIGS proved to be another sample that was readily available in the lab that was useful to measure. It has a bandgap of 1.175 eV (1055 nm), which meant that the NIR PMT had to be used to measure its TRPL. Whilst this detector is less sensitive than the visible one, it offered an important advantage – the wavelength range of this detector was 950-1700 nm, meaning that some laser light leaking through was not a concern, as it was invisible to the detector.

The TRPL response of available CIGS sample is displayed in Figure 4-19. The acquired TRPL response was best fitted with a double exponential decay and resulted in lifetimes of 6.3 ns and 34.0 ns.

Initial plans included positioning both of the detectors in the system such that a drop-in mirror could be used to select which of the detectors was in use. However, this proved impractical as the PL signal was so low already. It was more beneficial to keep the detectors as close to the source as possible, helping ensure less of the PL light was wasted.

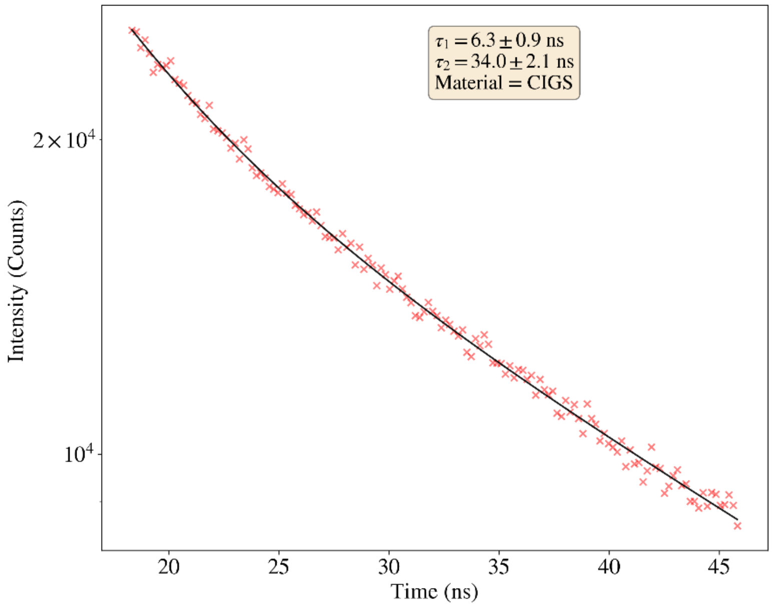

Figure 4-19 A single-point TRPL measurement acquired on the CIGS cell with a double exponential decay fitted to it.

4.7 Chapter conclusions

This chapter detailed the design, development, testing, and improvements of a TRPL measurements system, capable of characterising samples with emissions in the NIR spectral region. A key objective of this work was to establish a robust TRPL system, based on existing design principles, capable of capturing data across a range of semiconductor samples. Crucially, building this system provided a foundational platform for the development work described in the following chapter, where the capabilities of this system are expanded and improved to realise the first experimental implementation of a compressed sensing TRPL imaging system.

Throughout the design process, multiple system components required careful evaluation to ensure optimal performance. The initial step involved considering the materials to be investigated, which in turn guided the selection of components for TCSPC. The key materials identified were CdTe, CIGS, and GaAs, which have emissions in the NIR region. The primary components—detector, electronics, and laser—were evaluated and chosen based on a thorough comparison of specifications from two manufacturers to ensure the setup met the spectral and timing needs of the intended measurements.

A notable challenge during setup was managing laser light leakage, as residual laser light reached the PMT detector despite the use of multiple optical filters and enclosed optical beam path. This leakage introduced a fast-decaying component in the TRPL signal due to the falling edge of the excitation pulse. Attempts were made at correcting for this, as fitting the TRPL signals with laser leakage resulted in underestimated carrier lifetimes. One approach involved offsetting the fit by a few nanoseconds after the peak of the TRPL signal. However, this method proved inconsistent due to the starting point of the fit having an effect on the values of the fit. This issue was not present when measuring CIGS, as the NIR detector used for measuring this material was insensitive to the laser wavelength. Overall, the laser leakage restricted the choice of samples that could be measured.

An integral part of the TRPL system development was the creation of the customised control software, implemented using LabVIEW. This software coordinated the TCSPC electronics with the translation stage, enabling automated data acquisition across the sample area, utilising the development packages provided by the equipment manufacturers. The software allowed precise control over the timing and positioning needed for raster-scanned TRPL imaging. For analysing, processing and visualising the software, separate Python scripts were developed, which enabled the fitting of the TRPL decay profiles and extraction of charge carrier lifetimes.

After the assembly of the system, initial tests carried out on CdTe showed reasonable agreement between the expected lifetime values and the measured ones. However, these measurements also highlighted the inherent challenges in quantifying carrier lifetimes in absolute terms. The carrier lifetime values extracted from TRPL measurements are very challenging to quantify in absolute terms, as they do not exhibit sufficiently high precision. Carrier lifetime values were found to be highly sensitive to the material properties, experimental setup, and the specifics of the data fitting algorithms. Therefore, this suggests that these types of measurements are more suited for qualitative comparison.

The system demonstrated in this chapter successfully demonstrated the capability to map carrier lifetimes across an entire sample area, providing a valuable tool for material characterisation. This TRPL imaging approach enables identification of regions with shorter lifetimes, which may indicate areas of interest for further analysis. However, some limitations are present due to the raster scan approach. The spatial resolution is constrained by the illumination beam spot size, which is determined by the laser beam and microscope objective. Additionally, the measurement acquisition speed is also limited, requiring several seconds to acquire each data point in the final image.

The next chapter focuses on advancing this system through implementation of compressed sensing, aiming to achieve a faster and more accurate measurement system compared to the raster system described here.

Chapter 5 Implementing Compressed Sensing for Time-Resolved Photoluminescence Imaging

This chapter outlines the development and implementation of a prototype compressed sensing time-resolved photoluminescence (TRPL) measurement system. Building upon the simulation model and experimental setup described in chapters 4 and 5, the system was modified to incorporate a digital micromirror device (DMD) and other necessary components. These modifications aimed to enable spatial control of excitation patterns, allowing for the encoding of the measurement matrix directly into the excitation light.

Whilst chapter 4 demonstrated that compressed sensing TRPL is feasible in simulations, this chapter presents results that confirm its practicality in real-world experiments. The primary goal was to develop and showcase a working prototype of the system, providing experimental validation alongside the theoretical models. This chapter also highlights how the addition of the DMD enabled other measurements based on compressed sensing, expanding the system’s functionality beyond TRPL.

The key modification involved adding a DMD and a suitable tube lens to the existing TRPL setup, which allowed precise control over the spatial domain of the excitation light. The integration of the DMD and the tube lens was essential to focus the DMD patterns onto the sample, ensuring that the compressed sensing method could be applied. A detailed description of the updated experimental layout is provided, along with a schematic illustrating the new components and their placement within the system.

In addition to performing CS TRPL measurements, the DMD setup allowed for other compressed sensing-based imaging techniques to be explored. For instance, a simple photodiode was used to capture a high-resolution laser beam profile by projecting patterns onto the beam and reconstructing the profile using compressed sensing algorithms. This demonstrated the versatility of the system, as high-resolution spatial information was obtained without the need for complex detectors or expensive equipment.

Furthermore, the system was also employed to perform photocurrent microscopy measurements of photovoltaic (PV) devices using the same compressed sensing and pattern projection approach. This allowed for the acquisition of high-quality photocurrent maps while significantly reducing acquisition time compared to traditional raster scanning methods. These additional capabilities highlight the broader applicability of the DMD-enabled compressed sensing framework beyond TRPL, demonstrating its utility in a range of optical measurement tasks.

Several validation methods were explored to assess the accuracy and effectiveness of the compressed sensing TRPL measurements. Initial attempts involved comparing compressed sensing TRPL results with compressed sensing photocurrent mapping data, although this approach was later revised due to potential differences in carrier recombination behaviour between the two methods. Alternative validation strategies, such as fabricating samples with known features using a focused-ion beam (FIB) and conducting raster scanning TRPL measurements, were explored to provide more reliable comparison points.

This chapter also addresses the challenges encountered during system implementation, including issues related to laser beam quality and noise management. Various methods were tested to mitigate these challenges, such as using a silicon photodiode to measure the laser beam profile and adjusting the system alignment to improve signal-to-noise ratios. Additionally, system characterisation was performed by analysing dark count rates, noise sources, and the stability of the TRPL signal over time.

The results of the compressed sensing TRPL measurements are then presented, comparing the performance of the prototype system to conventional raster scanning techniques. The data demonstrate the feasibility of the compressed sensing TRPL approach, not only theoretically but also in practice, with comparisons highlighting the system's ability to reconstruct TRPL images while reducing acquisition times. The chapter also presents results from higher-resolution compressed sensing TRPL measurements, showcasing the system's capability to achieve finer spatial resolution at reduced sampling levels.

5.1 Modified experimental layout

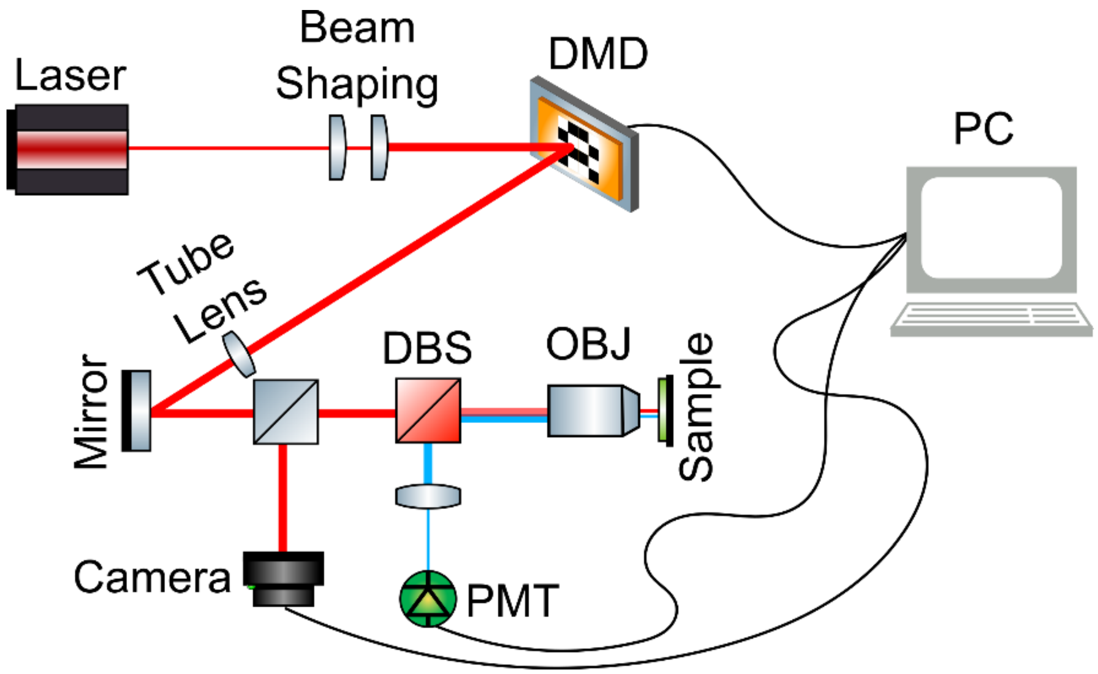

Figure 5-1 Schematic of the experimental layout used in the measurements carried out in this chapter.

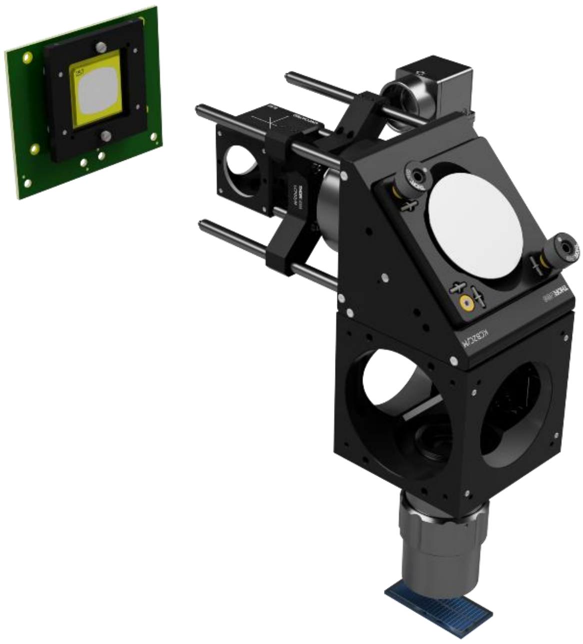

Figure 5-2 A rendered image of the main parts of the CS-TRPL system. Laser and detector are not shown.

The key modification to the experimental layout, compared to the one used in previous chapter is the addition of the DMD and a suitable tube lens. The tube lens used was Thorlabs TTL200-S8, which was recommended with the microscope objective used in this system. One of its benefits was a broad spectral range, making it compatible with the rest of the system. Its working distance was 151.8 mm. The DMD and tube lens were positioned such that the image of the DMD falls exactly at the back focal plane of the microscope objective. This meant that the patterns produced by the DMD were in focus at the focal plane of the objective.

5.2 Introducing DMD to TRPL measurement system

As described in the previous chapters discussing compressed sensing; to successfully carry out compressed sensing measurements, accurate control of the sampling domain is necessary. In the case of imaging applications, the spatial information of the excitation light must be precisely controlled. This allows to excite the sample with arbitrary patterns, encoding the measurement matrix into the excitation light itself.

To allow for this, a digital micromirror device was used, which is a type of Microoptoelectromechanical system (MOEMS) device. It is a form of spatial light modulator, first introduced and patented in 1980s by researchers at Texas Instruments [111]. Texas Instruments initially aimed to design an analogue version, allowing for control of the tilting angle of each mirror. However, this proved to be too challenging at the time and it was decided that a digital device would be sufficient for meeting the requirements. These devices are exclusive to Texas Instruments. They have been widely used in a variety of applications, but most predominantly in digital projectors, particularly larger ones. In the last couple of years, they have also been adopted by some 3D printer manufacturers for resin-based printers.

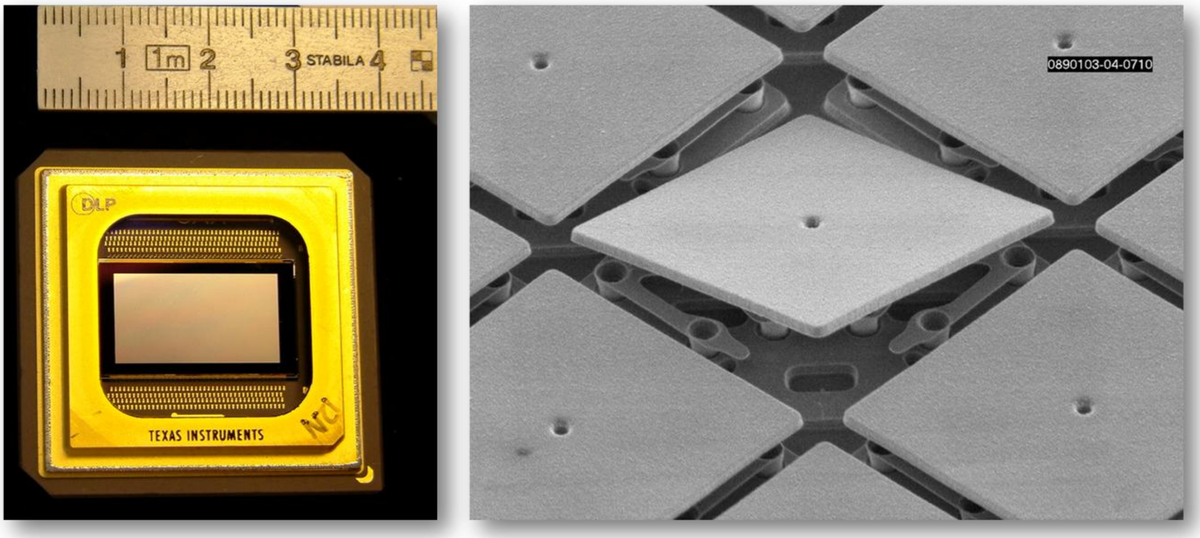

Figure 5-3 (Left) An image of a DMD (right) a close up microscope image revealing individual mirrors.

Digital Micromirror Devices (DMDs) are versatile components consisting of a large array of individually addressable micromirrors, as illustrated in Figure 5-3. These devices are widely used in digital projection systems and other imaging applications, with typical array sizes matching common display resolutions such as 1920 × 1080 pixels. The size of each micromirror varies depending on the specific model, ranging from 7.6 µm × 7.6 µm for high-resolution arrays to around 15 µm for standard configurations. In all cases, the gap between adjacent micromirrors is approximately 1 µm. Each micromirror is mounted on a silicon oxide memory cell formed by dual complementary metal-oxide-semiconductor (CMOS) elements, which determine the binary state (TRUE or FALSE) of each mirror. This state controls the tilt angle of the micromirrors, typically ±12° or ±10° depending on the model.

This binary control enables each micromirror to reflect light in one of two distinct directions, depending on whether it is set to the “on” or “off” state. The tilt is achieved through a yoke structure that allows the micromirrors to pivot about a pair of torsional hinges. This configuration enables precise spatial modulation of light, allowing DMDs to project arbitrary patterns onto a target area. For imaging applications, the spatial resolution of the projected patterns is governed by the micromirror dimensions and the optical configuration of the setup. A key advantage of DMDs is their fast switching speed, reaching up to ~50 kHz in modern systems, which facilitates the generation of greyscale levels through rapid switching between the TRUE and FALSE states.

DMD technology is known for its robustness and reliability, with extensive testing showing operational lifetimes exceeding 100,000 hours without significant performance degradation. However, initial durability studies identified certain failure mechanisms, such as hinge memory and surface contamination. Hinge memory can occur when a micromirror remains in one position for an extended period, leading to a slight drift in its resting position over time. Meanwhile, surface contamination from foreign particles can obstruct micromirror movement and even cause physical damage. Despite these issues, the calculated mean time between failures (MTBF) for DMDs is reported to exceed 650,000 hours, and the devices have demonstrated stability under extreme environmental conditions, including high temperatures and intense light exposure.

5.2.1 Laser issues

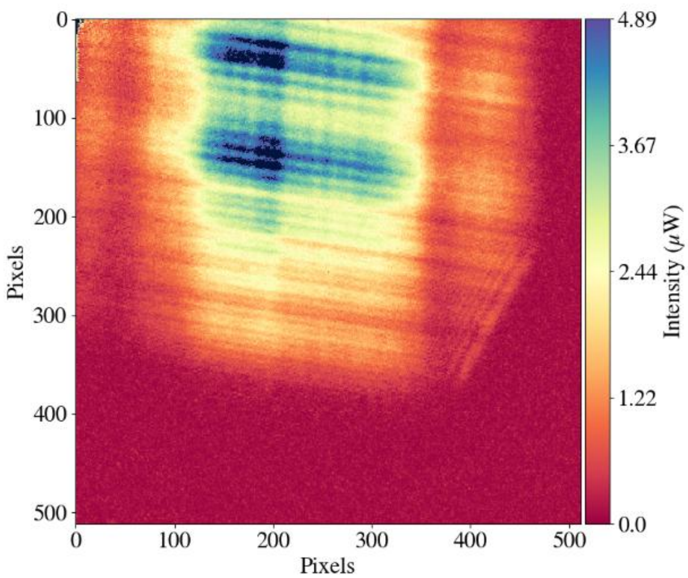

Figure 5-4 Laser beam profile acquired using compressed sensing at the sample plane.

One of the big limitations for this measurement technique was the beam profile of the laser used for sample excitation. This was discussed previously in Chapter 4.3 as part of developing compressed sensing system it was possible to use a Si photodiode in conjunction with the DMD to measure the beam profile. The overall setup was the same as shown in Figure 5-1, except with a photodiode positioned at the sample plane, focusing the laser beam on its surface. The current through the diode was then measured for a series of projected patterns. The reconstruction algorithm was then used to acquire the beam profile. The final reconstructed image agrees very well with the beam profile measured directly using a camera.

This illumination profile presented several challenged to compressed sensing TCSPC measurements. The heterogeneous excitation intensity created a fixed-pattern noise that adversely affected the reconstruction quality. Some approaches could be potentially implemented to improve the uniformity and mitigate its effects on the measurements.

Improving illumination uniformity could be achieved through optical means. One effective method would be incorporating a holographic diffuser in the beam path before the DMD. Such diffusers can transform a heterogeneous laser beam into one with a Gaussian or even ‘top-hat’ profile, which would significantly reduce the intensity variations across the field of view. For a laser source, this might introduce speckle patterns into the beam profile which would present their own issues in this system. Therefore, it would likely require the addition of a despeckle device such as a rotating diffuser or an acousto-optic modulator to further homogenise the illumination. These optical solutions could potentially address the non-uniformity problem at its source, providing a more ideal illumination profile for this application.

Furthermore, the non-uniformity problem could also be potentially mitigated through computational approaches. Flat-fielding techniques are commonly used in various imaging applications, ranging from astronomy to mobile phone cameras. Flat-fielding involves dividing the measured signal at each pixel by a reference "flat-field" image that captures the illumination non-uniformities. In this case, the beam profile measured using the photodiode and DMD could serve as this reference. Implementation would involve incorporating the known beam profile into the reconstruction algorithm as a weighting factor for each spatial position by either dividing the final reconstruction or incorporating into the measurement matrix directly, before carrying out the reconstruction.

Nonetheless, there are important caveats to these approaches. For flat-fielding to be effective, the spatial variation in excitation must not lead to fundamentally different responses across the sample. For instance, if the excitation density varies enough to induce different recombination mechanisms in different regions, then the assumptions underpinning flat-field correction may no longer hold. Moreover, optical methods must be carefully designed to avoid introducing additional aberrations or spatial artefacts that could degrade the compressed sensing reconstructions.

5.3 Photocurrent microscopy measurements

Compressed sensing photocurrent measurements have previously been extensively studied and described in previous works published by G. Koutsourakis [42,112]. To carry out these measurements, the existing system only needed a minor modification. Because these types of measurements had previously been demonstrated, it was a beneficial way of testing whether the compressed sensing calculations and projection optics were functioning as expected.

To carry out these measurements, InP-based PV device was used. Light incident on the sample caused the current produced by the cell to vary, corresponding to the amount of incident light. To carry out the compressed sensing photocurrent measurements, a series of measurement patterns were projected onto the device and the current produced was recorded. After the measurement was complete, using the described reconstruction algorithm, the overall photocurrent map was reconstructed, as shown in Figure 5-5.

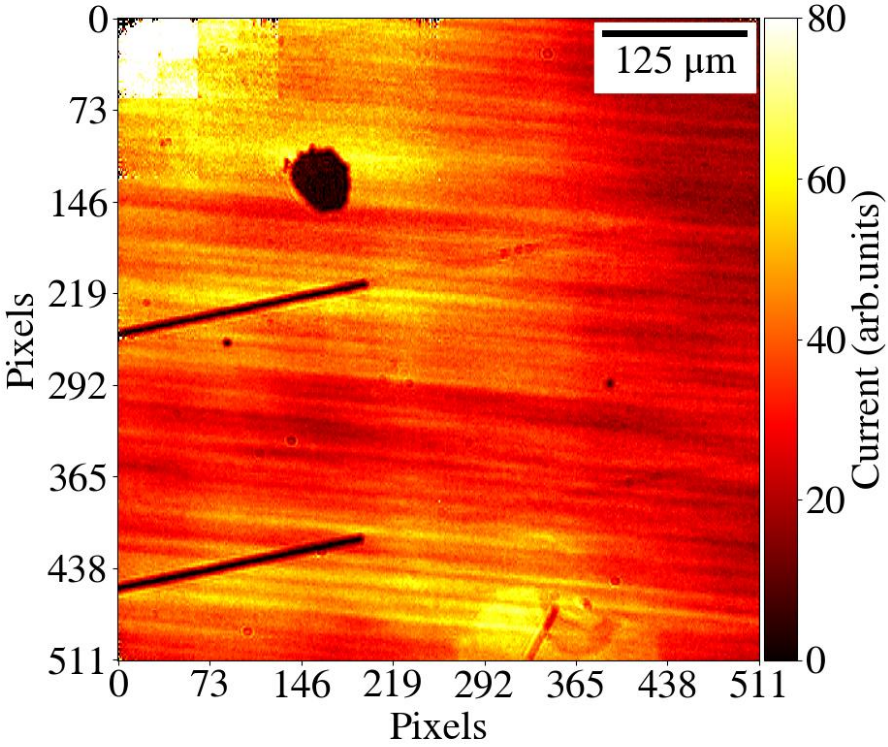

Figure 5-5 A photocurrent response map of InP PV device acquired using compressed sensing current microscopy.

The reconstructed image shown was acquired using 50% sampling level. The more prominent features of the sample are accurately reconstructed, such as the contact lines as well as a few larger defects. However, the non-uniformity of the laser beam dominates the finer details.

For current mapping measurements a pulsed laser source is not required. As a continuous wave single-mode laser source was available, it was beneficial to try using it as an excitation source. The laser could be easily swapped out and after realigning the system, some measurements could be acquired. In this case, a GaAs reference cell was used.

The reconstructed image, shown in Figure 5-6, agreed very well with the observations from the optical imaging measurements. The big scratch in the middle of the cell was identified. In the top left corner of the image, some artefacts are visible, which are introduced due to the reconstruction algorithm. The reconstruction uses Haar wavelet transform. However, it has some coherence with the lower order projection patterns, resulting in visible artefacts for the final reconstruction, visible in the top left of the image. Some fringe patterns are also visible in the acquired image, which are due to dust particles on the surfaces of optical elements.

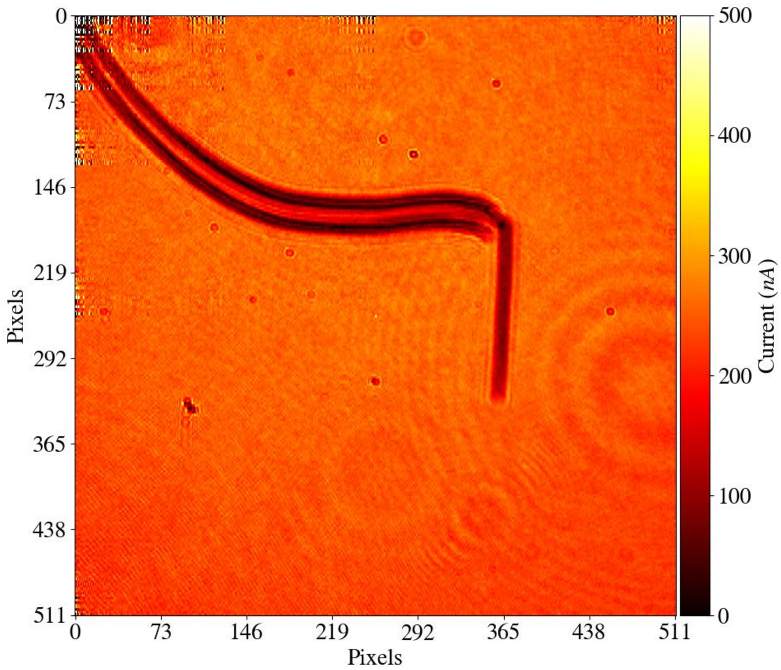

Figure 5-6 A photocurrent map of a GaAs reference cell acquired using compressed sensing techniques.

Regardless, the compressed sensing photocurrent imaging measurements were successful, achieving a 512×512 pixel resolution image in approximately 10 minutes. Carrying out these measurements provided confidence that compressed sensing TRPL measurements should be achievable as well. The optical system was known to function as expected, allowing for the measurement theory to be implemented in practise.

5.4 Towards TRPL imaging

One important challenge in developing a novel imaging method is having a suitable reference to compare the acquired images to. Without having anything to compare against, the new methodology cannot be validated. To validate the measurement, the spatial information of the sample must be known, which can be achieved in multiple ways. For example, this could mean having a different imaging method that is already validated and measures the same or comparable parameter. By measuring the same part of the sample with the 2 different methods and comparing the results, a new method can be validated. An alternative approach would be fabricating a sample in such a way that the spatial features that are expected to be seen are already known.

For compressed sensing TRPL measurements, multiple validation techniques were tested. The initial approach was to image sample area using compressed sensing photocurrent mapping technique described above and then measure the same area using compressed sensing TRPL. However, it was later decided to seek an alternative approach, as there was not conclusive evidence to determine if a photocurrent map could be compared to TRPL map. The carrier recombination inside the material is likely to behave differently and therefore result in a different image.

Finally, another approach to validation was imaging the sample using raster scanning TRPL method. Raster scanning offers the best comparison to compressed sensing measurement. By raster scanning, the same property can be measured (TRPL in this case) over the same area. In this system, there were 2 ways for carrying out raster scanning. The first is using the translation stage, as described in the previous chapter. However, the spatial resolution would not match the resolution of compressed sensing measurement. When raster scanning using the stage, each pixel is the size of the excitation spot on the sample. Whereas the aim of the compressed sensing is to have the entire image be the size of the excitation spot, meaning that each pixel is much smaller.

Instead, a DMD can also be used to perform the raster scanning. Because the optics are already setup in such a way that the excitation beam is incident onto the DMD, the reflected light can be controlled. It can even be set to only turn on a single DMD mirror or grouping multiple DMD mirrors to act as larger pixels. The benefit of this approach is the fact that the exact same setup is used for validation as for the compressed sensing TRPL measurement. Any non-uniformities in the beam profile would also be included and compared. However, the majority of excitation light is wasted in this approach – only a minor fraction of total emitted laser power ends up incident on the sample. Whilst the excitation density is the same as when measuring compressed sensing TRPL, the overall PL intensity is greatly reduced. Therefore, it becomes necessary to bin together some of the DMD mirrors so that the excitation is sufficiently high to produce a detectable amount of PL. In testing, this limited the resolution to about 16×16 pixels.

5.5 System characterisation

The simulation results presented in Chapter 3 indicate that careful management of noise sources is essential when implementing the methodology experimentally. Even small variations in the detected counts can lead to substantial deterioration in the quality of the reconstructed images. To address this, the dark count rate of the detector and its stability over time was examined. The photomultiplier tube (PMT) was set to its operational gain, and the shutter was closed to block incoming light. After a one-hour stabilisation period, the dark count rate was recorded continuously for 24 hours, yielding an average of 46,000 ± 1,000 counts per second (cps), shown in Figure 5-7.

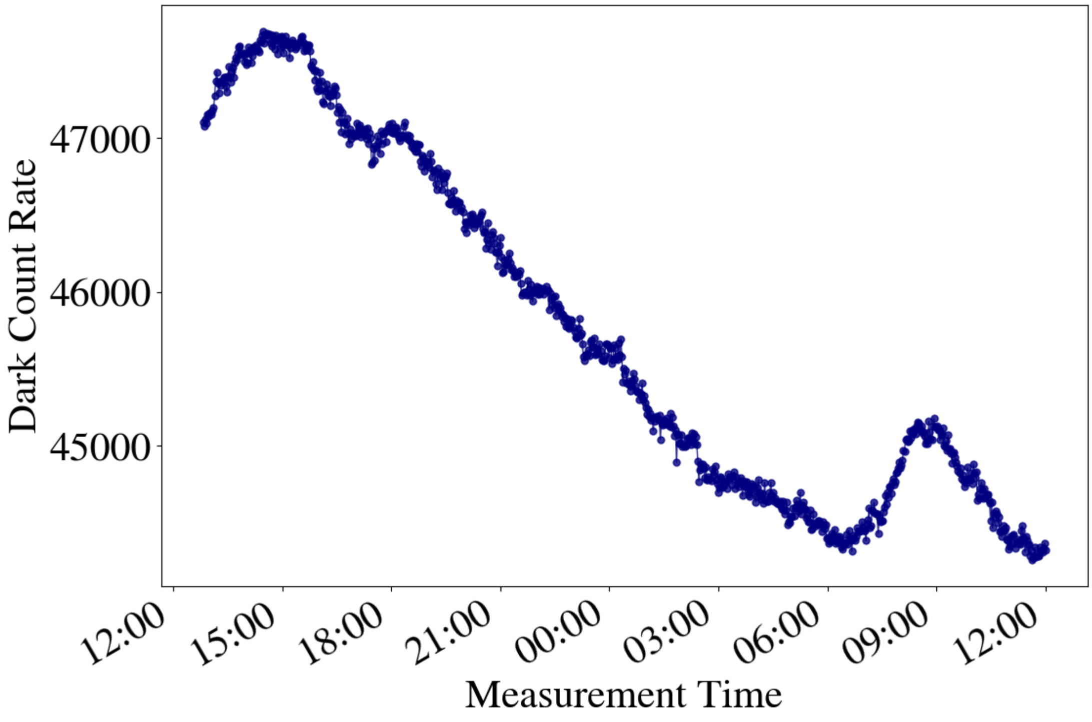

Figure 5-7 The dark count rate of the Hamamatsu HPMT detector with the shutter closed over a period of 24h.

Under normal time-correlated single photon counting (TCSPC) conditions, where the shutter is open and photoluminescence (PL) emission reaches the detector, the count rate typically rises to around 10^7 cps. Thus, the observed fluctuations in dark count rate are expected to have a negligible impact on the overall measurements.

A repetition rate of 20 MHz was used for all the measurements in this chapter, with the laser power set to the maximum available output of 8 mW average power (pulsed) at the laser source (prior to the optical system), unless otherwise stated. To assess sources of noise and uncertainty in the TRPL signal for sample measurements, a CIGS photovoltaic device was used. The TRPL signal was collected 100 times from the same excitation area, with a collection time of 5 seconds for each measurement. The standard deviation of the counts for each time bin of the TRPL signal across the 100 measurements was calculated, as illustrated in Figure 5-8. The standard deviation, expressed as a percentage of the count number, ranged from 2% at the peak of the TRPL signal to almost 10% near the beginning and end of the collection window. As noted in the simulation results, a high standard deviation significantly degrades the quality of the reconstructed image, with simulations showing that noise levels of 2% or higher severely impacted the results. For the experimental data, such high noise levels hindered accurate lifetime calculations, preventing meaningful lifetime estimations, as demonstrated in further sections.

The high noise levels are likely attributable to several factors. To project the desired patterns, the laser beam must first be expanded to fill the DMD area before being focused through the objective lens onto the sample. The final excitation area is approximately 200 × 200 µm, resulting in low excitation power density and a reduced signal-to-noise ratio. Additionally, the multimode laser source used exhibits poor beam quality when expanded, causing non-uniform excitation across the focused region. Furthermore, minor sample response, detector, or laser drift was observed, which also contributed slightly to the increased standard deviation. By examining the total count across each measurement, a slight increase in detected PL intensity was observed throughout the measurement duration. This is most likely due to a gradual change in the CIGS PL efficiency over time due to the pre-conditioning effects of light soaking for such samples [113].

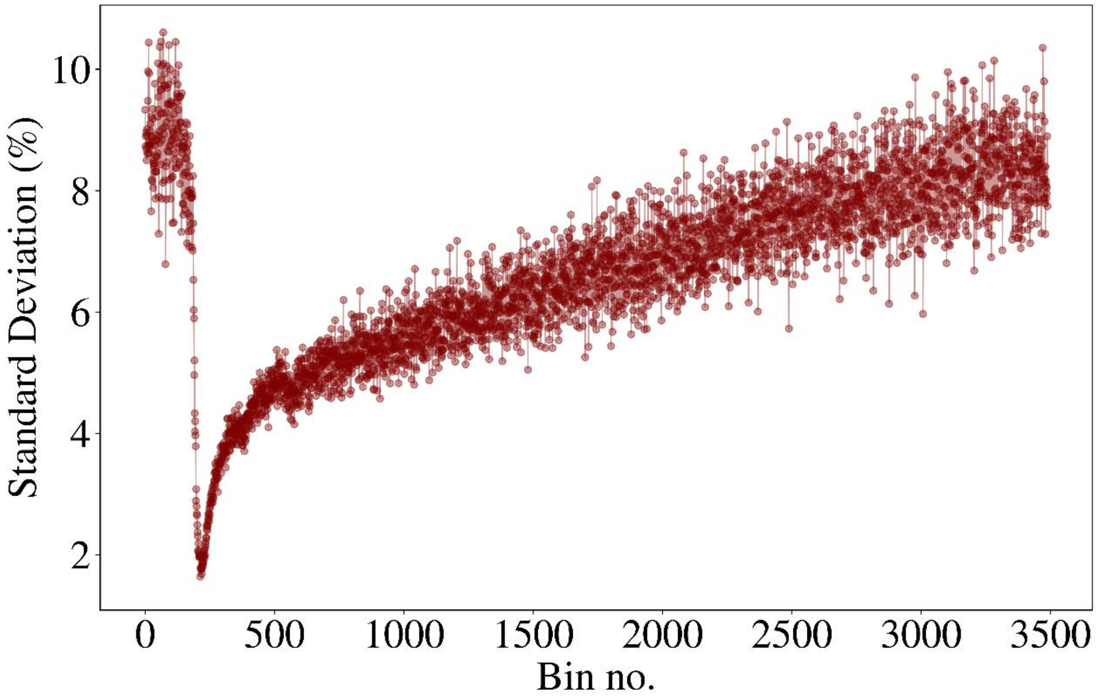

Figure 5-8 The standard deviation as a percentage of the mean number of counts for each time bin of the CIGS TRPL response. TRPL was measured 100 times from the same excitation area, with a collection time of 5 seconds for each measurement. The observed standard deviation curve is inversely proportional to the TRPL signal strength, with the uncertainty being lowest at the TRPL peak.

For the purposes of developing the compressed sensing TRPL method, it was useful to carry out the measurements with 100% sampling level, i.e. projecting the same number of patterns as pixels in the final image. That way during the reconstruction stage, a varied sampling level can be used by taking different amounts of data.

One of the inherent limitations of the compressed sensing method is the implicit assumption that any variation in the measured signal originates solely from changes in the spatial sampling patterns. Whilst using the WHT patterns, there is always 50% of the measurement area being excited. Therefore, in an ideal case, overall intensity throughout the entire measurement duration should remain the same. To check for that, the TRPL spectrum measured at each pattern was integrated, giving a good indication of the overall TRPL intensity for the given pattern. By repeating this for every measured pattern and plotting against pattern number it was possible to determine if any unexpected trends could be observed. The result is shown in Figure 5-9, where a sharp initial fall in TRPL intensity can be seen. No trend was expected for WHT pattern measurement, with small fluctuations and occasional jumps due to variations in the excitation pattern. This trend was suggestive of a drift in CIGS response efficiency, and has been described in work by R. Kenny et al. [114], where the modules are subject to light-induced change of the module efficiency. This drift could be reduced by light-soaking, where the sample is exposed to light prior to starting the measurement acquisition, as the modules are expected to reach a stabilisation point after a period of light soaking.

This temporal drift presents a significant challenge for single-pixel imaging. Since the compressed sensing framework relies on attributing all measured differences to spatial information modulated by the sampling patterns, any drift in the sample's optical response during acquisition introduces artefacts in the reconstruction, reducing both the fidelity and accuracy of the reconstructed image. In contrast, while raster-scanned measurements are also affected by PL efficiency drift, the impact is comparatively less severe. In raster scanning, each spatial point is sampled independently and sequentially. Although temporal drift may affect the absolute signal level across the image, it does not directly violate the assumptions of spatial encoding. To mitigate this, a few different strategies could be explored, such as using a different material, applying pre-conditioning to the sample or attempting to normalise for the sample drift. Pre-conditioning the sample by subjecting it to continuous illumination prior to data acquisition can allow the PL efficiency to stabilise, reducing subsequent drift. Alternatively, an in-situ normalisation approach could be applied – between each structured pattern projection, a reference measurement can be acquired with all DMD mirrors set to 'on' position. This yields a PL intensity reference that can be used to normalise the structured measurements and normalise for temporal drifts, before passing the data through a reconstruction algorithm. Although this approach should effectively correct for sample efficiency changes, it comes at the cost of approximately doubling the acquisition time.

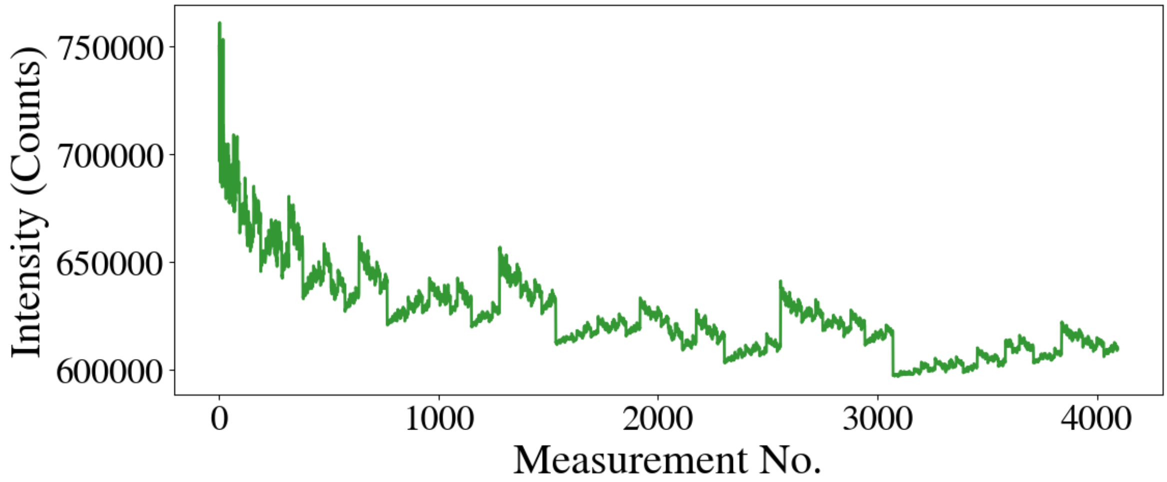

Figure 5-9 Figure showing the total number of counts recorded for each projected pattern. The initial decline in intensity is indicative of sample drift.

5.6 Final results

To create the most reliable reference image, a raster scan of a sample was performed using the DMD. This has the benefit of keeping the excitation exactly the same as for the case of compressed sensing TRPL. However, because there is only a single point of the sample being excited at any given time, the absolute number of mobile carriers in the material get significantly reduced. Therefore, even though the excitation density is the same as for compressed sensing TRPL measurement, the overall signal is reduced. This limits the maximum resolution achievable for the raster scan to about $16\ \text{px} \times 16\ \text{px} \times 12\ \text{ps}$. The dark counts from the detector result in a significant proportion of the signal, making extraction of the carrier lifetimes not feasible. Instead, PL maps were integrated across several time slices to reduce temporal resolution but increase the signal of each map. By reducing the temporal resolution to 3 ns, the noise in the maps could be reduced. The resulting TRPL maps are shown in Figure 5-10. The white pixel approximately at the centre of the images is missing data.

The same area was imaged using the compressed sensing TRPL technique. Measurement spatial resolution was kept the same as for the raster scan example, illuminating the exact same position of the sample, with the same light intensity. The only difference was using the structured illumination patterns rather than single point excitation. After the measurements were acquired, they were processed using a reconstruction algorithm to construct a data cube, giving $16 \times 16 \times 100$ resolution ($X \times Y \times t$) with step sizes of 13 μm × 13 μm × 120 ps. The temporal bins were then grouped, in the same way as in the raster case to get the temporal resolution to 3 ns. The maps shown in Figure 5-11 for periods 0-3 ns, 3-6 ns and 6-9 ns respectively. This reconstruction was performed using 50% sampling level, meaning that the number of patterns measured to reconstruct this data was 50% of the total number of pixels in the image.

Comparing the images in Figure 5-10 and Figure 5-11, they are both dominated by the features of a non-uniform laser beam used for excitation. The high intensity feature near the top of the image is clearly identified in both cases, however it appears to decay more rapidly than in the CS case. However, the images acquired using raster and CS TRPL approaches appear to be in agreement overall, suggesting feasibility of CS-TPRL measurements.

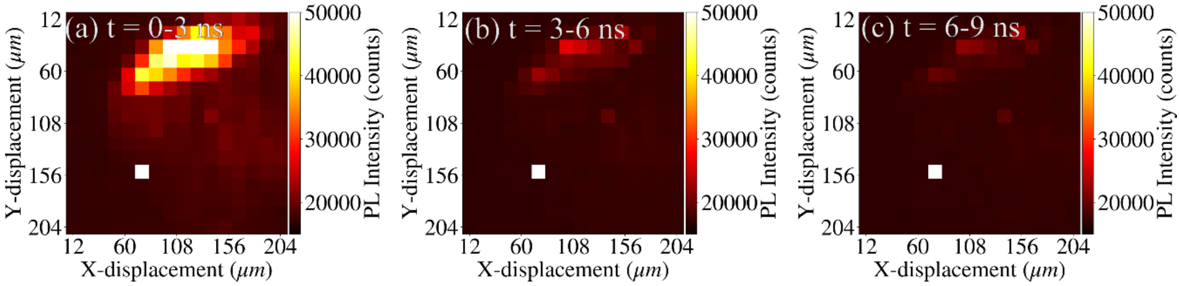

Figure 5-10 Normalised TRPL intensity maps of CIGS sample (a) from the peak emission to 3 ns after the peak, (b) 3-6 ns after the peak and (c). These measurements were acquired by scanning a single point across the sample using the DMD. No measurement data were acquired for the white pixel (failed decay acquisition), hence, it appears white in the maps above

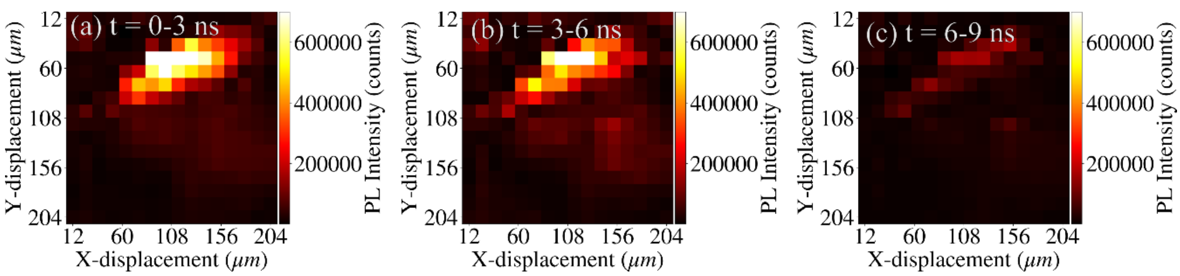

Figure 5-11 Normalised TRPL intensity maps of CIGS sample (a) from the peak emission to 3 ns after the peak, (b) 3-6 ns after the peak and (c) 6-9 ns reconstructed from CS TRPL methodology with 50 % sampling level. The reconstructed maps show good agreement with observations in the point-by-point scan maps

Using the exact same setup, it was possible to increase the spatial resolution for the CS TRPL up to 64 px × 64 px. However, it was not possible to measure at this resolution using a raster scan. Therefore, a direct validation measurement could not be acquired. The same feature at the top of the image was identified, as for the lower resolution images.

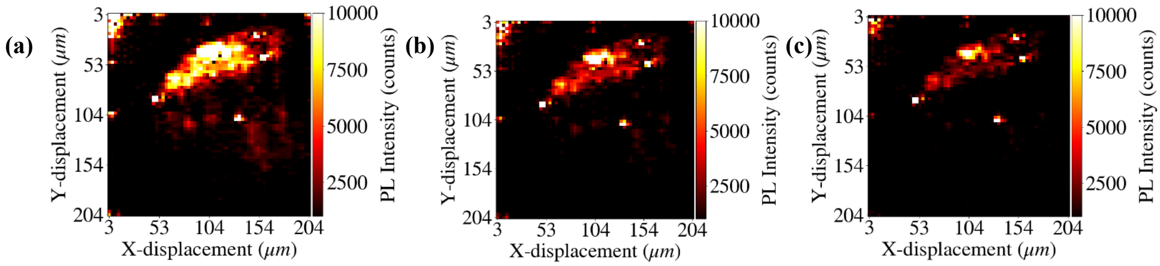

Figure 5-12 TRPL intensity maps of CIGS sample (a) from the peak emission to 3 ns after the peak, (b) 3-6 ns after the peak and (c) 6-9 ns reconstructed from CS TRPL methodology with 50 % sampling level. A resolution of 64 px × 64 px was achieved, with pixel size of 3.2 µm.

An alternative approach was attempted, with increased spatial resolution as shown in Figure 5-13. The spatial resolution was increased to 1.2 µm per pixel—about 10x finer than in the previous images, measuring the same CIGS sample but a different area. As previously, an equivalent raster scan could not be acquired due to low light signal. Image (a) shows a photocurrent map of the same area, captured by contacting the sample using electrical probes and measuring the photocurrent response for each projected pattern. By processing the acquired data through a similar reconstruction algorithm, the response map was obtained. Next, using the data already captured, the TRPL acquired from each pattern was integrated to get an overall PL response for a given pattern, and after reconstruction, the overall PL intensity map is shown in image (b). Furthermore, image (c) shows the PL intensity integrated from the peak of emission to 1.2 ns after, and (d) from 1.2 ns to 2.4 ns after the peak. The PL emission in (c) is more broadly distributed across the sample, while in (d) it appears more localized at a few recombination centres.

Comparing the three images, a dark spot is visible in all three, near the top left where an electrical contact was present. Additionally, some similarities can be seen in the top right with another darker region. Along the left side of the image, where the laser intensity was higher, some brighter regions are seen in all the pictures.

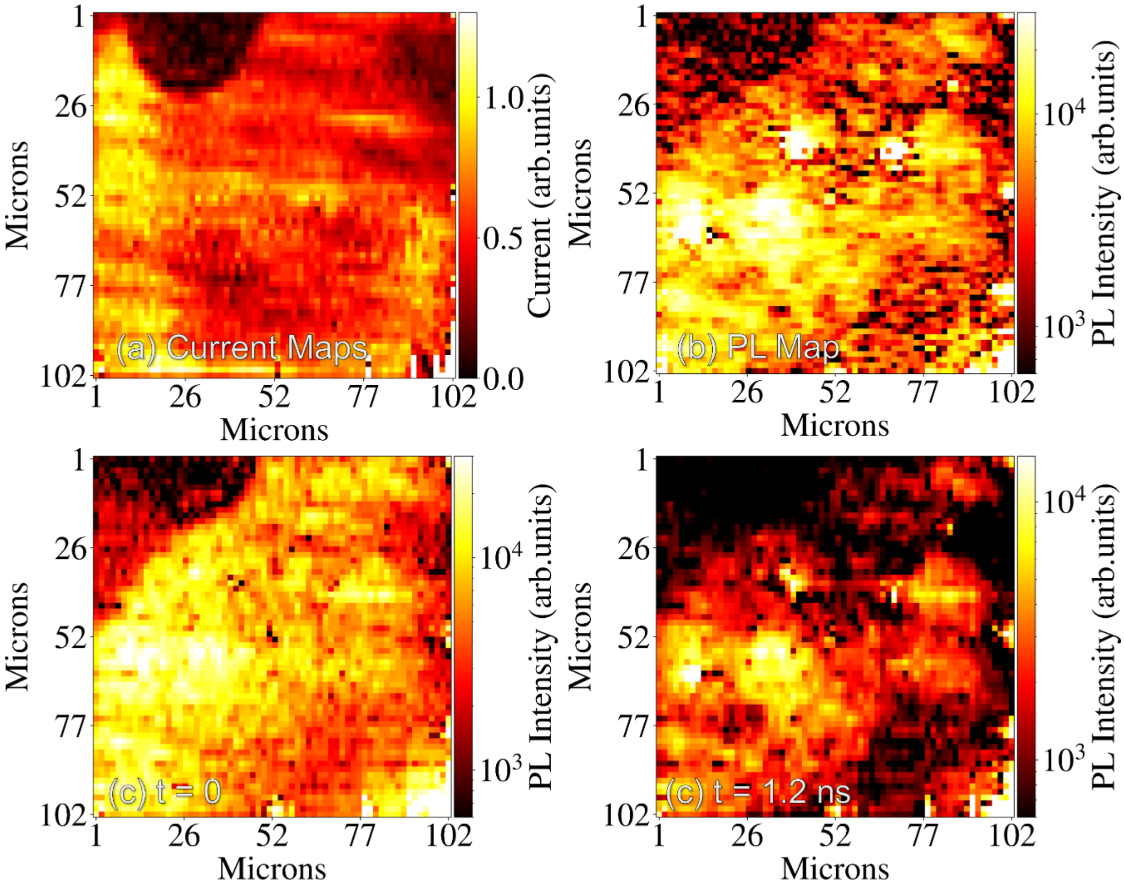

Figure 5-13 Intensity maps of the CIGS sample, with a 64 px × 64 px resolution and a pixel size of 1.6 µm. Image (a) shows the area measured using CS photocurrent mapping. Image (b) was acquired by integrating the time bins of each projected pattern, yielding the overall PL intensity. Images (c) and (d) were acquired using the CS-TRPL methodology and show the PL intensity from the peak of the emission to 1.2 ns and from 1.2 ns to 2.4 ns, respectively. All images were acquired using a sampling level of 50%.

5.7 Chapter conclusions

The work described in this chapter brings together the developments described in previous chapters, modifying the experimental system designed in chapter 4 and utilising the reconstruction techniques from chapter 3. In doing so, this effectively demonstrates the first experimental implementation for compressed sensing TRPL imaging, forming a significant milestone. The results confirm the feasibility of this approach by comparing measurements obtained through compressed sensing with those from traditional raster scanning.

By incorporating a DMD into the experimental setup, the system enabled spatial modulation of the excitation light, enabling the application of the compressed sensing approach to optical measurements. Examples of utilising the setup for measuring the photocurrent response map of a PV device are shown, demonstrating correct operation of the optical aspects of the system. The developed system was also used for measuring the beam profile at the sample plane, after propagating through the optical system, demonstrating the DMD's versatility and its potential for other optical applications.

Results from the computational simulations, shown in chapter 3, detailed how compressed sensing measurements can have high sensitivity to noise. To quantify this, measurements were done tracking the dark count rate of the detector over an extended period of time. For the NIR PMT, this was found to be ~46,000 counts per second, which would account for less than 1% of the overall signal. Additionally, the dark count rate would simply offset every measured value by a fixed amount. Some measurements were also carried out to evaluate how consistent TRPL signal is when sampling the exact same area. It was found that at the peak, the standard deviation was ~2%, rising closer to 10% away from the peak. This could mean that a more stable sample would be more suitable for further investigation and could provide more consistent results.

The results presented from measuring CdTe and CIGS highlight a comparative analysis between images acquired through traditional raster scanning and those obtained via CS TRPL. The reconstruction techniques developed in Chapter 3 were implemented to process the CS measurements, resulting in improved contrast. The acquisition times were improved through reduction in number of measurements necessary as well as faster signal acquisition times, resulting in more than 50% faster measurement acquisition time. The experiments demonstrated that the CS TRPL method is capable of mapping larger areas efficiently while maintaining reasonable spatial resolution.

While some limitations were encountered, particularly in noise sensitivity, laser performance, and sample stability, this work establishes a foundation for future advancements in compressed sensing TRPL imaging. The areas for improvement as well as future development work are discussed in chapter 6.

Chapter 6 Conclusions and Future Work

The primary objective of this project was to integrate time-resolved photoluminescence (TRPL) measurements of semiconductor devices with compressed sensing, in order to develop a novel approach for imaging charge carrier lifetimes. This concluding chapter summarises the key investigations, results and conclusions arising from the research. In addition, it offers a critical evaluation of the advantages and limitations of compressed sensing techniques, both in general imaging contexts and specifically within photoluminescence imaging of semiconductors. A reflective discussion on the methodological outcomes and areas for refinement is presented, followed by recommendations for future research directions.

6.1 Summary of key findings

6.1.1 Modelling of compressed sensing TRPL measurements

In chapter 3, the development of a computational model for exploring compressed sensing in TRPL measurements was presented. This approach had not been previously demonstrated; therefore, the work started with simulations to establish feasibility and optimise the methodology. The computational model was built around statistical simulations, allowing to assess and investigate application of compressed sensing to various measurement approaches and signal dimensionalities.

The computational model development involved 2 main stages – simulating the time-correlated single photon counting (TCSPC) sampling method and simulating compressed sensing acquisitions and reconstructions. The TCSPC simulations were carried out and effects of photon pile-up were investigated, showing some analytical proof of its effects.

The investigation commenced with a 1-dimensional signal as a basic example of compressed sensing, which then progressed to 2-dimensional imaging through a simulation of a single-pixel camera. More complex and practical examples were subsequently explored, simulating compressed sensing for PL imaging, which effectively emulated hyperspectral imaging. Finally, an extra dimension was added by simulating compressed sensing TRPL measurements, using a TCSPC acquisition, arriving at the final simulation of the measurement technique investigated in this thesis.

This model ultimately demonstrated that compressed sensing TRPL measurements are theoretically feasible. Testing the model under various noise conditions revealed that while compressed sensing can reconstruct data efficiently, random noise can significantly degrade reconstruction quality, highlighting the sensitivity of the method to noise and the need for controlled experimental conditions.

It is also worth noting that to quantify the quality of simulated reconstructions, structural similarity index (SSIM) was employed. It provided a perceptually meaningful assessment by accounting for luminance, contrast, and structural similarities between the reconstructed and ground truth images and is particularly valuable in evaluating image quality from human vision perception. However, while SSIM is well suited for general image analysis, particularly in applications such as image compression or enhancement, it may be less directly applicable to the evaluation of reconstructed physical measurement maps, where perceptual similarity is not the primary concern. In such cases, root mean squared error (RMSE) offers a more intuitive and interpretable metric. RMSE quantifies the average magnitude of pixel-wise deviations between the reconstructed and ground truth data, expressed in the same physical units as the original measurement. Therefore, RMSE would likely provide a more relevant and informative measure of reconstruction fidelity, particularly in the context of quantifying the accuracy of the technique.

Overall, this chapter served as a foundational feasibility study, providing a starting point for further development work carried out in this thesis. By establishing that compressed sensing could be effectively applied to TRPL, the groundwork was laid for further development of an experimental system. Additionally, the reconstruction methodology developed for reconstructing compressed sensing TRPL data was used when reconstructing the final data.

6.1.2 Development of TRPL imaging system

In chapter 4, design, development, testing, and improvements of a TRPL measurements system are presented and discussed. The primary focus of this chapter was to establish a fully operational experimental setup capable of measuring TRPL in semiconductor devices. The initial planning stages identified the NIR region as the spectral range desired for this system, with CdTe and CIGS photovoltaic devices as the target materials. Therefore, this guided the selection of key components, such as the laser, detector, and TCSPC electronics. A laser with a 640 nm wavelength was ultimately selected to excite the samples effectively.

After acquiring the components, the process of developing the system included investigating the laser properties. Given the divergence of the laser beam, cylindrical lenses were incorporated into the setup to improve the collimation. Additionally, the optical path was enclosed to prevent stray laser light from reaching the detector, which was necessary to ensure the detector was primarily detecting the PL emission from the samples.

An important part of the chapter was the process of fitting the TRPL decay curves to extract charge carrier lifetimes accurately. It was found that the charge carrier lifetimes resulting from the measurements could be highly influenced by the presence of laser leakage or reflections, leading to fast-decaying signal components and skewed lifetime values. Adjustments such as reconvolution fitting or adjusting the starting point of the fit were attempted, however, these proved to be unreliable.

This chapter also focused on developing the software necessary for running TRPL imaging measurements. LabVIEW scripts were written to automate the TCSPC acquisition and combined with the control of the translation stage. Initial tests on CdTe device validated the system's capability to map carrier lifetimes.

Overall, the work carried out in this chapter, combined with modelling work of chapter 3, allowed for the final implementation of compressed sensing TRPL imaging system described in chapter 5.

6.1.3 Implementing compressed sensing for TRPL imaging

In chapter 5, the developments and insights of Chapters 3 and 4 are integrated to achieve the primary objective of this thesis – creating a TRPL measurement system capable of compressed sensing imaging. This work represents the first implementation of such a technique, demonstrating its feasibility and establishing a foundation for further exploration of compressed sensing in TRPL applications. The successful development of this system not only validates the methodology of compressed sensing TRPL imaging but also opens the door to future advancements and optimisations.

This implementation was achieved by incorporating a digital micromirror device (DMD) into the TRPL measurement system. With careful optical configuration, the DMD pattern could be projected onto the sample via the microscope objective, allowing for selective excitation of varied regions across the device. This setup enabled spatially resolved compressed sensing TRPL measurements, with the DMD dynamically adjusting the illuminated areas based on the desired sampling pattern. The same setup is also adaptable to other measurement modalities, by modifying the property being measured. For example, when characterising a photovoltaic (PV) device, the photocurrent map of the same area could also be acquired. Alternatively, by switching out the PMT for a spectrometer, hyperspectral information about the sample could also be acquired, provided sufficient signal was present.

The acquired TRPL measurements were reconstructed using the methodology developed in Chapter 3. To improve the quality of the reconstructed signal, the temporal resolution was adjusted by merging time bins to form broader intervals, enhancing the amount of signal in each time bin. The reconstruction process resulted in a data cube, providing representation of the TRPL signal at each point within the measured area.

To validate the technique, raster scan measurements were carried out. Since the system was already configured with a DMD in its optical path, these measurements could be done using the DMD itself. This approach ensured that the imaged area remained identical to the one imaged with compressed sensing approach and that the light intensity per unit area incident on the sample was consistent between both techniques. An additional benefit of the DMD is its ability to selectively control the projected beam spot size, allowing for fine-tuning of the excitation area as needed. When comparing raster scan measurements to compressed sensing TRPL measurements, similar features were observed even with a 50% sampling rate for the compressed sensing approach. This reduction in the number of measurements directly translated into shorter acquisition times. Further advantage for compressed sensing measurements was that for a given laser excitation density, the amount of TRPL signal is increased due to the larger excited area.

Some initial limitations were encountered that would benefit from further investigation. After reconstruction, the TRPL signal intensity at each pixel was relatively low, making it challenging to reliably extract charge carrier lifetimes. Validating compressed sensing TRPL measurements was particularly challenging. The most reliable approach was performing raster imaging over the same area. However, the reduced signal strength from exciting a single point compared to a larger area limited the highest achievable spatial resolution. Nevertheless, the DMD offers an advantage in compressed sensing TRPL by allowing for more flexible sampling across a broader range of excitation levels, potentially enhancing signal strength and measurement precision.

Interesting investigation could be investigating whether the use of projected patterns could have some applications in imaging past diffraction limit. Since the spatial information is encoded before the microscope objective, it might be some details could be acquired that were smaller than the laser wavelength.

Overall, whilst demonstrating these measurements proved challenging, the results presented here provide the first validation and implementation of compressed sensing TRPL imaging setup. Although the system readily acquired measurements, often yielding seemingly high signal levels when projecting the patterns, validating the reconstructed images remained a persistent difficulty throughout the project. This challenge was compounded by the properties of the excitation laser and various optical components. Reconstructed images frequently displayed features, but it was consistently difficult to determine whether these represented actual sample characteristics or artefacts from the laser beam. Nevertheless, this work successfully implemented the core methodology proposed in this thesis. Further potential improvements and areas for investigation are outlined in the following section.

6.2 Critical evaluation of compressed sensing for TRPL

Although compressive sensing was employed throughout this work as a means to enable PL imaging with a single-pixel detector, its broader utility in the imaging field remains context-dependent. Compressive sensing and single-pixel imaging are not universal replacements for conventional imaging systems - they offer specific advantages in niche applications where conventional cameras are unsuitable or unavailable. In situations where high-quality detector arrays exist—such as visible-wavelength imaging using CMOS or CCD sensors—conventional imaging offers superior performance in terms of spatial resolution, SNR, and acquisition speed. These systems benefit from direct pixel-wise detection and avoid the ill-posed inversion problems inherent in compressive sensing based reconstruction, where an image has to be reconstructed from a smaller number of measurements. The underdetermined nature of compressive measurement, means that small errors, such as drift or noise, can propagate to have large effects on the final reconstructed image.

However, single-pixel imaging can become attractive in areas where detector arrays are either unavailable or prohibitively expensive. For example, at the time of starting this research, there were no readily available detector arrays capable of recording TRPL transients at each spatial pixel with high temporal resolution. Therefore, traditional TRPL techniques have typically relied on raster-scanned excitation coupled with a fast photodetector such as a PMT or single-photon avalanche diode (SPAD), which, while effective, are inherently slow due to the need for serial acquisition, where each measured pixel is treated as completely independent from one another. The approach presented in this thesis aimed to address this limitation by using a single PMT and structured illumination patterns. This in principal can offer advantages for charge carrier lifetime imaging, such as enhanced repeatability compared to scanning approaches, high image resolution and increased measurement speed. Moreover, compressed sensing TRPL could offer an improvement in the contrast of acquired maps due to exciting a broader area at the same time compared to point-by-point scan, due to measurements being detector noise limited.

In the methodology presented here, the laser excitation is expanded to fill the active area of the DMD, thereby reducing the irradiance on the sample and injecting fewer mobile carriers into the semiconductor. This typically means that the recombination pathways within the material are dominated by non-radiative recombination. In this regime, the TRPL measurements are likely to be limited by detector noise, such as dark counts, which remain relatively constant as the signal intensity increases. Consequently, the application of multiplexing through structured illumination presents an opportunity to enhance the overall SNR. While the irradiance remains unchanged, the illuminated area increases as patterns are projected onto the sample. However, when the sample irradiance is elevated, shot noise may begin to dominate. In this case, measurements acquired for each pattern exhibit minimal variation, with only slight differences between them. The high shot noise present in the bias contaminates all measurements, leading to a significant degradation in the final image SNR, even if the recorded signal appears relatively strong. This shot noise can then propagate through the compressed sensing reconstruction process, further compromising the quality of the final image. This could also explain the results shown in chapter 5, where after the reconstruction, the individual pixel transient decay was severely degraded. Therefore, it remains to be seen, whether increasing the irradiance levels could result in better results.

A key factor influencing the accuracy of charge carrier lifetime extraction is the SNR of the acquired data. In raster-scan TRPL imaging, each spatial point is measured directly, and decay curves are fitted to the time-resolved signal collected at that location. The SNR in this case is governed by the photon statistics and noise characteristics of the detector for each pixel, making it relatively straightforward to manage via integration time or averaging. In contrast, the compressed sensing approach relies on acquiring spatially multiplexed signals, with the TRPL signal at each measurement representing a weighted sum over many spatial locations. Although this approach leads to increased total signal per measurement due to the larger illuminated area, the inversion process required to reconstruct spatially resolved TRPL curves can introduce additional sources of uncertainty. Noise in the measurement domain is redistributed during reconstruction, and artefacts arising from imperfect inversion may affect the accuracy of extracted decay times. As observed in chapter 5, even when the original measurements yield high levels of signal, after the reconstruction, the TRPL curve of each pixel has low signal. This highlights a key difference between the single pixel imaging and raster approaches – compressed sensing improves the measurement acquisition time at the cost of increased reconstruction complexity and reduced clarity at each spatial point.

More recently, some SPAD array sensors have emerged as commercial products, such as Horiba's FLIMera [115] and Canon's MS-500 [116]. The FLIMera is particularly relevant to the work presented in this thesis, as it is a fluorescence lifetime imaging (FLIM) camera equipped with a $192 \times 128\ pixel$ SPAD array, each coupled with a time-to-digital converter (TDC) capable of achieving timing resolutions below $40\ ps$. This configuration enables simultaneous TCSPC measurements across all pixels, facilitating real-time video-rate fluorescence lifetime imaging. Such capabilities are particularly advantageous for dynamic studies of live cells and complex molecular systems.

These emerging technologies signal a shift towards more integrated and efficient imaging systems. The FLIMera, with its real-time TCSPC capabilities, could present a compelling alternative to traditional raster-scanned TRPL methods, potentially reducing the need for compressed sensing-based TRPL imaging. As these technologies continue to evolve, they are expected to increasingly influence the landscape of time-resolved imaging, challenging the relevance of compressed sensing in this field, much in the way that the existence of conventional cameras make the use of compressed sensing for conventional imaging impractical.

6.3 Technique limitations

A known limitation of compressed sensing systems is the potential for imperfect inversion, often arising from calibration errors or inaccuracies in the system model, which can significantly degrade the quality of reconstructed images. In the present system, the main sources of inversion imperfection stem from optical calibration errors—such as misalignment between the DMD projection and the sample plane due to lens aberrations or focus drift—as well as noise amplification during the inversion process. Such deviations introduce errors in the sensing matrix, violating the Restricted Isometry Property (RIP) conditions required for robust compressed sensing recovery, as discussed by Candès et al. [117].

Despite these challenges, several studies demonstrate that high-quality image reconstruction is attainable under compressed sensing, even in the presence of moderate calibration errors.

For example, work done by G. Koutsourakis et al. [42], demonstrated a megapixel resolution reconstruction of a photocurrent response map of a photovoltaic device. Similarly, in this thesis (Section 5.3), high-fidelity photocurrent microscopy images were reconstructed using compressed sensing, illustrating that accurate spatial information can be recovered in electrically measured signals where SNR is relatively high and inversion artefacts are less critical.

In contrast, the application of compressed sensing to TRPL imaging places more stringent demands on both spatial and temporal accuracy, as lifetime extraction is highly sensitive to noise and artefacts in the reconstructed decay curves. The TRPL implementation presented here successfully recovered macroscopic spatial features, but inversion artefacts and low per-pixel SNR significantly degraded the fidelity of decay fitting, to the point where fitting was not possible. For compressed sensing to be viable for quantitative TRPL imaging, improvements in calibration precision, noise robustness, and inversion algorithms would be necessary to achieve decay curve fidelity of sub-nanosecond, which would be required for semiconductor characterisation.

6.4 Future work

This project explored and demonstrated the potential of compressed sensing for TRPL imaging. However, several challenges were encountered, which could benefit from further improvements to the experimental setup as well as further research. Below, the various potential future directions for further research and development are outlined.

6.4.1 Methodology improvements

One of the most significant improvements to the system would be the use of a more suitable laser source for sample excitation. The laser employed in this work exhibited multiple spatial modes, resulting in a highly non-uniform beam profile. Replacing this with a single-mode laser that provides a uniform beam profile would enhance the quality of the measurements and increase confidence in the acquired images. While a laser source with a top-hat beam profile would likely be ideal for these types of measurements, a Gaussian beam with a low

M^2 value would also offer a significant improvement by producing a more predictable illumination pattern. This improvement would help ensure that the observed features in the images are genuine, rather than artefacts introduced by the non-uniform beam profile. This could be improved further, by implementing flat-field correction to calibrate for non-uniformities within the laser beam.

Another important consideration for future development is the laser stability over time both in terms of optical power and its spatial distribution. Fluctuations in laser power can introduce inconsistencies in the compressed sensing reconstruction, similar to the sample drift issues discussed in Section 5.5. To mitigate this, it would be beneficial to implement active monitoring of the laser output by sampling a fraction of the beam. This could be achieved using a simple beam splitter to direct a small portion of the laser light to a photodiode or other power monitoring device. Although this approach marginally reduces the excitation power reaching the sample, the trade-off is likely favourable, as the enhanced confidence in the stability of the excitation source and the ability to normalise for power fluctuations outweigh the slight loss in intensity. Moreover, the additional hardware required is inexpensive and does not introduce significant complexity to the optical system.

In parallel, the normalisation strategy discussed in Section 5.5, where the DMD is set to an all-on pattern between each measurement to record a reference signal, should be explored further While this method increased the acquisition time, at this stage of system development, the increase is justifiable if it results in more robust and interpretable measurements. Both approaches - active excitation monitoring and sample drift normalisation, could be employed to derive a normalisation factor, which may then be applied to each TRPL signal prior to reconstruction, thereby compensating for variations in excitation conditions.

As demonstrated in Chapter 3, the compressed sensing reconstruction is highly sensitive to noise in the measurements. Simulated data revealed that even modest levels of random noise, on the order of 1–2% of the signal amplitude, can result in a much larger degradation in the reconstructed image quality. This highlights a fundamental limitation of single pixel imaging techniques – their susceptibility to both random noise and drifts in the system parameters.

Any gradual variation in the excitation intensity or sample response will be misinterpreted by the reconstruction algorithm as a result of the spatially encoded signal, resulting in artefacts in the final image.

Furthermore, the compressed sensing system exhibits greater sensitivity to power fluctuations compared to conventional raster scanning approaches. In raster-scanned systems, small pixel to pixel variations in laser intensity typically do not affect the extracted lifetimes, as these are derived from temporal decay profiles that do not change significantly with small fluctuations in excitation power. Similarly, spatial inhomogeneities such as speckle or beam profile variations are less problematic in raster scanning, since the beam is focused to a small spot and fluctuations within that spot should have almost no impact. In contrast, compressed sensing relies on structured illumination and spatial encoding – every measurement is a linear combination of many individual points. As such, any deviation in laser power or beam shape between patterns introduces inconsistencies that can distort the reconstruction.

Even if the laser was replaced with a source featuring a highly uniform beam profile, care would still be needed to ensure spatial stability throughout the measurement duration. Uniform beam profiles still typically exhibit speckle patterns, which can also degrade the quality of reconstructions. More critically, any temporal variation in the spatial distribution of the beam would severely compromise the measurement. In principle, the simulation framework developed in Chapter 3 could be extended to model these effects by introducing spatially varying detection probabilities across the virtual sample. While direct monitoring of spatial fluctuations during measurement is challenging, it could be partially addressed by diverting a portion of the beam to a camera or beam profiler via an additional beam splitter. However, such monitoring would need to occur before the laser passes through the microscope objective. Therefore, any aberrations introduced downstream in the optical path would not be detected, limiting the effectiveness of this approach.

Another advantage of introducing a single-mode laser would be the reduction of optical losses and improved beam collimation. In the current setup, the laser beam is highly divergent, and despite the use of cylindrical lenses for beam correction, the beam still overfilled the DMD, resulting in significant optical losses. With a highly collimated beam, not only would the optical losses be reduced but also the spot size could be more precisely controlled, ensuring that the beam is only as large as necessary. This would be particularly beneficial when imaging smaller-scale features, as only a portion of the DMD would need to be illuminated, rather than overfilling the entire device. Additionally, when higher resolution images or a larger field of view are needed, the beam could be expanded accordingly.

The laser power was a limiting factor in these measurements. Due to the divergence of the beam, the overall excitation density reaching the sample was relatively low. By improving the beam collimation and incorporating a higher-power laser, the excitation density could be significantly increased. This would lead to stronger photoluminescence signals and a higher signal-to-noise ratio, thereby enhancing both the clarity and accuracy of the measurements.

Improvements to the laser source would significantly expand the scope of studies that could be performed. With the system described in this work, most measurements were conducted with the laser power set at the maximum available level, limiting the ability to explore varying excitation conditions. A more powerful and better-collimated laser would facilitate measurements across different excitation levels, which is particularly important for investigating the charge carrier dynamics within the semiconductor. This approach would allow for the acquisition of 4-dimensional data, encompassing two spatial dimensions, time, and excitation intensity. By fitting a decay curve to the time-resolved data, a data cube could be generated, revealing how charge carrier lifetimes vary with excitation level. Such a dataset would offer valuable insights into non-linear phenomena, including dominant carrier recombination mechanisms and saturation behaviours, which may not be detectable at a fixed excitation level. This would enhance the method's capability, transforming it into an even more powerful and comprehensive tool for semiconductor characterisation.

6.4.2 New applications

In this work, the materials investigated had bandgaps in the near-infrared region. However, the methodology and techniques presented here are largely wavelength-agnostic, meaning they could be readily adapted for the study of materials in the visible spectrum. Investigating samples in the visible range would require a shorter-wavelength laser and replacement of the current optics with components optimised for visible light. Expanding the methodology to the visible spectrum would enable the characterisation of materials and devices relevant to microdisplay applications, such as microLEDs and various perovskite materials. These materials typically exhibit high emission levels, which would help mitigate the low signal issues encountered in this work, potentially improving both the efficiency and accuracy of the measurements.

An intriguing area for further research could be exploring whether the use of projected patterns could facilitate imaging beyond the diffraction limit. Since spatial information is encoded prior to the microscope objective, it may be possible to capture details smaller than the laser wavelength, potentially revealing features that conventional TRPL systems cannot resolve.

Another potential direction for future research would involve shifting focus towards biological applications, specifically fluorescence lifetime imaging (FLIM). The measurement principles in FLIM are analogous to those of TRPL imaging explored in this project. However, instead of relying on the emission from semiconductor materials, FLIM involves samples injected with fluorescent dyes that exhibit known fluorescence decay times. By applying the compressed sensing techniques and insights gained from this work, FLIM measurements could benefit from enhanced acquisition speeds and improved spatial resolution. This adaptation would open up new possibilities for faster and more precise imaging in biological contexts, potentially transforming the efficiency of FLIM-based studies.

Another possible direction for investigation is in the computer science domain. As highlighted in chapter 2, measurement matrices are critical for compressed sensing. While the random matrices used in this work are generally suitable for a broad range of samples and applications, purpose-designed measurement matrices could offer significant advantages. By designing the matrices, the system could be trained to identify the key points of interest more rapidly and more reliably. This concept could be applied in a production environment for quality control purposed. The model could be trained on measurements of previous samples and used to determine the optimal measurement matrices. These would converge towards identifying the defining features of the sample significantly faster than general random matrices. However, this approach should only be explored once all the measurement limitations have been solved and the methodology produces reliable results.

A final consideration for future exploration could involve extending the compressed sensing application beyond the spatial domain. While this work focused solely on sparsity within the spatial dimension of the images, signals in the time domain also exhibit sparsity. In this project, every measurement required acquiring the full time-resolved decay. However, compressed sensing could, in principle, be applied to reduce the number of required time bins, thereby improving the temporal resolution. By leveraging temporal sparsity, the methodology could achieve faster acquisition times without sacrificing accuracy and improve the ability to resolve the charge carrier dynamics with greater precision.

6.4.3 Final remarks

As a final remark, this thesis investigated and demonstrated the potential of compressed sensing for time-resolved photoluminescence. However, the principles of compressed sensing extend far beyond this specific application and are broadly applicable across various areas of metrology. Compressed sensing utilises the inherent sparsity of signals – a trait common to many types of measurements. As such, its application holds promise not only for semiconductor characterisation but also for a wide range of fields and measurement techniques, shifting the workload from data acquisition to data reconstruction - a process that benefits greatly from advances in modern computational power.

References

1. Damadian R. Tumor Detection by Nuclear Magnetic Resonance. Science. 1971 Mar 19;171(3976):1151–3.

2. Lauterbur PC. Image Formation by Induced Local Interactions: Examples Employing Nuclear Magnetic Resonance. Nature. 1973 Mar;242(5394):190–1.

3. Röntgen WC. ON A NEW KIND OF RAYS. Science. 1896 Feb 14;3(59):227–31.

4. Von ardenne M. On the History of Scanning Electron Microscopy, of the Electron Microprobe, and of Early Contributions to Transmission Electron Microscopy*. In: Hawkes PW, editor. The Beginnings of Electron Microscopy [Internet]. Academic Press; 1985 [cited 2024 Oct 20]. p. 1–21. Available from: https://www.sciencedirect.com/science/article/pii/B9780120145782500072

5. Binnig G, Quate CF, Gerber Ch. Atomic Force Microscope. Phys Rev Lett. 1986 Mar 3;56(9):930–3.

6. Kino GS. Acoustic Waves: Devices, Imaging, and Analog Signal Processing. Prentice-Hall; 1987. 632 p.

7. Holst GC. Common Sense Approach to Thermal Imaging. JCD Pub.; 2000. 400 p.

8. Shockley W, Queisser HJ. Detailed Balance Limit of Efficiency of p-n Junction Solar Cells. J Appl Phys. 1961 Mar 1;32(3):510–9.

9. Shannon CE. A Mathematical Theory of Communication. Bell Syst Tech J. 1948;27(4):623–56.

10. Lustig M, Donoho D, Pauly JM. Sparse MRI: The application of compressed sensing for rapid MR imaging. Magn Reson Med. 2007 Dec;58(6):1182–95.

11. Qu L, An S, Tian-hong Y, Sun Y. Group Sparse Basis Pursuit Denoising Reconstruction Algorithm for Polarimetric Through-the-Wall Radar Imaging. Int J Antennas Propag. 2018;

12. Metropolis N, Ulam S. The Monte Carlo Method. J Am Stat Assoc. 1949 Sep 1;44(247):335–41.

13. Candes EJ, Wakin MB. An introduction to compressive sampling: A sensing/sampling paradigm that goes against the common knowledge in data acquisition. IEEE Signal Process Mag. 2008;25(2):21–30.

14. Donoho DL. Compressed sensing. IEEE Trans Inf Theory. 2006;52(4):1289–306.

15. Baraniuk RG. Compressive sensing. IEEE Signal Process Mag. 2007;24(4).

16. Murtagh F, Fadili JM, Starck JL, editors. Introduction to the World of Sparsity. In: Sparse Image and Signal Processing: Wavelets, Curvelets, Morphological Diversity [Internet]. Cambridge: Cambridge University Press; 2010 [cited 2024 Oct 19]. p. 1–15. Available from: https://www.cambridge.org/core/books/sparse-image-and-signal-processing/introduction-to-the-world-of-sparsity/F1C52D9A3F7FF55E338BDE3C1A5737DC

17. Candès EJ, Romberg JK, Tao T. Stable signal recovery from incomplete and inaccurate measurements. Commun Pure Appl Math. 2006;59(8):1207–23.

18. Candès EJ. The restricted isometry property and its implications for compressed sensing. Comptes Rendus Math. 2008 May;346(9–10):589–92.

19. Baraniuk R, Davenport M, DeVore R, Wakin M. A simple proof of the restricted isometry property for random matrices. Constr Approx. 2008;28(3):253–63.

20. Thompson A. The cascading haar wavelet algorithm for computing the Walsh-Hadamard transform. IEEE Signal Process Lett. 2017;24(7):1020–3.

21. Cartis C, Thompson A. A New and Improved Quantitative Recovery Analysis for Iterative Hard Thresholding Algorithms in Compressed Sensing. IEEE Trans Inf Theory. 2015 Apr;61(4):2019–42.

22. Maleki A, Donoho DL. Optimally Tuned Iterative Reconstruction Algorithms for Compressed Sensing. IEEE J Sel Top Signal Process. 2010 Apr;4(2):330–41.

23. Park SW, Park J, Jung BC. On the Sparse Signal Recovery With Parallel Orthogonal Matching Pursuit. Ieice Trans Fundam Electron Commun Comput Sci. 2013;

24. Bao W, Liu H, Huang D, Hua Q, Hua G. A Bat-Inspired Sparse Recovery Algorithm for Compressed Sensing. Comput Intell Neurosci. 2018;

25. Tropp JA, Gilbert AC. Signal Recovery From Random Measurements Via Orthogonal Matching Pursuit. IEEE Trans Inf Theory. 2007 Dec;53(12):4655–66.

26. Wu H, Wang S. Adaptive Sparsity Matching Pursuit Algorithm for Sparse Reconstruction. Ieee Signal Process Lett. 2012;

27. Li XH, Chen YL, Hu N, Li W, Yuan TJ, Wang Y, et al. Signal Reconstruction Based on a Fusion Compressed Sensing Frame. Adv Mater Res. 2013;

28. Blumensath T, Davies ME. Normalized Iterative Hard Thresholding: Guaranteed Stability and Performance. Ieee J Sel Top Signal Process. 2010;

29. Zhu J, Li X, Arroyo F, Arroyo E. Error analysis of reweighted l1 greedy algorithm for noisy reconstruction. J Comput Appl Math. 2015;

30. Zhang J, Chen L, Boufounos PT, Gu Y. Cross Validation in Compressive Sensing and Its Application of OMP-CV Algorithm. 2016;

31. Mattingley J, Boyd S. Real-Time Convex Optimization in Signal Processing. Ieee Signal Process Mag. 2010;

32. Usman K, Gunawan H, Suksmono AB. http://ijeei.org/docs-13076566035ae946102bb6b.pdf. Int J Electr Eng Inform. 2018;

33. Zhao F, Hao K, Ding Y. Improved Algorithm Based on StOMP for Compressed Sensing Reconstruction. 2016;

34. Zhao H, Chen C, Shi C. Image Reconstruction Algorithm Based on Variable Atomic Number Matching Pursuit. J Algorithms Comput Technol. 2016;

35. Carrillo RE, McEwen JD, Wiaux Y. PURIFY: A New Approach to Radio-Interferometric Imaging. Mon Not R Astron Soc. 2014;

36. Qin T, Wang X, Meng H, Qin Y, Wan G, Witte RS, et al. Performance Improvement for Thermoacoustic Imaging Using Compressive Sensing. 2014;

37. Cevher V. Convex Optimization for Big Data. 2014;

38. Erkoc ME, Karaboğa N. A Comparative Study of Multi-Objective Optimization Algorithms for Sparse Signal Reconstruction. Artif Intell Rev. 2021;

39. van den Berg E, Friedlander MP. SPGL1: A solver for large-scale sparse reconstruction. 2020.

40. van den Berg E, Friedlander MP. Probing the Pareto frontier for basis pursuit solutions. SIAM J Sci Comput. 2008;31(2):890–912.

41. Doll A, Ravasi M, Relyea D. {SPGL1} Python implementation. 2020.

42. Koutsourakis G, Thompson A, Blakesley JC. Toward Megapixel Resolution Compressed Sensing Current Mapping of Photovoltaic Devices Using Digital Light Processing. Sol RRL. 2021;2100467:1–8.

43. Koutsourakis G, Blakesley JC, Castro FA. Signal amplification gains of compressive sampling for photocurrent response mapping of optoelectronic devices. Sens Switz. 2019;19(13).

44. Duarte MF, Davenport MA, Takbar D, Laska JN, Sun T, Kelly KF, et al. Single-pixel imaging via compressive sampling: Building simpler, smaller, and less-expensive digital cameras. IEEE Signal Process Mag. 2008;25(2):83–91.

45. Gurve D, Delisle-Rodriguez D, Bastos-Filho T, Krishnan S. Trends in compressive sensing for EEG signal processing applications. Sens Switz. 2020 Oct;20(13):1–21.

46. Dai W, Sheikh MA, Milenkovic O, Baraniuk RG. Compressive sensing DNA microarrays. Eurasip J Bioinforma Syst Biol. 2009 Dec;2009(1):1–12.

47. Amir A, Zuk O. Bacterial community reconstruction using compressed sensing. J Comput Biol. 2011 Nov;18(11):1723–41.

48. Koutsourakis G. Compressed Sensing Current Mapping Spatial Characterization of Photovoltaic Devices. IEEE J Photovolt. 2017;7(2):486–92.

49. Quan L, Xie K, Xi R, Liu Y. Compressive light beam induced current sensing for fast defect detection in photovoltaic cells. Sol Energy. 2017 Jul;150:345–52.

50. Quan L, Xie K, Liu Y, Zhang H. Camera enhanced compressive light beam induced current sensing for efficient defect detection in photovoltaic cells. Sol Energy. 2019 May;183:212–7.

51. Žídek K, Denk O, Hlubuček J. Lensless Photoluminescence Hyperspectral Camera Employing Random Speckle Patterns. Sci Rep. 2017 Nov 10;7(1):15309.

52. Klein L, Kristoffersen AS, Touš J, Žídek K. Versatile compressive microscope for hyperspectral transmission and fluorescence lifetime imaging. Opt Express. 2022 Apr;30(9):15708.

53. Klein L, Touš J, Žídek K. Spatially encoded hyperspectral compressive microscope for ultrabroadband VIS/NIR hyperspectral imaging. Appl Opt. 2023 May;62(15):4030.

54. van Rossum G, The Python Development Team. The Python Language Reference - Release 3.8.1. 2018;1–160.

55. Dosselmann R, Yang XD. A comprehensive assessment of the structural similarity index. Signal Image Video Process. 2011;5(1):81–91.

56. Shockley W, Read WT. Statistics of the Recombinations of Holes and Electrons. Phys Rev. 1952 Sep;87(5):835–42.

57. Hall RN. Electron-hole recombination in germanium. Phys Rev. 1952 Jul;87(2):387.

58. Tsai V, Potamialis C, Ulicna S, Bliss M, Betts TR, Gottschalg R. Quantifying minority carrier lifetime and collection efficiency of solar cells by combined optical and electrical characterisation techniques. EU PVSEC 35 Proc. 2018;114–21.

59. Schroder DK. Chapter 7 - Carrier Lifetimes. Wiley Intersci. 2006;

60. Carlson TA, Krause MO. Experimental Evidence for Double Electron Emission in an Auger Process. Phys Rev Lett. 1965 Mar;14(11):390–2.

61. Cuevas A, Macdonald D. Measuring and interpreting the lifetime of silicon wafers. Sol Energy. 2004;76(1–3):255–62.

62. Rossi B. Method of Registering Multiple Simultaneous Impulses of Several Geiger's Counters. Nature. 1930 Apr;125(3156):636–636.

63. Bollinger LM, Thomas GE. Measurement of the Time Dependence of Scintillation Intensity by a Delayed-Coincidence Method. Rev Sci Instrum. 1961 Sep 1;32(9):1044–50.

64. Hirvonen LM, Suhling K. Wide-field TCSPC: Methods and applications. Meas Sci Technol. 2017;28(1):12003.

65. Bachrach RZ. A Photon Counting Apparatus for Kinetic and Spectral Measurements. Rev Sci Instrum. 1972 May 1;43(5):734–7.

66. Binkert Th, Tschanz HP, Zinsli PE. The measurement of fluorescence decay curves with the single-photon counting method and the evaluation of rate parameters. J Lumin. 1972 Jul 1;5(3):187–217.

67. Bradley DJ. Methods of Generation. In: Shapiro SL, editor. Ultrashort Light Pulses: Picosecond Techniques and Applications [Internet]. Berlin, Heidelberg: Springer; 1977 [cited 2024 Oct 26]. p. 17–81. Available from: https://doi.org/10.1007/978-3-662-22574-5_2

68. Cova S, Longoni A, Andreoni A. Towards picosecond resolution with single-photon avalanche diodes. Rev Sci Instrum. 1981 Mar 1;52(3):408–12.

69. Ding X, Zang K, Fei Y, Zheng T, Su T, Morea M, et al. Pile-up correction in characterizing single-photon avalanche diodes of high dark count rate. Opt Quantum Electron [Internet]. 2018;50. Available from: https://doi.org/10.1007/s11082-018-1517-x

70. Virtanen P, Gommers R, Oliphant TE, Haberland M, Reddy T, Cournapeau D, et al. {SciPy} 1.0: Fundamental Algorithms for Scientific Computing in Python. Nat Methods. 2020;17:261–72.

71. Levenberg1 K, Arsenal F. A method for the solution of certain non-linear problems in least squares. Q Appl Math. 1944;2(2):164–8.

72. Moré JJ. The Levenberg-Marquardt algorithm: Implementation and theory. In: Watson GA, editor. Numerical Analysis. Berlin, Heidelberg: Springer Berlin Heidelberg; 1978. p. 105–16.

73. Bevington P, Robinson DK. Data Reduction and Error Analysis for the Physical Sciences. McGraw-Hill Education; 2003. 344 p.

74. Arlt J, Tyndall D, Rae BR, Li DDU, Richardson JA, Henderson RK. A study of pile-up in integrated time-correlated single photon counting systems. Rev Sci Instrum. 2013 Oct 1;84(10):103105–10.

75. Rontani D, Choi D, Chang CY, Locquet A, Citrin & DS. Compressive Sensing with Optical Chaos OPEN. Nat Publ Group [Internet]. 2016; Available from: www.nature.com/scientificreports

76. Wang Z, Li Q. Information content weighting for perceptual image quality assessment. IEEE Trans Image Process. 2011 May;20(5):1185–98.

77. Potamialis C, Lisco F, Maniscalco B, Togay M, Bowers J, Walls M. Process development of sublimated Cu-free CdTe solar cells. Photovolt Sci Appl Technol Pvsat-13. 2017;C99(Figshare item version: 1):153–6.

78. Fonthal G, Tirado-Mejía L, Marín-Hurtado JI, Ariza-Calderón H, Mendoza-Alvarez JG. Temperature dependence of the band gap energy of crystalline CdTe. J Phys Chem Solids. 2000 Oct;61(4):579–83.

79. Tsai V, Bittau F, Potamialis C, Bliss M, Betts TR. Combined Electrical and Optical Characterisation of Recombination Mechanisms and Minority Carrier Lifetime in Solar Cells. In 2018.

80. Uličná S. Solution-processing of Cu(In, Ga)(S, Se $)_2$ solar cells from metal chalcogenides – aspects of absorber crystallisation and interface formation. Loughborough University; 2019.

81. Uličná S, Arnou P, Eeles A, Togay M, Wright LD, Abbas A, et al. Control of Mose2 formation in hydrazine-free solution-processed CIS/CIGS thin film solar cells. In: 2017 IEEE 44th Photovoltaic Specialist Conference (PVSC). 2017. p. 186–91.

82. Feurer T, Reinhard P, Avancini E, Bissig B, Löckinger J, Fuchs P, et al. Progress in thin film CIGS photovoltaics – Research and development, manufacturing, and applications. Prog Photovolt Res Appl. 2017;25(7):645–67.

83. Belghachi A, Limam N. Effect of the absorber layer band-gap on CIGS solar cell. Chin J Phys. 2017 Aug;55(4):1127–34.

84. Sturgk MD. Optical Absorption of Gallium Arsenide between 0.6 and 2.75 eV. 1962;127.

85. Worsley C, Raptis D, P Meroni SM, Patidar R, Pockett A, Dunlop T, et al. Green solvent engineering for enhanced performance and reproducibility in printed carbon-based mesoscopic perovskite solar cells and modules †. Cite This Mater Adv. 1125;2022:1125.

86. Zhang H, Ji X, Yao H, Fan Q, Yu B, Li J. Review on efficiency improvement effort of perovskite solar cell. Sol Energy. 2022;233(December 2021):421–34.

87. Bugajski M, Lewandowski W. Concentration-dependent absorption and photoluminescence of n-type InP. J Appl Phys. 1985;57(2):521–30.

88. BDS-MM Series ps Diode Lasers [Internet]. Becker & Hickl GmbH. [cited 2024 Oct 26]. Available from: https://www.becker-hickl.com/products/bds-mm-series/

89. LDH-I Series - Smart Laser Diode Heads for Taiko PDL M1 | PicoQuant [Internet]. [cited 2024 Oct 26]. Available from: https://www.picoquant.com/products/category/picosecond-pulsed-sources/ldh-i-series-smart-laser-diode-heads-for-taiko-pdl-m1

90. LDH-FA Series - Amplified Picosecond Pulsed Laser Diode Heads | PicoQuant [Internet]. [cited 2024 Oct 26]. Available from:

https://www.picoquant.com/products/category/picosecond-pulsed-sources/ldh-fa-series-amplified-picosecond-pulsed-laser-diode-heads

91. Bülter A. Single-Photon Counting Detectors for the Visible Range Between 300 and 1,000 nm BT - Advanced Photon Counting: Applications, Methods, Instrumentation. In: Kapusta P, Wahl M, Erdmann R, editors. Cham: Springer International Publishing; 2015. p. 23–42. Available from: https://doi.org/10.1007/4243_2014_63

92. Zworykin VK, Morton GA, Malter L. Technical papers: The secondary emission multiplier—a new electronic device. Proc Inst Radio Eng. 1936;24(3):351–75.

93. Shih A, Yater J, Hor C, Abrams R. Secondary electron emission studies. Appl Surf Sci. 1997;111:251–8.

94. Cova S, Ghioni M, Lacaita A, Samori C, Zappa F. Avalanche photodiodes and quenching circuits for single-photon detection. Appl Opt. 1996 Oct;35(12):1956–76.

95. Hirvonen LM, Suhling K. Fast Timing Techniques in FLIM Applications. Front Phys. 2020 May;8(May):1–20.

96. Charbon E. Single-photon imaging in complementary metal oxide semiconductor processes. Philos Trans R Soc Math Phys Eng Sci. 2014 Oct;372(2012):20130100.

97. Cova S, Ghioni M, Lotito A, Rech I, Zappa F. Evolution and prospects for single-photon avalanche diodes and quenching circuits. J Mod Opt. 2004 Oct;1267–88.

98. Kurtsiefer C, Zarda P, Mayer S, Weinfurter H. The breakdown flash of silicon avalanche photodiodes-back door for eavesdropper attacks? J Mod Opt. 2001 Nov;48(13):2039–47.

99. Natarajan CM, Tanner MG, Hadfield RH. Superconducting nanowire single-photon detectors: Physics and applications. Supercond Sci Technol. 2012 Jun;25(6):63001.

100. Gol'tsman GN, Okunev O, Chulkova G, Lipatov A, Semenov A, Smirnov K, et al. Picosecond superconducting single-photon optical detector. Appl Phys Lett. 2001 Oct;79(6):705–7.

101. Hadfield RH. Single-photon detectors for optical quantum information applications. Nat Photonics. 2009;3(12):696–705.

102. Korzh B, Zhao QY, Allmaras JP, Frasca S, Autry TM, Bersin EA, et al. Demonstration of sub-3 ps temporal resolution with a superconducting nanowire single-photon detector. Nat Photonics. 2020;14(4):250–5.

103. Goodrich GW, Wiley WC. Continuous Channel Electron Multiplier. Rev Sci Instrum. 1962 Oct;33(7):761–2.

104. Becker W. Architecture of the bh TCSPC Modules. In: The bh TCSPC Handbook. Berlin; 2021. p. 123–37.

105. Zhang Y, Gross H. Systematic design of microscope objectives. Part I: System review and analysis. Adv Opt Technol. 2019 Oct;8(5):313–47.

106. Thorlabs - TL10X-2P 10X Super Apochromatic Microscope Objective, 0.50 NA, 7.77 mm WD [Internet]. [cited 2024 Oct 26]. Available from: https://www.thorlabs.com

107. Hecht E. Chapter 4 - The Propogation of Light. In: Optics. 5th ed. Addison-Wesley; 2002.

108. Tsai V. Combined Optical and Electrical Characterisation of Minority Carrier Lifetime in Solar Cells. University of Loughborough; 2019.

109. Kuciauskas D, Duenow JN, Kanevce A, Li JV, Young MR, Dippo P, et al. Optical-Fiber-Based, Time-Resolved Photoluminescence Spectrometer for Thin-Film Absorber Characterization and Analysis of TRPL Data for CdS/CdTe Interface. In 2012 [cited 2024 Oct 27]. Available from: https://research-hub.nrel.gov/en/publications/optical-fiber-based-time-resolved-photoluminescence-spectrometer--5

110. Tsai V, Bittau F, Potamialis C, Bliss M, Betts TR, Gottschalg R. Combined Electrical and Optical Characterisation of Recombination Mechanisms and Minority Carrier Lifetime in Solar Cells. In: Proceedings of the 14th Photovoltaic Science, Applications and Technology Conference (PVSAT-14). 2018.

111. Hornbeck LJ. The DMD™ Projection Display Chip: A MEMS-Based Technology. MRS Bull. 2001;26(4):325–7.

112. Koutsourakis G. Compressed Sensing Current Mapping Spatial Characterization of Photovoltaic Devices. Loughborough University; 2019.

113. Gostein M, Dunn L. Light soaking effects on photovoltaic modules: Overview and literature review. In: 2011 37th IEEE Photovoltaic Specialists Conference [Internet]. 2011 [cited 2024 Oct 27]. p. 003126–31. Available from: https://ieeexplore.ieee.org/abstract/document/6186605

114. Kenny RP, Chatzipanagi AI, Sample T. Preconditioning of thin-film PV module technologies for calibration. Prog Photovolt Res Appl. 2014;22(2):166–72.

115. FLIMera [Internet]. [cited 2025 May 21]. Available from: https://www.horiba.com/gbr/scientific/products/detail/action/show/Product/flimera-1989/

116. UK C. Canon MS 500 Video Camera [Internet]. Canon UK. [cited 2025 May 21]. Available from: https://www.canon.co.uk/video-cameras/ms-500/

117. Candes EJ, Romberg J, Tao T. Robust uncertainty principles: exact signal reconstruction from highly incomplete frequency information. IEEE Trans Inf Theory. 2006 Feb;52(2):489–509.